NONLINEAR OPTICAL STUDY OF METALLIC SUBWAVELENGTH HOLE ARRAYS

by

Tingjun Xu

A dissertation submitted to the faculty of
The University of Utah
in partial fulfillment of the requirements for the degree of

Doctor of Philosophy

Department of Electrical and Computer Engineering

The University of Utah

August 2012

The University of Utah Graduate School

STATEMENT OF DISSERTATION APPROVAL

The dissertation of **Tingjun Xu**

has been approved by the following supervisory committee members:

Steven M. Blair	, Chair	**3/7/2012** Date Approved
Ajay Nahata	, Member	**03/08/2012** Date Approved
Mark Miller	, Member	**3/12/2012** Date Approved
Michael H. Bartl	, Member	Date Approved
Valy Vardeny	, Member	**3/15/2012** Date Approved

and by **Gianluca Lazzi** , Chair of the Department of **Electrical and Computer Engineering**

and by Charles A. Wight, Dean of The Graduate School.

ABSTRACT

Light transmission through small apertures has attracted a lot of attention. Only with the advance of nanofabrication techniques does the study of light transmission through subwavelength apertures and hole arrays in the visible region becomes possible. Although there are numerous studies on the extraordinary optical transmission through hole arrays and potential applications, not much work had been done for the study of the nonlinear phenomena generated from these subwavelength hole arrays.

In this thesis, advanced nanofabrication techniques, such as electron beam lithography, have been utilized to fabricate nanometer scaled hole arrays on very thin metal films. Hole arrays with different lattice arrangements, lattice constants and shapes have been fabricated for measurement. Ultrafast laser pulses generated from a Ti:Sapphire oscillator and a regenerative amplifier, which is capable of generating extremely high power laser pulses, are used as the light source for the nonlinear optical study.

Nonlinear measurements, including second harmonic generation and third harmonic generation from the fabricated hole arrays, have been performed. Second harmonic generation studies had been focused on how symmetry plays a role in the process of generating second harmonic signal. Results show that upon breaking symmetry by either the illumination or detection angle, or the symmetry of the aperture itself, very strong nonlinear signals from the nanohole arrays can be generated. For third harmonic generation, the symmetry requirement is less restrictive, but follows the same principle: the highest harmonic signals are produced upon the extraordinary transmission of the fundamental light. The effects of the adhesion layer, the lattice arrangements, lattice constant, aperture shape and nonlinear filling material inside the apertures have been studied for both second harmonic generation and third harmonic generation. As preliminary efforts towards generating supercontinuum from these hole arrays, luminescence from Au has been studied.

CONTENTS

LIST OF TABLES

ACKNOWLEDGEMENTS

First of all, my sincerest gratitude goes to my advisor, Professor Steven M. Blair, for guiding me through the long, tough and interesting path of my Ph.D study, for his expert guidance, mentorship, and for his steady encouragement and support at all levels, both academically and financially.

I would also like to express my deep appreciation to Professor Ajay Nahata, Professor Mark Miller, Professor Valy Vardeny and Professor Michael H. Bartl, for serving on my supervisory committee and providing valuable suggestions and recommendations for my academic studies and researches.

I would like to thank Dr. Matt Delong in the Physics department of the University of Utah for providing me all the conveniences for SEM usage and EBL. I also appreciate all the assistance from all the $MicroFab$ members for all my sample fabrications and characterizations. Professor Chunfei Li in the Physics department of Portland State University was very helpful for training me on focused ion beam lithography.

I greatly appreciate Dr. Yongdong Liu and Dr. Di Wu for tutoring me on the microfabrication and electron beam lithography techniques. As friends and mentors, they did not only teach me how to do researches, but also how to be a nice person.

Great thanks to my colleagues in Professor Blair's photonics research group, for their friendship and companionship, for their encouragement when things were not going smoothly,and for pulling me out of frustration much faster. Special thanks to Steven Paradise for his generous and continuous assistance on getting me started with the optical alignments and operation of the $Ti : Sapphire$ oscillator. Dr. Xiaojin Jiao has contributed all the $FDTD$ simulation results and also provided some measurement results, which have made this work more integrated.

Last but not least, I would like to thank my parents, Mr. Rongshou Xu and Mrs. Chenbi Liang. I have great gratitude to my wife Xiamin Chen, for encouraging me

in all the tough and down times; and for my son Evan Xu and my daughter Effie Xu, for all the enjoyment they bring to me. Their tremendous love and constant support kept me moving forward no matter what has been happening. Without their tolerance and devotion, I could have never gone this far.

CHAPTER 1

INTRODUCTION

Nonlinear optics is a very young scientific field compared to linear optics, which possesses a history about as long as that of human beings. We encounter linear optics from the moment we open our eyes every morning: reflection makes it possible for us to see all kinds of things, scattering makes the sky blue, etc. During all these phenomena, one important factor has not been changed: the wavelength. This is also why it is called linear optics. But we do not observe nonlinear phenomena in our daily life, even when we see different colors; we barely see any new wavelength creation, which is the core of nonlinear optics.

Nonlinear optics allows us to change the color of a light beam, to change its shape in space and time, and to create ultrashort laser pulses, even to use light to control light. Why do we not see nonlinear optical effects in our daily life? There are some simple answers:

1. The light intensities of daily life are too weak, and nonlinear optics usually needs high intensity light to be observed.

2. Most of the light sources in our daily life, like the sun and light bulbs, are incoherent.

3. Materials usually have the wrong symmetry for second harmonic generation, which is the nonlinear phenomenon most likely to occur.

4. Phase-matching is often required, which does not usually happen naturally.

In this chapter, we are going to briefly introduce light matter interaction and fundamental nonlinear definitions. Why we would be interested in the study of nonlinear phenomena from subwavelength metallic hole arrays is also discussed in

the "Motivation" section. The outline of this thesis work is also given at the end of this chapter.

1.1 Light Matter Interaction

When light travels through a medium, its electric field introduces a response in the medium, which can be described by the constitutive equations.[1]

$$\begin{aligned} \vec{B} &= \mu_0 \mu \vec{H} \\ \vec{D} &= \epsilon_0 \epsilon \vec{E} \\ \vec{J} &= \sigma \vec{E} \end{aligned} \tag{1.1}$$

Consequently, the medium interacts with the optical fields, governed by Maxwell's equations.

$$\begin{aligned} \bigtriangledown \times \vec{E} &= -\frac{\partial \vec{B}}{\partial t} \\ \bigtriangledown \times \vec{H} &= \frac{\partial \vec{D}}{\partial t} \\ \bigtriangledown \cdot \vec{D} &= 0 \\ \bigtriangledown \cdot \vec{B} &= 0. \end{aligned} \tag{1.2}$$

According to classical electrodynamics, the electric displacement $\vec{D}$ introduced by an external applied electric field $\vec{E}$ is described as,

$$\vec{D} = \epsilon_0 \epsilon \vec{E} = \epsilon_0 \vec{E} + \vec{P} \tag{1.3}$$

Here $\vec{P}$ is the induced dipole moment per unit volume, or polarization. The wave equation is then given by,

$$\bigtriangledown \times \left[\bigtriangledown \times \vec{E} \right] + \frac{1}{c^2} \frac{\partial^2 \vec{E}}{\partial t^2} = -\mu_0 \frac{\partial^2 \vec{P}}{\partial t^2} \tag{1.4}$$

with the approximation $\bigtriangledown \times \left[\bigtriangledown \times \vec{E} \right] \approx - \bigtriangledown^2 \vec{E}$ valid for a homogeneous, isotropic medium.

1.2 Nonlinear Optics

Nonlinear optics deals with phenomena in which the optical parameters of materials are changed with irradiation by light. In general, this requires very high optical

intensities usually coming from high power lasers. This explains why nonlinear optics did not appear before the invention of laser and develops in parallel with the advance of the laser technologies. Since then, nonlinear optics has greatly impacted many fields in science and technology, ranging from our fundamental understanding of light matter interaction to a wide variety of applications such as frequency conversion and optical switching.

A material system is said to be "nonlinear" because it responds to an applied optical field $\tilde{E}$(t) (starting from here, we use tilde to denote a quantity that varies rapidly in time) in a nonlinear manner upon the strength of the optical field. The induced polarization $\tilde{P}$ of a material system is the mathematical description of this nonlinearity, and it plays a key role in the nonlinear optical phenomena because a time-varying polarization can act as a source of new components of the electromagnetic field.[2] In the case of conventional linear optics, the induced polarization depends linearly on the electrical field, described by the following relationship [3]

$$\tilde{P}(t) = \epsilon_0 \chi^{(1)} \tilde{E}(t) \tag{1.5}$$

where the dimensionless constant $\chi^{(1)}$ is the linear susceptibility. When the incident light has high enough intensity, the induced polarization enters the nonlinear regime,

$$\begin{aligned} \tilde{P}^{NL}(t) &= \epsilon_0 \chi^{(1)} \tilde{E}(t) + \epsilon_0 \chi^{(2)} \tilde{E}^2(t) + \epsilon_0 \chi^{(3)} \tilde{E}^3(t) + \cdots \\ &\equiv \tilde{P}^{(1)}(t) + \tilde{P}^{(2)}(t) + \tilde{P}^{(3)}(t) + \cdots \end{aligned} \tag{1.6}$$

$\chi^{(2)}$ and $\chi^{(3)}$ are the second and third order nonlinear optical susceptibilities, with units m/V and m^2/V^2, respectively. The wave equation for nonlinear optics is then described as equation 1.7 with $\tilde{P}^{NL}$ as the driving term.

$$-\bigtriangledown^2 \tilde{E} + \mu_0 \epsilon_0 \chi^{(1)} \frac{\partial \tilde{E}}{\partial t} + \frac{1}{c^2} \frac{\partial^2 \tilde{E}}{\partial t^2} = -\mu_0 \frac{\partial^2 \tilde{P}^{NL}}{\partial t^2} \tag{1.7}$$

When the fields are treated as vectors, $\chi^{(1)}$ will be a second rank tensor with 9 elements, $\chi^{(2)}$ a third rank tensor with 27 elements and $\chi^{(3)}$ a fourth order tensor with 81 elements. The values and properties of the susceptibility tensors depend on the symmetry of the medium, which may reduce the number of independent and nonzero elements of the tensors.[2] For example, for all centrosymmetric crystals and

isotropic media (gases, liquids and amorphous solids), all even order susceptibility tensors ($\chi^{(2)}$, $\chi^{(4)}$, $\cdots$) must be zero.

In general,[4] the magnitude of $\chi^{(n+1)}$ is approximately equal to $\chi^{(n)}/E_{atm}$, where E_{atm} is the atomic electric field, and $E_{atm} \sim e/{a_0}^2 \sim 5 \times 10^{11} V/m$. Thus, the effect of $\chi^{(2)}$ is a factor of $\tilde{E}/E_{atm}$ smaller than $\chi^{(1)}$. This explains why the nonlinear effect could only be discovered only after the invention of the laser, which delivers a high electric filed comparable to the atomic field.

In the frequency domain, the electric field of the incident light, the real quantity of a physical field, is usually expressed as,

$$\begin{aligned} \tilde{E}(t) &= E e^{-i\omega t} + E^* e^{i\omega t} \\ &= E e^{-i\omega t} + cc \end{aligned} \tag{1.8}$$

Here *cc* is the complex conjugate of the preceding term. The nonlinear polarization in the frequency domain will then be,[4]

$$\begin{aligned} P_l(\omega_i) = {} & {\chi^{(1)}}_{lm}(\omega_i) E_m(\omega_i) \\ & + 2{\chi^{(2)}}_{lmn}(\omega_i; \omega_j, \omega_k) E_m(\omega_j) E_n(\omega_k) \delta(\omega_i; \omega_j + \omega_k) \\ & + 6{\chi^{(3)}}_{lmno}(\omega_i; \omega_j, \omega_k, \omega_h) E_m(\omega_j) E_n(\omega_k) E_o(\omega_h) \delta(\omega_i; \omega_j + \omega_k + \omega_h) \\ & + \cdots \end{aligned} \tag{1.9}$$

The delta functions in equation 1.9 determine which nonlinear process is happening.

For example, from the term $P_l^{(2)}(\omega_i) = 2{\chi^{(2)}}_{lmn}(\omega_i; \omega_j, \omega_k) E_m(\omega_j) E_n(\omega_k) \delta(\omega_i; \omega_j + \omega_k)$, we may have one of the following second order nonlinear effects:

- $\chi^{(2)}(\omega_i; \omega_j, \omega_k)$, optical three wave mixing, which includes sum and difference frequency generation,
- $\chi^{(2)}(2\omega; \omega, \omega)$, optical second harmonic generation or frequency doubling,
- $\chi^{(2)}(\omega; 0, \omega)$, linear electrooptics or Pockels effect,
- $\chi^{(2)}(0; \omega, -\omega)$, optical rectification,
- $\chi^{(2)}(\omega_j + \omega_k; \omega_j, \omega_k)$, frequency upconversion,

- $\chi^{(2)}(\omega_j - \omega_k; \omega_j, -\omega_k)$, parametric oscillation.

And from the term $P_l^{(3)}(\omega_i) = 6\chi^{(3)}{}_{lmno}(\omega_i; \omega_j, \omega_k, \omega_h)E_m(\omega_j)E_n(\omega_k)E_o(\omega_h)\delta(\omega_i; \omega_j + \omega_k + \omega_h)$, we have the following third order nonlinear processes:

- $\chi^{(3)}{}_{lmno}(\omega_i; \omega_j, \omega_k, \omega_h)$, optical four wave mixing,
- $\chi^{(3)}{}_{lmno}(3\omega; \omega, \omega, \omega)$, optical third harmonic generation,
- $Re\chi^{(3)}{}_{lmno}(\omega; \omega, \omega, -\omega)$, nonlinear refractive index,
- $Im\chi^{(3)}{}_{lmno}(\omega; \omega, \omega, -\omega)$, two photon absorption,
- $Im\chi^{(3)}{}_{lmno}(\omega_s; \omega_l, -\omega_l, \omega_h)$, stimulated Raman scattering,

It is clear that second harmonic generation and third harmonic generation are just a small part of a big family of nonlinear optics phenomena.

1.3 Applications of Subwavelength Metallic Aperture

Subwavelength metallic apertures are known to possess interesting characteristics. Even though more work needs to be done to fully understand the transmission properties of subwavelength apertures, there are many remarkable applications demonstrated by utilizing these subwavelength apertures. Here are a few examples.

- *Bio-molecule analysis* : Information from a single molecule[5] can give some insights about kinetic processes not normally accessible by ensemble measurements. In order to optically observe the dynamics of a single molecule, it requires picomolar to nanomolar concentrations of a molecule in order to isolate individual molecules,[6] [7] However, many biological processes occur at micromolar concentrations. So, a three order dilution is needed to observe single molecule dynamics while reserving a relatively high concentration of molecules for the reactions to occur. The subwavelength holes or hole arrays act as small reaction chambers containing on average a few molecules, but reducing observation volume from the femotoliter (obtained by a standard confocal microscope) to the attoliter or zeptoliter range (10^{-18} or 10^{-20}).[8]

- *Bio-molecule sensing* : In biomedical and biochemical research and applications for the characterization and quantification of binding events, surface plasmon resonance (SPR) sensors[9] made from arrays a subavelength metalic nanohole arrays are superior to the traditional Kretschmann configuration,[10] which is generally operating in total internal reflection mode. Since this new sensor operates in transmission mode, it allows for a simpler collinear optical arrangement and provides a smaller probing area than the typical Kretschmann configuration.

- *Nanolaser Technology* : The very small aperture laser ($VSAL$)[11] is one effective method to obtain a promising nanometric light source. The $VSAL$ is basically an edge-emitting ridge waveguide laser or laser diode embedded between a high reflectivity back facet coating and a low reflectivity front facet coated with multilayer dielectric and metal layers, which are designed to maximize the power output and feedback sensitivity in reflection for the $VSAL$ during operation. Then, an aperture with the desired shape and size (usually tens or hundreds of nanometers) is created on the metal films as the laser output. It has great potential applications in high-density optical data storage,[11] scanning near-field optical microscopes,[12] nanolithography[13] and so on.

1.4 Surface Plasmon Polaritons

Surface plasmons are electromagnetic surface waves bound to metal-dielectric interfaces, having their maximum in the metal surface with exponentially decaying fields perpendicular to it[14] (on both sides of the interface), as illustrated in Figure 1.1. When surface plasmons are excited, the direct macroscopic phenomenon is strong light absorption by the metal, and sharp drop of the reflected power. The surface plasmon resonance can be thought of as the coherent oscillation of the conduction band electrons induced by interaction with an incoming electromagnetic field.[15]

Surface plasmons can only be excited at such an interface if the dielectric displacement $\vec{D}$ of the electromagnetic mode has a component normal to the surface which can induce a surface charge density σ.

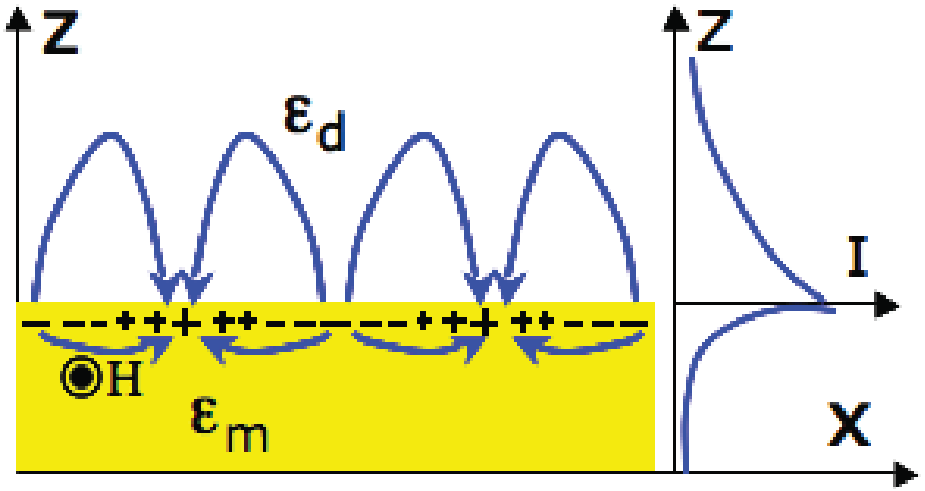

Figure 1.1: Surface plasmons are oscillating modes at the metal:dielectric surface, with maximum at the surface and exponentially decaying fields at both sides.

$$(\vec{D_2} - \vec{D_1}) \cdot \vec{z} = 4\pi\sigma \tag{1.10}$$

S-polarized light propagating along the x-direction (TE) that possesses only an electric field parallel to the y direction, or $\vec{E_i} = (0, E_y, 0)$, is not able to excite surface plasmons. Only P-polarized light (TM) with $\vec{E_i} = (E_x, 0, E_z)$, can couple to such modes.

The fields in metal (1) and air (2) can be described as the following:[14]
for air (medium 2), z>0

$$H_2 = (0, H_{y2}, 0)e^{i(k_{x2}x + k_{z2}z - \omega t)} \tag{1.11}$$

$$E_2 = (E_{x2}, 0, E_{z2})e^{i(k_{x2}x + k_{z2}z - \omega t)} \tag{1.12}$$

for metal (medium 1), z<0

$$H_1 = (0, H_{y1}, 0)e^{i(k_{x1}x - k_{z1}z - \omega t)} \tag{1.13}$$

$$E_1 = (E_{x1}, 0, E_{z1})e^{i(k_{x1}x - k_{z1}z - \omega t)} \tag{1.14}$$

These fields must fulfill Maxwell's equations:

$$\begin{aligned} \nabla \times E_i &= -\frac{1}{c}\frac{\partial H_i}{\partial t} \\ \nabla \times H_i &= \epsilon_i \frac{1}{c}\frac{\partial E_i}{\partial t} \\ \nabla \cdot \epsilon_i E_i &= 0 \\ \nabla \cdot H_i &= 0. \end{aligned} \tag{1.15}$$

And the continuity relations:

$$\begin{aligned} E_{x1} &= E_{x2} \\ H_{y1} &= H_{y2} \\ \epsilon_1 E_{z1} &= \epsilon_2 E_{z2} \end{aligned} \tag{1.16}$$

So

$$k_{x1} = k_{x2} = k_x \tag{1.17}$$

From Maxwell's equation,

$$\frac{\partial H_i}{\partial z} = -\epsilon_i E_{xi}\frac{\omega}{c} \tag{1.18}$$

or

$$\begin{aligned} +k_{z1}H_{y1} &= +\frac{\omega}{c}\epsilon_1 E_{x1} \\ +k_{z2}H_{y2} &= -\frac{\omega}{c}\epsilon_2 E_{x2} \end{aligned} \tag{1.19}$$

This leads to the only nontrivial solution if the determinant D_0 of equation group 1.19 has to be zero:

$$D_0 = \frac{k_{z1}}{\epsilon_1} + \frac{k_{z2}}{\epsilon_2} = 0 \tag{1.20}$$

or

$$\frac{k_{z1}}{k_{z2}} = -\frac{\epsilon_1}{\epsilon_2} \tag{1.21}$$

This equation indicates that surface electromagnetic modes can only be excited at interfaces between two media with dielectric constants of opposite sign. For a dielectric medium, the dielectric constant ϵ_d is positive, so the metal in contact with

the dielectric medium has to be negative. For noble metals, the real part of the complex dielectric functions is negative. This explains why surface plasmon studies were all performed with noble metals. As an example, Figure 1.2 shows the dielectric constant experimentally measured from a thin Au film.

Further, we have:

$$k_x{}^2 + k_{zi}{}^2 = \epsilon_i(\frac{\omega}{c})^2 \tag{1.22}$$

Finally, we have the dispersion relationship of surface plasmon:

$$K_{sp} = \frac{\omega}{c}(\frac{\epsilon_1\epsilon_2}{\epsilon_1 + \epsilon_2})^{1/2} \tag{1.23}$$

Surface plasmons can be excited by electrons by transferring energy from the incident electron to the ones in the solid.[14] They can also be excited by light. In the case of surface plasmons excited by light, the dispersion relationship of the surface plasmons lies on the right of the light line ($k_{SP} < \omega/c$). Because of the difference of the wavevectors for the incident laser from air and the surface plasmon on the surface,

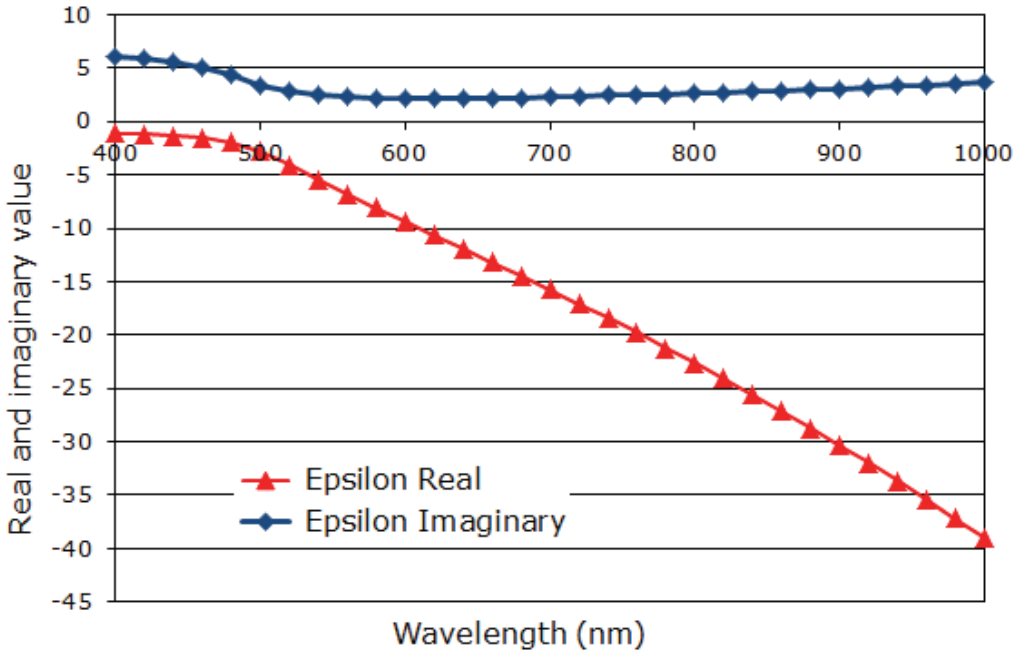

Figure 1.2: Experimentally measured dielectric constant from a thin puttered Au film used in the calculations in later chapters. The negative real part of the Au dielectric constant satisfies equation 1.21, and enables the excitation of the surface electromagnetic waves on the metal-dielectric interfaces.

the incident light can not be directly coupled into surface plasmons. Some coupling methods have to be used to match the momentum to couple the light into the surface plasmon modes. The methods commonly used are end-fire coupling, prism coupling and grating coupling.[16] In the case of metallic subwavelength hole arrays, the hole array serves as a two-dimensional grating to couple the light into surface plasmon modes.

1.5 Extraordinary Transmission from Subwavelength Apertures and Hole Arrays

The pioneering works on light transmission through small apertures were focused on a single aperture because of its enormous applications. With the reduction of the aperture size, one can achieve higher spatial resolution, but it suffers from a power law loss ($\propto (d/\lambda)^4$) of the transmitted power.[17] [18] Even for an array of holes, the throughput scales linearly with the number of apertures, because no interaction between the holes was taken into consideration except the interference from the holes.

A decade ago, Ebbesen[19] found out that by surrounding a single aperture with periodically spaced corrugations, the optical transmission could be strongly enhanced at wavelengths corresponding to the period spacing. Since then, there are many experimental[20] [21] [22] [23] [24] [25] and theoretical studies[26] [27] on the transmission properties of a single subwavelength aperture surrounded by periodic surface corrugations.

Unlike the single aperture transmission, the breakthrough of the extraordinary optical transmission (EOT) from subwavelength hole arrays came with the publication of T. W. Ebbesen's famous *Nature* paper.[28] The extraordinary transmission of this work was believed to be enhanced by exciting the surface plasmon modes. For surface plasmons on a two-dimensional lattice, the momentum conservation is given by,

$$\vec{K_{sp}} = K_x\hat{x} + iG_x\hat{x} + jG_y\hat{y} \tag{1.24}$$

where K_{sp} is the surface plasmon wavevector, $K_x = (2\pi/\lambda_0)sin\theta$ is the component of the wavevector of the incident light that lies in the plane ($\theta = 0$ for normal incidence), G_x and G_y are the reciprocal lattice vectors of the two-dimensional photonic crystal, and i and j are integers. In the case of a square lattice with lattice constant a_0, the

reciprocal lattice vectors are simply $G_x = G_y = 2\pi/a_0$, and the conservation of energy is given by

$$|K_{sp}| = \left[\left(\frac{2\pi}{\lambda_0} sin\theta + i\frac{2\pi}{a_0}\right)^2 + \left(j\frac{2\pi}{a_0}\right)^2\right]^{1/2} \tag{1.25}$$

On the other hand, from SPP theory,

$$|K_{sp}| = \frac{2\pi}{\lambda_0}\left(\frac{\epsilon_d\epsilon_m}{\epsilon_d + \epsilon_m}\right)^{1/2} \tag{1.26}$$

At normal incidence, $\theta = 0$. So

$$\left[\left(\frac{2\pi}{\lambda_0} sin\theta + i\frac{2\pi}{a_0}\right)^2 + \left(j\frac{2\pi}{a_0}\right)^2\right]^{1/2} = \frac{2\pi}{\lambda_0}\left(\frac{\epsilon_d\epsilon_m}{\epsilon_d + \epsilon_m}\right)^{1/2} \tag{1.27}$$

Solve for λ_{max},

$$\lambda_{max} = \frac{a_0}{(i^2 + j^2)^{1/2}}\left(\frac{\epsilon_d\epsilon_m}{\epsilon_d + \epsilon_m}\right)^{1/2} \tag{1.28}$$

and this equation predicts the location of the extraordinary transmissions.

Taking the Ebbessen's *Nature* paper as an example, we can see how well the theory is matching with the experimental results.

According to the surface plasma theory, the surface wave can be excited on both side of the noble metal film upon laser excitation. On the air-metal surface, the refractive index of air is constant, 1. The refractive index of noble metal (Ag in this paper) is wavelength dependent, and can be easily obtained from an online resource: http://refractiveindex.info/. According to the surface plasma theory, the extraordinary transmission wavelength can be calculated and is listed in Table 1.1.

On the metal-glass surface, the refractive index of glass is constant, 1.47, and the extraordinary transmission wavelength can be calculated and listed in Table 1.2.

Figure 1.3 shows the peak positions of the surface plasma modes from the two different interfaces. It is clear that the experimental results match the calculations very well.

Table 1.1: Calculated extraordinary transmission wavelength for surface wave excited on the metal-air interface.

Mode Numbers (i,j)	(1,0)	(1,1)	(2,0)	(2,1)
Calculated peak λ nm	885.6	652.6	476.9	442.8

Table 1.2: Calculated extraordinary transmission wavelength for surface wave excited on the metal-glass interface.

Mode Numbers (i,j)	(1,0)	(1,1)	(2,0)	(2,2)
Calculated peak λ nm	1378.0	953.7	729.3	516.6

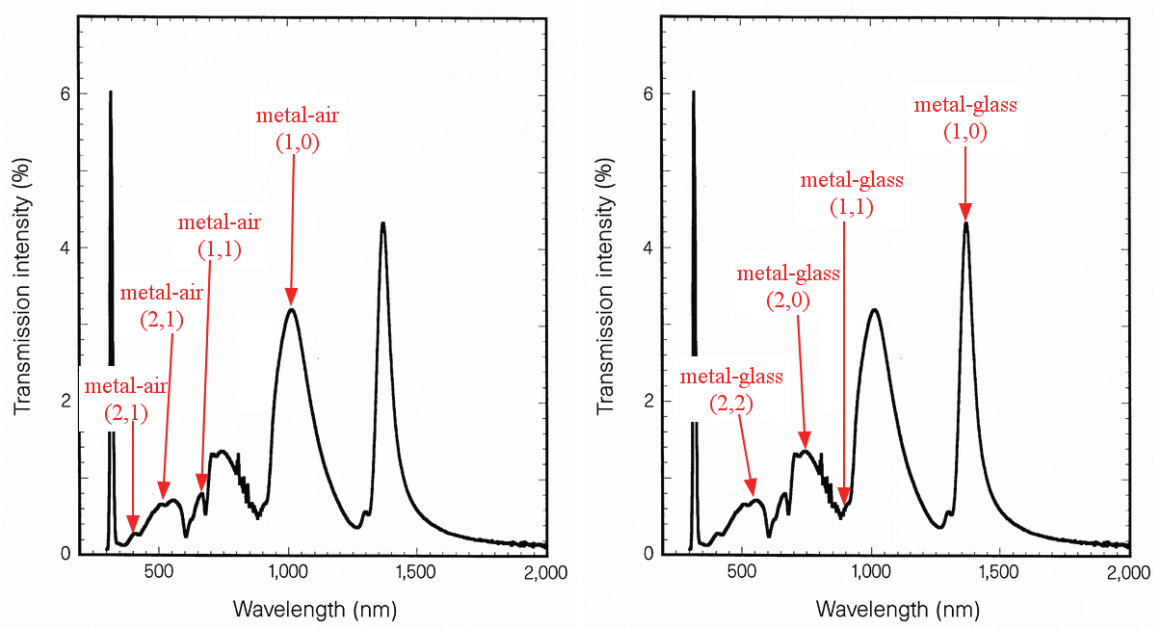

Figure 1.3: The calculated extraordinary transmission peak wavelengths on the metal-air interface (left) and the metal-glass interface (right) are marked out and pointed to the position they should appear on the wavelength spectrum.

After Ebbessen's work, there has been increasing interest in the study of extraordinary transmission from metallic hole arrays. As an example of this, in 1999,[29] Ebbesen patented this observation and today, there are another 73 citing patents.[30] Later, Thio et al.[31] studied normal transmission from square latticed Cr hole arrays. A. Nahata[32] and J. Bravo-Abad[33] found that the periodicity is not a necessity to get the extraordinary transmission either in the terahertz or optical regime with a quasiperiodic hole array. Quite a lot work on the effect of aperture shape has also been done,[3435] and it is normally considered that square holes are considerably better than round holes owing to the localized surface plasmons associated with the hole shapes, and rectangular shapes are better than circles or squares for the same reason. A "C" shaped aperture[36] is probably another good choice for the extraordinary transmission. Different materials have also been studied, even though gold and silver are normally

considered as *good* metals, extraordinary transmission is also observed from Cr[31] and Cu.[39] The thickness of the film[40] [41] also plays an important role in the extraordinary transmission. As film gets thicker, the surface plasmons on the two surfaces become uncoupled and the transmission decreases exponentially.

In all of these cases, it is believed that the incident radiation at a specific wavelengths is coupled to surface plasmon polariton modes via the grating properties of the periodically structured metal surfaces. The surface propagating waves at the resonant wavelengths form standing wave patterns with local maxima at the location of the apertures. This then leads to enhanced transmission at the resonant wavelengths.

More generally,[42] extraordinary transmission can occur in the following ways: when the incident light can be coupled to a surface plasmon mode supported by the incident surface, the enhanced field associated with the surface plasmon mode increases the probability of transmission through the holes, where it is again scattered by the periodic array to produce light. When the incident light cannot be coupled to a surface plasmon mode on the incident side, instead, the matching conditions allow weakly transmitted light through the array to couple to a surface plasmon mode on the output side. Then, the enhanced electric field associated with the surface plasmon mode increases the probability of transmission, and subsequent scattering again results in transmitted light. Sometimes, the coupling conditions might be satisfied on both sides simultaneously, then, the transmission will be greatly enhanced.

1.6 Wood's Anomaly from Subwavelength Apertures and Hole Arrays

The minima on the transmission spectrum were widely believed to be associated with Wood's anomaly, which occurs when the diffracted light becomes tangential to the sample surface. According to surface plasma theory and following similar mathematics, the wavelength minima positions for the two interfaces are given by the equation 1.29 and the calculated results are shown in Table 1.3 and Table 1.4.

$$\lambda_{min} = \frac{a_0}{\left(i^2 + j^2\right)^{1/2}} {\epsilon_d}^{1/2} \tag{1.29}$$

Table 1.3: Calculated Wood's anomaly wavelength on the metal-air interface.

Mode Numbers (i,j)	(1,0)	(1,1)	(2,0)	(2,1)
Calculated peak λ nm	900.0	636.4	450.0	402.5

Table 1.4: Calculated Wood's anomaly wavelength on the metal-glass interface.

Mode Numbers (i,j)	(1,0)	(1,1)	(2,0)	(2,1)
Calculated peak λ nm	1322.7	935.3	661.4	591.5

Figure 1.4 shows the Woods anomaly from Ebbessen's same *Nature* paper, and the anomaly locations are marked with their corresponding modes.

1.7 Motivations

Since surface plasmons describe the fluctuations of the surface electron densities, they are very sensitive to the surface condition on the nanometer scale. Therefore, it is no wonder they have been widely used to study the surface nonlinearities,[44] [45] [46] [47] and surface enhanced Raman scattering, for optical tagging,[48] glucose detection,[49]

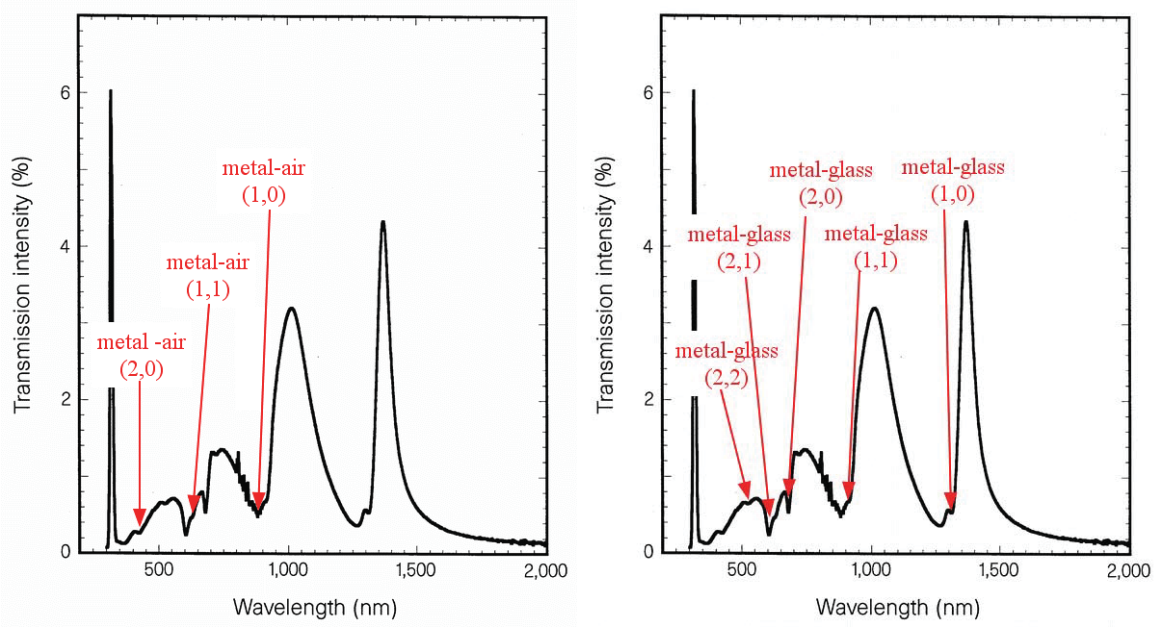

Figure 1.4: The calculated Wood's anomaly wavelengths on the metal-air interface (left) and the metal-glass interface (right) are marked out and pointed to the position they should appear on the wavelength spectrum.

DNA and RNA detection.[50] For nanometer scaled surfaces, like nanoparticles and nanoapertures, the surface plays a more important role than bulk.

There are intensive works on nonlinear optical study on surface and interfaces, and many applications utilizing the nonlinear second harmonic generation from surfaces. With the advance of nanolithographic technology, there are also many studies on second harmonic generation from nanoparticles.

Even though there are intensive studies on the metallic subwavelength hole arrays, most of them are focused on the linear regime. But for nonlinear study, especially for second harmonic generation, third harmonic generation and supercontinuum generation, there are only limited cases.

As a natural expansion of their work on the linear extraordinary transmission, A. Nahata[23] performed the very first work of second harmonic generation in the visible region from a single hole surrounded with periodically structured surface corrugations. The fundamental radiation near the vicinity of the aperture has been enhanced by a factor of more than 100 times, and the second harmonic generation increased by a factor of about 10^4 compared to a similar bare aperture without the corrugations. A similar work[51] reported a little bit earlier with a simple metal aperture also exhibited enhanced second harmonic generation.

M. Airola[52] studied second harmonic generation from metallic subwavelength hole arrays for the first time. They had used a square lattice and disordered round hole arrays. All the samples showed strong second harmonic signal with strong angular dependence. Because of the coherent nature of the interaction among the periodic apertures, the square lattice arrays showed well-defined peaks for both the fundamental and second harmonic signals, with peak positions following to each other, at positions where the surface plasmon resonance occurred.

J. A. H. van Nieuwstadt[53] investigated the influence of the aperture shapes on second harmonic generation with rectangular hole arrays with different aspect ratios. At certain aspect ratios, they observed about two orders of magnitude higher second harmonic signal than other shapes and they attributed this modification to slow propagation of the fundamental wavelength through the holes close to the hole cutoff wavelength.

A. Lesuffleur[54] [55] fabricated an array of double holes with two adjacent holes overlapping to each other, so there are two apexes in the middle of the double holes. They found out that the double holes generated much higher second harmonic signal. Also, the nonlinear enhancement peaks when the double holes have an aspect ratio at $2:1$, which is essentially the same results as J. A. H. van Nieuwstadt.

Most recently, N. Feth[56] reported second harmonic generation from complementary split ring resonator arrays (SRRs in which the metal in the sample plane is replaced by air). Upon the fundamental plasmonic resonance, both the electric and magnetic fields are strongly localized inside the gap of the resonators, which in turn greatly enhances the conversion efficiency of second harmonic generation.[57] [58]

To our knowledge, we have not found any publication on third harmonic generation or supercontinuum generation from metallic subwavelength hole arrays except the second harmonic generation studies mentioned above.

Based on all the works on nonlinear optical studies on metallic subwavelength hole arrays, none of them have systematically studied how the symmetry affects the generation of second or third harmonic generation and even supercontinuum generation, and some other factors related to the hole arrays would affect the nonlinear performance. This sets the goal for this work.

1.8 Thesis Overview

In Chapter 2, I have briefly introduced the most widely used nanofabrication techniques. Most of the contents of this chapter focus on electron beam lithography (EBL). With the restricted facility availability at the University of Utah at the time, we have managed to obtain resolution to the problems associated with the nanolithography, mainly nanohole array fabrication. Decent samples have been fabricated with this method which provided the samples for the nonlinear optical study for this work. In the end, I have also discussed one of the other nanofabrication methods we have used –FIB, along with some sample images fabricated with this method.

In Chapter 3, the other necessity for nonlinear optical generation – the ultrafast high power laser, and some techniques for generating and characterizing the ultrashort pulses are briefly discussed. The experimental setups and measurement techniques,

especially the procedures for sample alignments, used to perform the nonlinear optical measurements have been discussed in a detailed manner because of the specific measurements used in this work.

In Chapter 4, the results of second harmonic generation from subwavelength hole arrays are presented. We have used different methods to break the symmetry to create nonzero second order susceptibility, and generated the second order harmonic signal on all the samples we have studied. In this chapter, we have only studied second harmonic generation from an average lattice constant of about 800nm, which is the central wavelength of our light source. For most of the work in this part, only round shaped hole arrays were used, but nonsymmetric hole arrays are also used to study the effect of aperture shape on the second harmonic generation.

In Chapter 5, we have studied third harmonic generation from the same kind of nanohole arrays. Even though the measurement techniques we have used are the same, quite different results have been obtained for third harmonic generation from the hole arrays even though it is a nonlinear process with much lower conversion efficiency.

In Chapter 6, we have studied some of factors that affect both second harmonic generation and third harmonic generation in different ways. We have varied the period of the lattice to change the resonant frequency of the surface plasma polaritons, used different adhesion layers to study the effect of the adhesion layers to the nonlinear processes, filled the hole arrays with different nonlinear materials trying to enhance the nonlinear conversion and we also used hole arrays with different sizes and shapes to study the roles the aperture played on the second and third harmonic generations.

In Chapter 7, we reviewed our early efforts of generating a supercontinuum from the metallic subwavelength hole arrays, and presented some of our results towards supercontinuum generation. We believe all the results obtained so far are luminescence from metal, and there is still more work to do to achieve the supercontinuum generation.

Finally, in Chapter 8, we proposed some directions in which future research could go and some possible outcomes this research might lead to.

CHAPTER 2

SAMPLE FABRICATION

Since we are working in the visible optical region ($380nm$ to $750nm$), the spacing between the nanoholes should be designed in that range accordingly. Ideally, smaller spacing ($\sim \lambda$) will allow lower order coupling to occur. However, because of the capability we have on campus, it is very difficult to make our holes smaller than $200nm$, so the spacings were designed to be about $800nm$. For most of our samples, we have used the electron beam lithography (EBL) and dry etching methods for fabrication. However, it turns out that focused ion beam (FIB) lithography might be a better method for nanohole array fabrications.

In this chapter, I am going to briefly introduce the most widely used nanofabrication technologies and describe how we have fabricated metallic hole arrays in more detail.

2.1 Nanofabrication Techniques

According to the different light source used, nanofabrication can be categorized as photolithography, electron beam lithography, or laser interference lithography, etc. All the processing steps are pretty much the same except for the light sources and hence the resists. In general, a nanofabrication iteration includes the following steps:

1. Wafer preparation

   In this first step, the wafers to be patterned are thoroughly cleaned to remove any contamination, baked to remove moisture and sometimes an adhesive promoter is applied to promote adhesion of the photoresist to the wafers. In some cases, a thin antireflection layer is applied to reduce reflections within the resist.

2. Photoresist application

   Photoresist is dispensed on the wafer and spin coated. The spinner is usually

running at several thousand RPM to ensure that the wafer is uniformly covered. The coated wafer is then baked (soft bake) to drive off excess solvents and glassfy the resist.

3. Photoresist exposure

   The wafer is then exposed to different light sources, either through a mask or not, depending on the method used, which distinguishes the different types of nanofabrication.

4. Photoresist development

   The exposed wafer is immersed into a developer to either remove the exposed area (for positive tone photoresist), leaving a "positive" image, or the unexposed area (for negative tone photoresist), leaving a "negative" image.[59] The desired pattern is thus generated on the resist.

5. Etching or metalization

   Depending on different applications, metalization or etching is carried out after developing the resist. During metalization, a thin metal film is thermally evaporated or sputtered on the surface of the chip, and the metal film will fill out all the open areas. For the etching, the remaining resist will serve as the protection and the open areas will be etched away.

6. Photoresist removal

   This is generally the final step. The wafer is immersed into a photoresist stripping solution to dissolve away the remaining photoresist. In the metalization case, only the metals inside the holes will survive and all the films on top of the resist will be stripped away, which is called lift-off. In the etching case, the pattern on the resist will be transfered to the layer underneath it.

Another nanolithographic technique, focused ion beam lithography, is fundamentally different from all the above listed methods, and more details about it are given later.

2.1.1 Photolithography

Photolithography[60] (also called optical lithography) is currently the most widely used technology for industrial integrated circuit manufacturing. It is similar to photography in the way that the patterns generated are created by exposure to light, but is more complicated by means of mask making, and other postexposure procedures.

The minimum feature size that can be achieved by photolithography is limited by the wavelength of the light source used, also known as the diffraction limit. By using some new technologies like optical projection lithography and immersion lithography, sub-30 nm feature size[61] [62] has been achieved with photolithography. Figure 2.1 schematically shows the types of photolithography techniques most commonly used.

UV light is generally used as the light source to expose the resist on an aligner. According to the different light used, photolithography is characterized as "g-line" ($436nm$) or "i-line" ($365nm$). Recently, lithography has moved to the "deep ultraviolet" region, with a $248nm$ line produced by a Krypton Fluoride laser, and $193nm$ by an Argon Fluoride laser. A photomask has to be used to block the undesired light and only part of the light gets through. In order to minimize the diffraction effect from the photomask, the patterned side of the photomask has to be placed close to

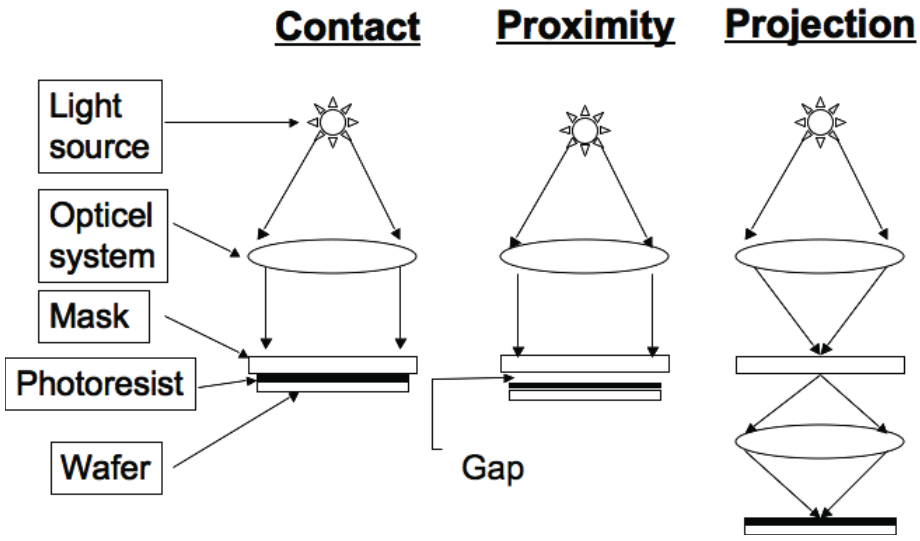

Figure 2.1: A schematic block diagram shows the idea of photolithography and the three primary exposure methods: contact, proximity, and projection.

the wafer. The passed UV light will cut the bonds of the positive resist molecules and make the exposed areas more dissolvable, but it will cross-link the exposed areas for negative resist, which makes the exposed area less soluable in developer.

2.1.2 Electron Beam Lithography

The light source for electron beam lithography is a focused beam of electrons. When the electrons are accelerated by an applied electrical field, usually with a high voltage at $10 \sim 50$ kilovolts, it can be treated as a matter wave with very short wavelength.

$$\lambda_e = \frac{1.226}{\sqrt{V}}(nm) \tag{2.1}$$

For $10 \sim 50$ kilovolts accelerating voltage, the wavelength of the electron beam is in the range of $0.2 \sim 0.5$ angstroms, which is very short for lithography.

Figure 2.2 shows a block diagram of a typical electron beam lithography system. The column is responsible for forming the electron beam with various electron lenses.

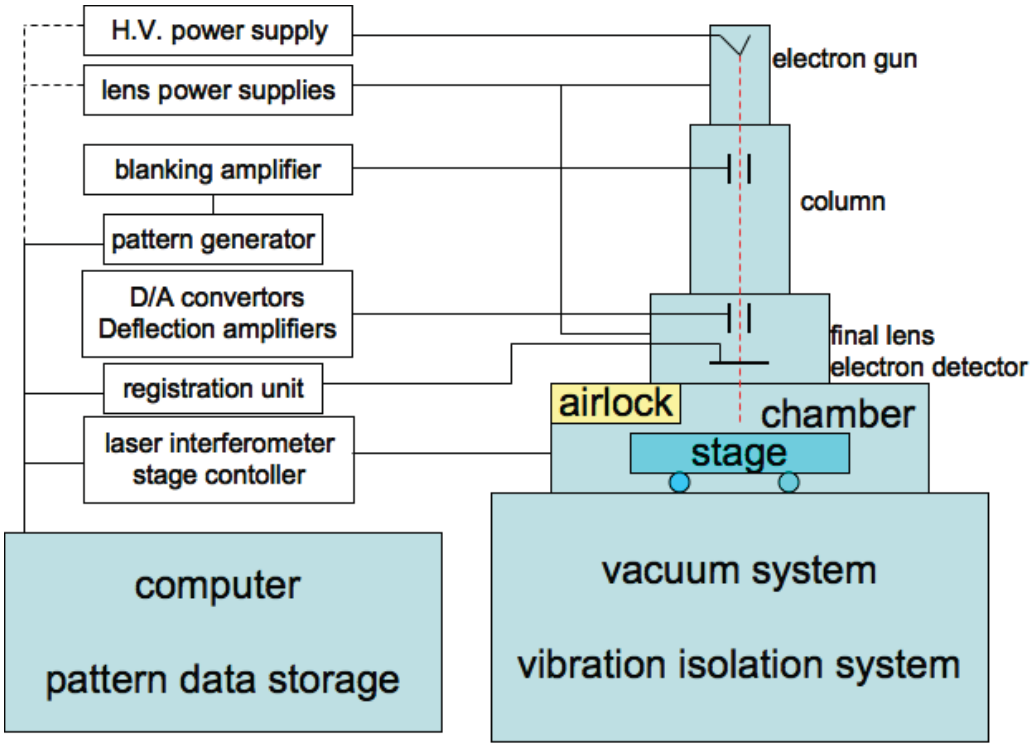

Figure 2.2: A schematic block diagram shows how the electron beam lithography has been carried out. It looks similar to the scanning electron microscope but only has the imaging capability of SEM.[63]

The computer sends out the designed pattern to the pattern generator, which converts the digital signal to an analog signal to control the deflection shutter, and determines when and where to let the electron beam pass through, or to expose the resist.

Commercial electron beam lithography systems are of high performance but very expensive. For example, a middle grade system from Leica or JEOL normally costs between $\$3 \sim 5$ million and a top grade system such as JBX-9300FS or VB6-UHR can cost from $\$6 \sim 9$ millon. A cheaper solution for EBL is to modify an existing scanning electron microscope, like JC Nabity Lithography Systems, which is the one used in the University of Utah. For an EBL system integrated on a SEM which also provides the electron source, the electron beam can be scanned over a surface with a very small diameter beam. Therefore, there is no mask needed for nanolithography. An EBL system simply "draws" [65] the pattern over the resist using the electron beam as its drawing pen. Thus, EBL systems produce the resist pattern in a "serial" manner, making it slow compared to optical systems.

The resolution of electron beam lithography is not limited by the light source because of the extremely short wavelength, but by other factors, such as electron scattering in the resist and by various aberrations in its electron optics. And the electron beam works exactly the same way to either break or cross-link the positive and negative resists.

2.1.3 Laser Interference Lithography

As stated in its name, laser interference lithography uses a laser as its light source. A shorter wavelength is preferred to make smaller structures, but practically, a UV laser radiating at $364nm$ is widely used for consideration of alignment.

One of the most common laser interference lithography configurations is called Lloyd's Mirror[66] setup shown in Figure 2.3. The Lloyd's Mirror setup uses constructive and destructive interference to create a sinusoidal intensity profile of exposure on the resist. This works due to the fact that half of the beam reflects off the mirror and onto the sample. That reflection changes the angle of the beam. As a result, when the reflected and incident beams meet on the face of the sample, the constructive and

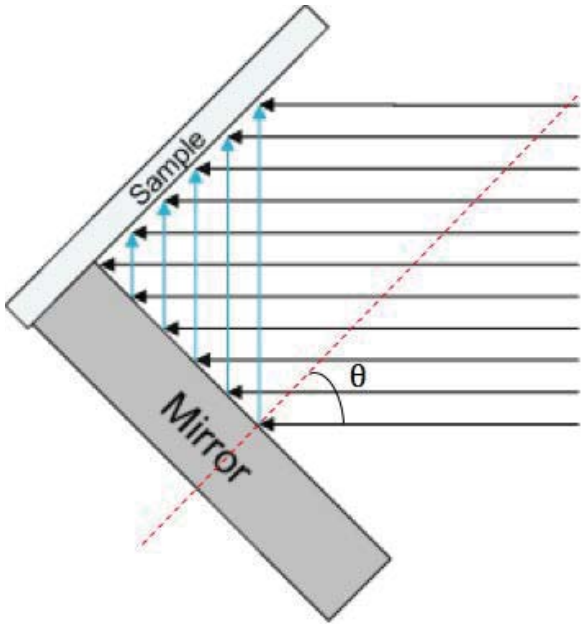

Figure 2.3: The Lloyd's Mirror setup uses a perpendicularly positioned mirror (to the sample) to reflect half of the incident light to the resist and interferences with the directly incident light, exposing the constructive interference areas.

destructive interference create a sinusoidal intensity pattern to expose valleys into the resist.

The Lloyd's Mirror interference lithography produces a fringe pitch:

$$\Lambda = \frac{\lambda}{2\sin\theta}(nm) \tag{2.2}$$

where Λ is the period of the grating created on the resist, λ is the wavelength of the incident light and θ is the incident angle.

The primary advantage of the Lloyd's Mirror is that the spatial period of the exposed gratings can be easily and continuously varied from many microns down to a half wavelength simply by rotating the stage without realigning the optical path. This has opened the door to new possibilities such as varied aspect ratio grids (different periodicities in the two axes of the grid) for patterned magnetic media and MRAM (Magnetic Random Access Memory) devices.

From equation 2.2, it is clear that the minimum spacing of the Lloyd's Mirror is half the wavelength but the minimum feature size can actually be made smaller than this by tuning the exposure conditions.

2.2 Sample Fabrication with EBL

Most of the samples used in this work were fabricated with electron beam lithography and focused ion beam lithography. Quartz, rather than the ordinary glass, was used as a substrate to minimize the absorption for the generated shorter wavelengths, and also for the consideration of any influence from possible luminescence. The task of nanofabrication is to produce hole arrays on $100nm$ gold films with about $800nm$ period. This fully defines the methods used in this work.

2.2.1 General Procedures of EBL

An electron beam lithography process usually includes all the following steps.

1. Substrate preparation

   Quartz slides were diced to about $12.5mm$ by $10mm$ for easy handling in the following fabrication and measurement steps. The diced chips were first cleaned with $RCA\ I$ for 15 minutes: $50ml\ H_2O_2 + 50ml\ NH_3OH + 250ml$ de-ionized water heated to 75 $^\circ C$. This is intended to remove any organic contamination from the substrates. After rinsing with DI water for couple of times, the chips were cleaned with $RCA\ II$ for another 15 minutes: $50ml\ H_2O_2 + 50ml\ HCl + 250ml$ de-ionized water heated to 75 $^\circ C$, which is intended to remove any inorganic contamination from the substrates. The chips were then DI water rinsed and blown dry with compressed N_2.

2. Metal film deposition

   5 $nm\ Cr$ was sputtered[67] as an adhesion layer because gold usually did not stick to quartz. Without breaking the vacuum of the sputtering chamber, $100nm$ gold film was sputtered on top of the thin Cr layer.

3. Resist application

   A small drop of Zep520A resist was dispensed on the metal film coated chip and the spinner was set to run at 6000 RPM for 1 minute. This results in a uniform resist film with a thickness of about $300nm$. The coated chips are then baked on a hot plate at 180 $^\circ C$ for $5 \sim 10$ minutes to drive off the excessive solvent. Zep520A was chosen in this work for the following reasons:

(a) Zep520A was developed as a replacement for PMMA resist.[68] It possesses as high resolution and high contrast as PMMA, and $10nm$ lines with $59nm$ pitch[69] have been obtained by using it.

(b) Zep520A has much higher sensitivity than PMMA. At $20kV$ acceleration voltage, its sensitivity is about $20 \sim 50\ \mu C/cm^2$, which is $5 \sim 10$ times higher than PMMA (about $50 \sim 100\ \mu C/cm^2$). This makes the exposure much faster and saves time since electron beam lithography is a very slow process.

(c) The most important reason for using Zep520A in this work is that its selectivity in plasma dry etching is comparable to most of novolak-based photoresists, which is at least five times better than PMMA.

4. Electron beam lithography

   The coated chips were then loaded into the SEM chamber to perform the electron beam lithography. The EBL system used at the University of Utah is a modified scanning electron microscope, $LEO\ StereoScan\ 440i$, equipped with a JC Nabity Lithography System.

5. Resist development

   After exposure with the electron beam, the chips were then dipped into the developer called $ZED-N50$, manufactured from the same company as ZEP520A, for 2 minutes, then rinsed with Isopropyl Alcohol (IPA) for 1 minute, and blown dry with compressed N_2. Only after this step done, it become safe to expose the chips to white light. Because ZEP520A is sensitive to white light, all the previous steps should avoid any white light exposure. During transportation, the chips should be wrapped with aluminum foils.

6. Gold film etching

   With the protection of the resist, Ar ion milling was carried out to etch away the exposed gold and finally created the needed hole arrays. We have found out that Cl_2 reactive ion milling (RIE) did not do a good job etching gold. As a matter of fact, Ar ion milling works much better since gold film is relatively soft. So far, we have not found a way to etch other denser films yet, such as Al.

7. Resist removal

   After Au was etched through, the resist was removed to expose the film and the etched structures. The chip was put into a stripper solution "$RemoverPG$" from MicroChem Crop, heated to 180 $^{\circ}C$ with a hotplate. Most of the resist should be stripped off and the heated solution could be placed in an ultrasonic bath for a few minutes if necessary. Rinse off any residue of the stripper with DI water, and sequentially rinse the sample with Acetone, Isopropyl Alcohol and Methanol for a couple of times, then blow dry with compressed N_2. This ends the sample fabrication process.

2.2.2 Problems with EBL

There are a few problems associated with the lithography and dry etching. Since the electron beam lithography involves many steps, there are problems associated with some of the fabrication processes. Almost all the problems are related to the etching process.

2.2.2.1 Choice of Resist

The unexposed resist served as a mask to etch the exposed area, and $300nm$ resist (like PMMA) usually can not last long enough to etch through $100nm$ gold film. On the other hand, the resist can not be made thicker since thicker resist will significantly reduce the resolution. This problem was overcome by utilizing Zep520A, which has much better etching resistance than PMMA.

2.2.2.2 "Enlarging" Effect

Figure 2.4 shows the "enlarging" effect caused by the dry etching process. The Ar ion milling is an isotropic process and when the charged ions hit the bottom of the holes, the ions that bounced back also hit the wall in all directions, which expanded the holes horizontally and made the holes much larger than they were originally written on the resist. This problem can not be avoided but only be slightly reduced by lowering the kinetic energy of the ions.

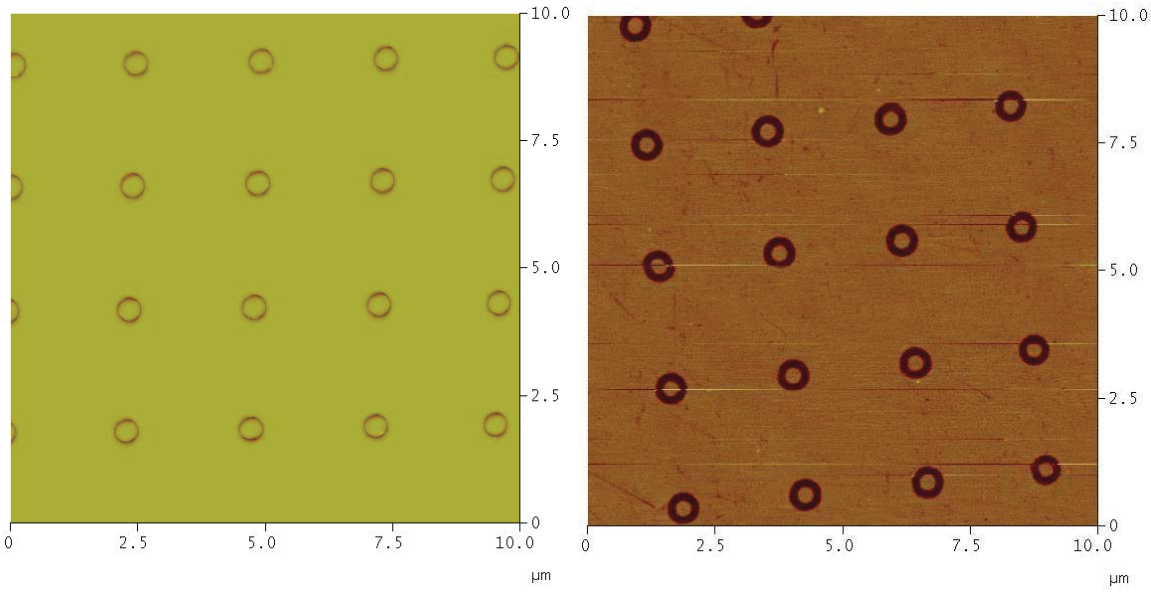

Figure 2.4: The AFM images showing the "enlarging" effect caused by the etching process, mainly by the wet etch process. The left image shows the AFM scan of "donut" structures right after resist development, and the right one shows the image with all the fabrication process was finished. The trenches have been largely expanded and it is very hard to control the exact width of the trenches with this fabrication technique.

2.2.2.3 Surface Contaminations

The more challenging problem is shown in Figure 2.5. During the etching process, some of the resists got refloated and resputtered on the metal surfaces. And some of the etched metal films also redeposited around the holes, forming a ring surrounding each hole. These deposition could not be stripped off by any means, such as heated strippers, ultrasonic bath orO_2 plasma, etc.

The solution to this problem is to use a sacrificial layer which will have all the resputtering materials deposited onto its surface, and it will take all the contaminations away upon removal, under wet etching. At the same time, this layer should also be hard enough to hold for a long time to mill through the gold films.

We have tested quite a few films, like SiO_2 and SiN_x, but we found Cr to be the best choice. Unlike SiO_2 and SiN_x, which are grown by $PECVD$ (plasma enhanced chemical vapor deposition) in a different machine at a high temperature (at 300 $°C$), one of the advantages of using Cr is that Cr can be sputtered in the same chamber without breaking vacuum. Another important factor is the Cr wet etchant etches Cr

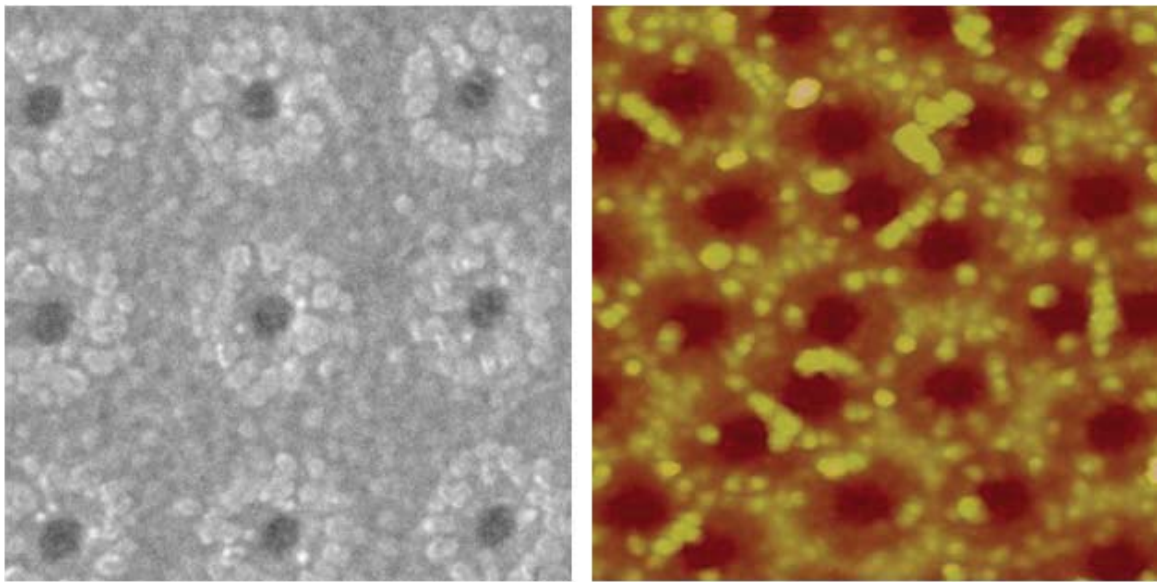

Figure 2.5: Images of finished all the fabrication processes. The surfaces of the gold film after removing resist show contaminations everywhere and a "ring" surrounding each hole. By comparing the left image in Figure 2.4, there are undesired deposits on the surface, and no good method to remove.

only and it has no effect on gold and quartz, but anything etching SiO_2 and SiN_x is likely to etch quartz. However, the potential problem is that the wet etchant may also attack the adhesion Cr layer. If other materials are used as the adhesion layer, this method will work better.

Based on the above discussions, we have chosen $20nm$ Cr as the hard mask. This hard mask layer was sputtered right after the $100nm$ gold film without breaking the vacuum.

2.2.3 Summary of EBL Process

With all the previous discussion in mind, the nanohole array fabrication process can be described by the following diagrams.

1. Substrate Preparation and Metal Films Deposition

   This step is shown in Figure 2.6.

2. Resist Application

   This step is shown in Figure 2.7.

Figure 2.6: $5nm$ Cr, $100nm$ Au and $20nm$ Cr are sequentially magnetron sputtered on the quartz substrate. The sputtering power is kept at 50 volts, Ar flow rate is 50%. Under such conditions, the sputtering rate for Cr is $14.1nm/min$, and Au is $22nm/min$.

Figure 2.7: The spinner was running at $6K\ RPM$ for 1 minute, and the resulting resist thickness is about $300nm$ (from AFM scan with big holes right after developing the resist). The chips were baked on a hotplate for $5 \sim 10$ minutes at $180°C$.

3. Electron Beam Lithography

   This step is shown in Figure 2.8.

4. Resist Development

   This step is shown in Figure 2.9.

5. Hard Mask RIE

   The hard mask reactive ion etch is shown in Figure 2.10.

6. Resist Removal

   This step is shown in Figure 2.11.

7. Ar Ion Milling

   This step is shown in Figure 2.12.

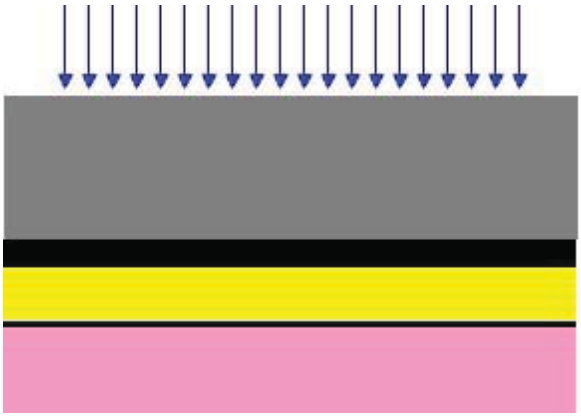

Figure 2.8: The resist was exposed during the electron beam lithography process inside the scanning electron microscope with magnification of 1000X, and the dosage was set to $0.2nC/cm$ (line dose).

Figure 2.9: The exposed samples were developed in $ZED-N50$ for 2 minutes, then rinsed in Isopropyl Alcohol (IPA) for 1 minute, and blown dry with compressed N_2. The written patterns are then transferred onto the resist.

Figure 2.10: Cl_2 reactive ion etching was used to transfer the patterns from the resist to the hard mask.This was performed on an Oxford 80 Plus RIE systems with Cl_2 flow rate at 20 $sccm$, and DC power at 300 W. The RIE rate for Cr is about 7 nm/min.

8. Cr Wet Etch

   This step is shown in Figure 2.13.

Figure 2.11: Resist was stripped off with "*RemoverPG*" at 180 $°C$ on a hotplate and may be assisted with ultrasonic bath.

Figure 2.12: Ar ion milling was then used to transfer the pattern from the hard mask to Au. The Ar gas flow was set to be 20 $sccm$, and with a DC power at $300W$. The etching rate for Au is about $25nm/min$.

Figure 2.13: The remaining Cr on top of Au was removed with wet etching of the Cr layer. All contamination on the Cr surface has been successfully removed and a clean surface with hole arrays has been obtained. At this point, there might be some undercuts for the adhesive Cr layer.

Figure 2.14 is some images taken with the samples fabricated with electron beam lithography. By comparing with Figure 2.5, it is clear that the surface is almost contamination free. But because of the etching process, we can not make very small holes, like holes with a diameter less than $100nm$. It is also very hard to make complicatedly shaped apertures rather than round holes, since any sharp edges will be rounded out during the etching process.

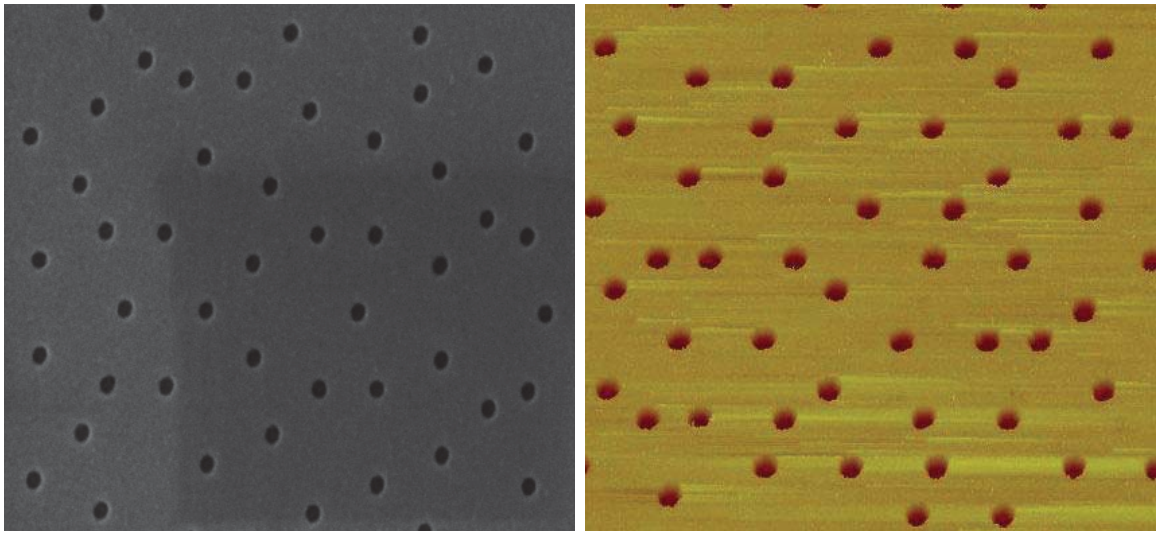

Figure 2.14: The SEM (left) and AFM (right) images of the same sample show that the surface is almost contamination-free.

2.3 Focused Ion Beam Lithography Fabrication

Focused Ion Beam (FIB) technology was developed for microelectronics in the semiconductor industry during the 1980s. The applications of FIB are mainly as a diagnostic tool for photomask repairing, device cross-sectioning, integrated circuit reverse engineering and restructuring, maskless implantation, transmission electron microscopy sample preparations [70] and ion beam assisted etching.

As a lithography technology, focused ion beam lithography is a much more straightforward method to make hole array samples and Figure 2.15 shows single trenched "Bow Tie" samples made with FIB. As also shown in Figure 2.16 and Figure 2.17, it is essentially one-step processing, and this is especially convenient to fabricate complicated aperture shapes.

Unlike the scanning electron microscope, the FIB uses a Gallium beam for imaging or drilling. Gallium is chosen because it is easy to build a gallium liquid metal ion source (LMIS). In a Gallium LMIS, gallium metal is placed in contact with a tungsten needle and heated. Gallium wets the tungsten, and a huge electric field (greater than 10^8 V/cm) causes ionization and field emission of the gallium atoms. These ions are then accelerated to an energy of $5 \sim 50$ keV, and then focused onto the sample by electrostatic lenses. Since FIB is using much heavier Gallium ions rather than nearly

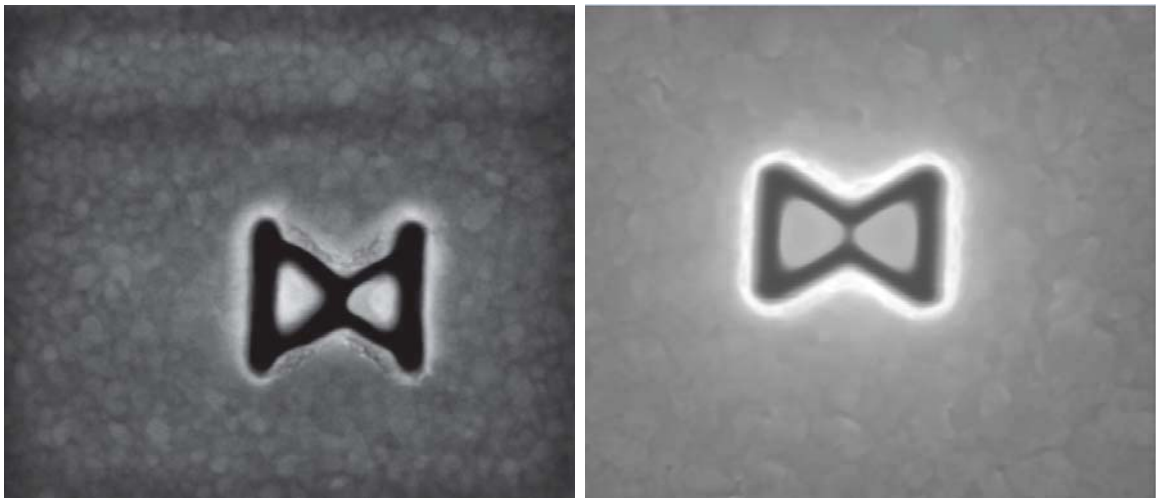

Figure 2.15: Trenched *Bowtie* structures made on $50nm$ Au film and on $50nm$ Al film fabricated with FIB. The gaps between the two metals can be fine tuned. These structures have to be made one by one with very low ion beam current.

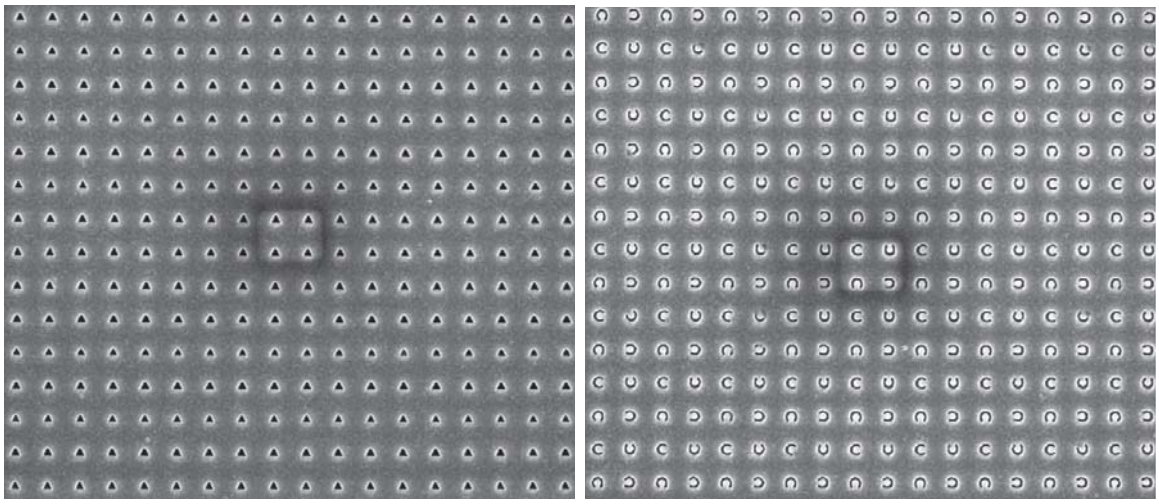

Figure 2.16: Square lattice triangular shaped hole array and "*C*" shaped hole array fabricated with FIB on $100nm$ Al films. The FIB is very capable of fabricating complicated aperture shapes because no chemical etching process is required.

weightless electrons, it is inherently destructive, and this makes FIB a perfect tool for drilling nanometer scale holes.

The software coming with the machine will transfer whatever you have designed to binary stream data, which will control when and where the ion beam is going to do the drilling job. After this drilling process, the sample is ready for use without any cleaning or chemical process, and this makes the fabricated samples almost

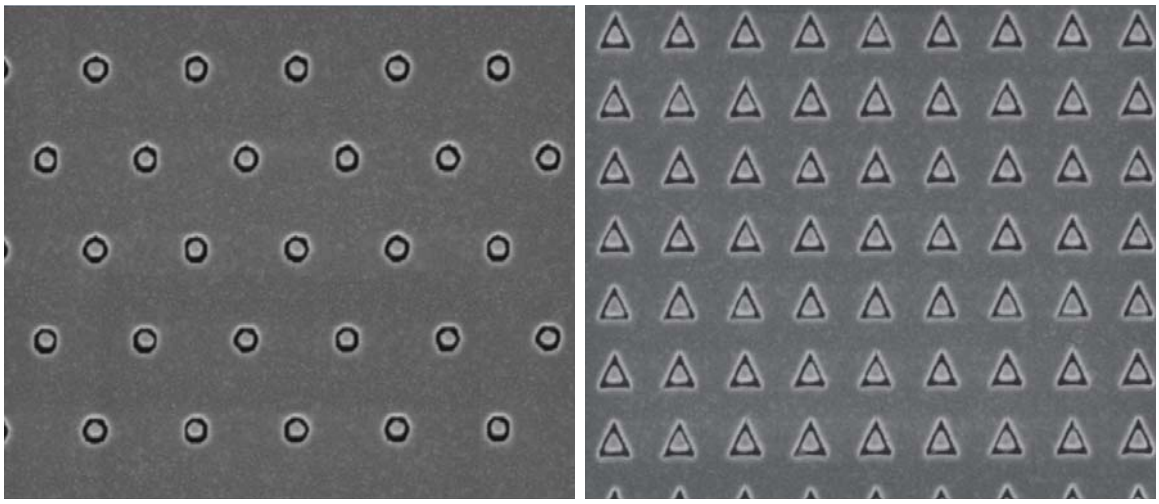

Figure 2.17: Triangular latticed annular round aperture arrays (left) and square latticed annular triangular aperture arrays (right) on $100nm$ Au film fabricated with FIB. Those annular apertures are believed to posses the capability of more than 90% transmittance[71] in the visible optical range, compared to about 10% to that of the regular hole arrays.

contamination free. Another advantage of the FIB fabrication is it does not care about the type of the metal to be drilled. If the metal film is soft materials, like gold, you can use very low current. For denser metal films like Al, the only parameter to change is to increase the beam current without losing too much resolution. This is also a pretty fast process. Typically, I have been choosing 10 minutes to make $25\mu m$ by $25\mu m$ hole arrays. With a dual-beam system, one can switch to electron beam to check how the drilling worked and make any necessary modifications immediately.

The major drawback of the FIB lithography comes from the data converting software. It can only handle a certain amount of data and that is why most of the hole arrays with about $800nm$ spacing is only about $25\mu m$ by $25\mu m$ in size, and this will make the following sample alignment more challenge.

2.4 Sample Characterization

The fabricated samples were usually characterized with SEM to find out the size of holes, the spacing of the lattice and the condition of the surfaces. Figure 2.18 shows an Atomic Force Microscope (AFM) image scan of the sputtered blanket Au

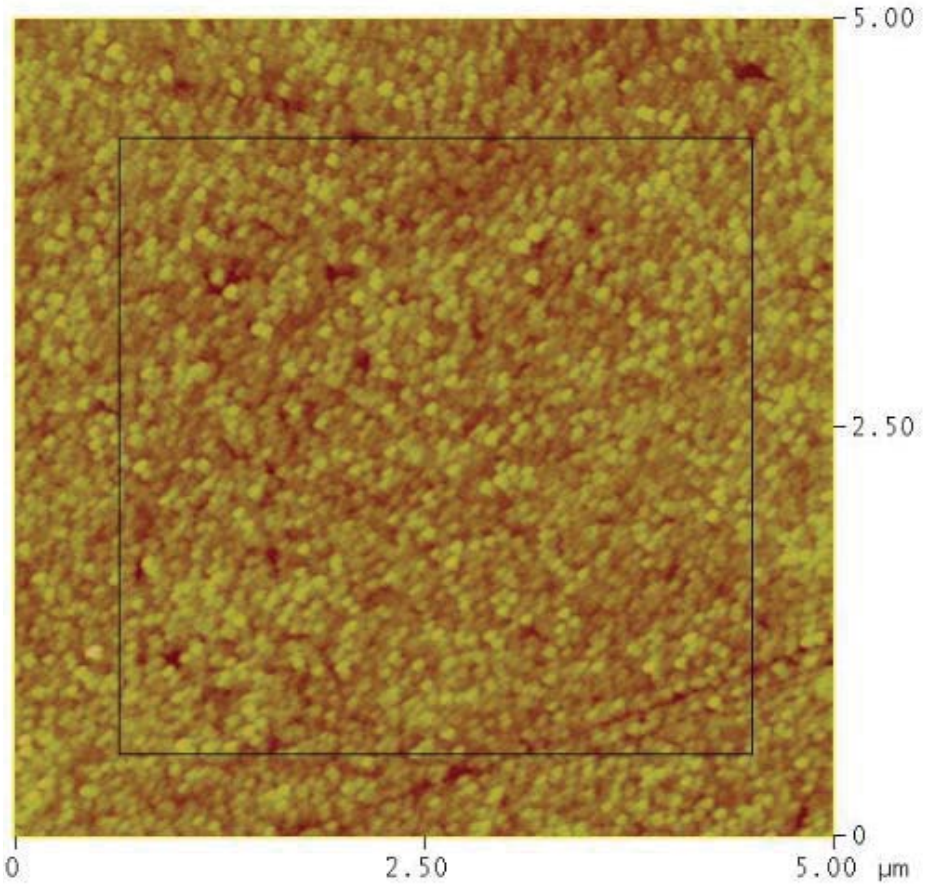

Figure 2.18: The sputtered blanket films we have used in this work generally have a roughness about 1 to 2nm RMS.

film to characterize its roughness of the surfaces. In general, the surface roughness of the as-deposited 100nm Au films is on the range of 1 to 2nm.

Sometimes, a white light optical spectrometer can also be used to characterize the optical properties before any nonlinear optical study.

2.5 Conclusions and Discussions

We have demonstrated our ability to fabricate subwavelength metallic hole arrays in the nanometer scale with decent quality. However, this is not the best way to do this job because electron beam lithography has involved too many etching processes and introduced too many uncertainties. As I have pointed out earlier, focused ion beam lithography can do a much better job on the hole array fabrication.

CHAPTER 3

MEASUREMENT TECHNIQUES

In this chapter, I briefly introduce the light sources and measurement techniques used in this work. Since the hole arrays fabricated with EBL and FIB are only hundreds of square micrometers, and in order to get high enough intensity, the incident laser has to be tightly focused into a spot $\sim 20um$ in diameter, to make sure all the incident light is hitting holes. This posed challenges to the measurements since our angular measurements are automated and require the sample to rotate with the axis centered right on the optical axis to maintain illumination on the same area. As a result, we have developed an alignment technique.

3.1 Light Sources

3.1.1 Ti:Sapphire Oscillator

One of the major requirements for nonlinear phenomena to occur is light of high intensity, and this is provided by a mode-locked Ti:Sapphire laser in this work. Titanium doped sapphire is a solid state laser medium capable of tunable laser operation over a broad range of near infrared wavelengths. Because of its broad absorption band in the blue and green pump, energy for the lasing process can be supplied by a standard frequency doubled $Nd:YAG$ or $Nd:YLF$ laser. The Ti:Sapphire laser we are using is a semiclosed oscillator system from Kapteyn-Murnane Laboratories L.L.C, pumped by a frequency doubled solid state laser from SpectraPhysics, Millennia V, at $532nm$. The mode-locked Ti:Sapphire has a repetition rate of around 80 MHz, and can produce about $400mW$ average power right after the exit mirror. A typical mode-locked spectrum is shown in Figure 3.1. The semiclosed system allows the operator to customize the operation of the oscillator but requires some skill to run it stably with relatively high power and a wide bandwidth.

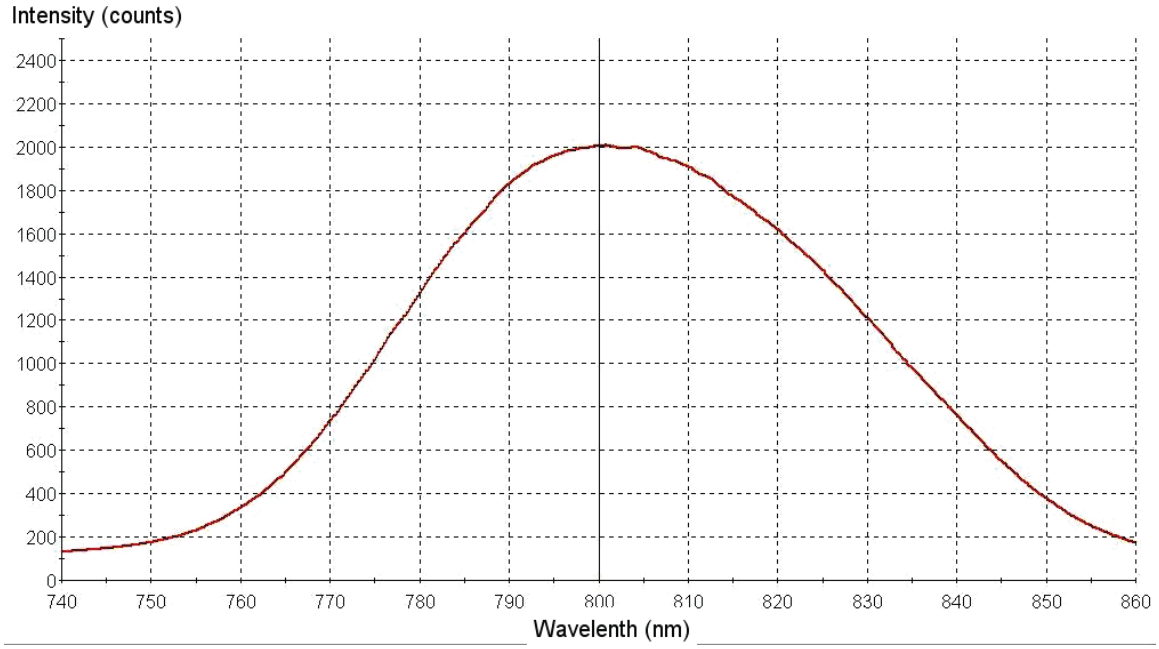

Figure 3.1: The spectrum of the output from the Ti:Sapphire oscillator shows the laser is running at $800nm$ wavelength with a bandwidth over $50nm$. The pulse duration was measured to be about $130fs$ (measured with FROG, refer to Figure 3.4) before prism compression.

3.1.2 Regenerative Amplifier

When the output from the oscillator is not intense enough even with the high peak power, an optical amplifier will then be used to amplify the power of the ultrashort pulses. The Spitfire Ti:Sapphire regenerative amplifier from *SpectraPhysics* can amplify a single pulse from an energy of nanojoules to over $1mJ$, which represents an overall amplification of greater than 10^6. Such a huge increase in peak intensity may exceed the damage threshold of most of the optics. So, a technique called Chirped Pulse Amplification is used to operate the amplifier without the risk of optical damage, and the illustration is shown in Figure 3.2.

This technique was originally developed for radar applications and involves temporally stretching the pulse, amplifying at reduced peak power, then recompressing the amplified pulse to close to its original duration.

The regenerative amplifier is usually running at a much lower repetition rate than the oscillator. In our case, it is running at $1kHz$. Because of this, some signal collection techniques had to be applied to retrieve the data.

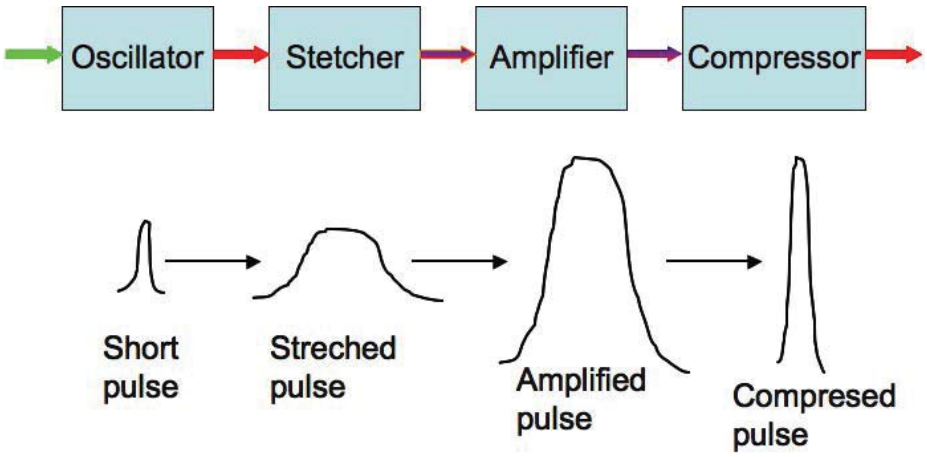

Figure 3.2: Principle of chirped pulse amplification: the low energy short duration pulse is initially stretched, by as much as 10,000 times, using a single grating pulse stretcher. A Ti:Sapphire regenerative amplifier increases the pulse energy up to 10^6 times. A single grating compressor then recompresses the pulse to near the original duration.

3.2 Pulse Characterization

The output pulse from the oscillator is in the femtosecond region, so it is difficult to characterize the pulse, because it is one of the shortest events in the world. However, people have developed a way to measure the ultrashort pulse by itself. This is called Frequency Resolved Optical Gating (FROG),[72] which is shown schematically in Figure 3.3.

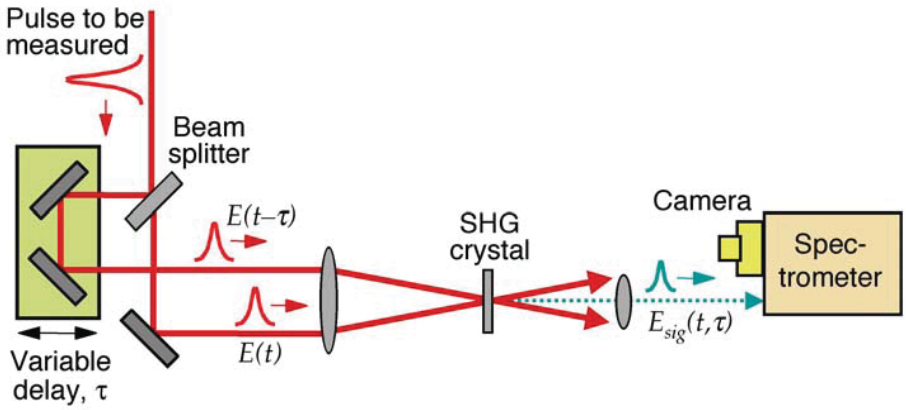

Figure 3.3: The optical path of the most common and sensitive version FROG: Second Harmonic Generation FROG. (Copyright permission of Professor Rick Trebino, Georgia Institute of Technology.)

The most widely used and most sensitive FROG is the second harmonic generation FROG. It uses the pulse to gate itself, and records the autocorrelation signal through a second harmonic generating crystal. The photodiode used for an autocorrelation setup is replaced with a spectrometer, so the spectrum of each delay time could be recorded. Then a two-dimensional map has been generated with x as delay time and y as wavelength. Figure 3.4 shows a typical uncompressed FROG trace acquired.

3.3 Prism Compressor

Almost all optical materials that are transparent for visible light have a normal, or positive, dispersion: the refractive index decreases with increasing wavelength. This means that longer wavelengths travel faster through these materials. Usually, there

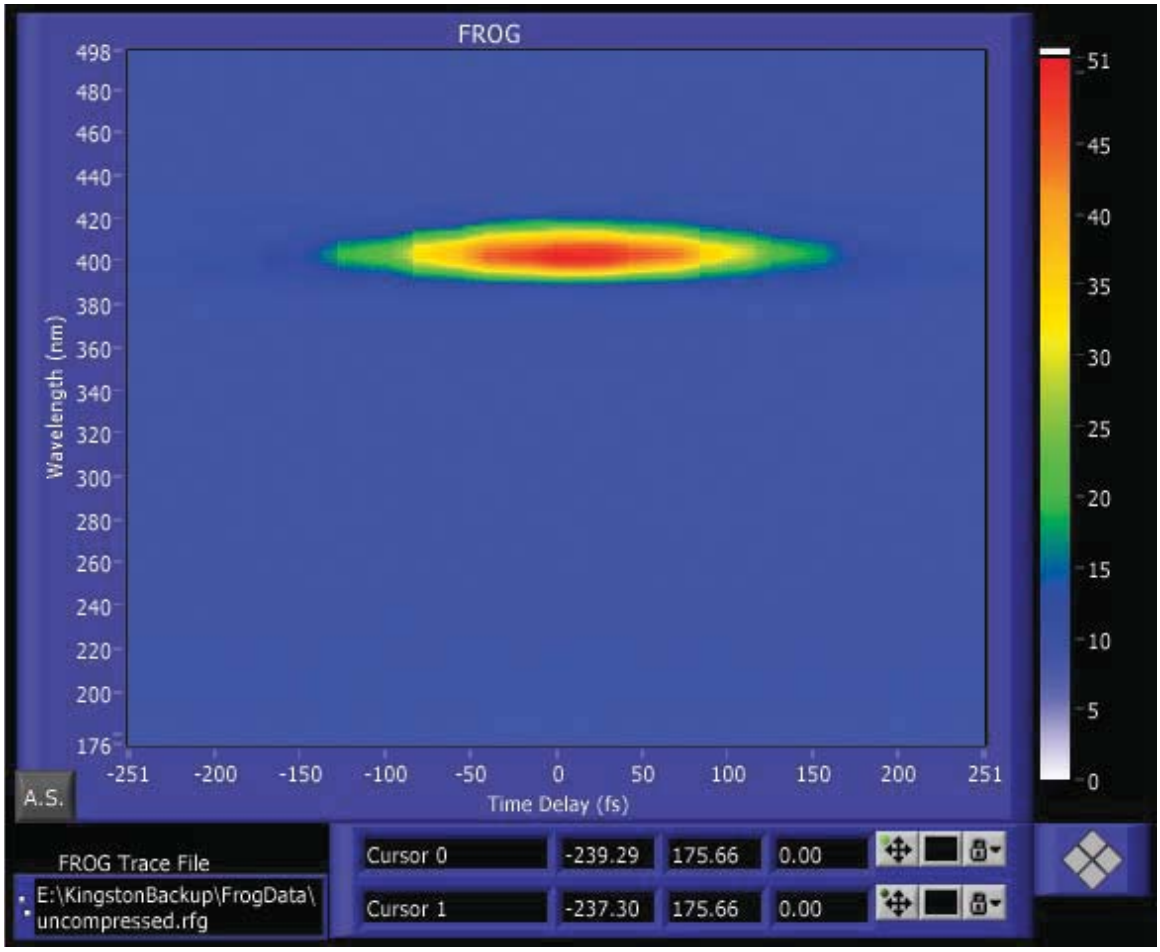

Figure 3.4: This picture shows an uncompressed FROG trace taken with the second harmonic generation FROG setup. The horizontal axis shows the time delay between the two beams and the vertical axis shows the spectrum at each time delay.

are tens of optics in any experiment setup before the laser beam hits the sample. The pulse of the output light from the oscillator is more than $125fs$. In order the get high peak intensity, a prism pair[73] [74] was used to provide a negative dispersion, and compress the pulse even shorter, typically to about $30fs$. Figure 3.5 shows a typical two pair prism set to compress optical pulses, and Figure 3.6 shows the FROG trace before and after the pulse compression.

3.4 Sample Alignment

Even though the output light from the Oscillator running at $800nm$ is visible when the intensity is high enough, it is still very hard to see diffraction patterns after passing through the hole arrays since only about 1 percent of the incident light can pass through. Also the diffraction pattern is the only way to tell if the sample has been well aligned. So, a He:Ne laser running at $633nm$ was aligned to be collinear with the $800nm$ laser for this purpose, and there is no worry about sample damage.

Figure 3.7 shows the actual setup used for all the experiments included in this work: a translational stage is fixed on the optical table and can only travel in the direction perpendicular to the laser beam. Then, the rotational sample stage has been installed on top of the translation stage and a second rotational stage (detector stage) is stacked onto the sample stage with an opening in the middle so that the

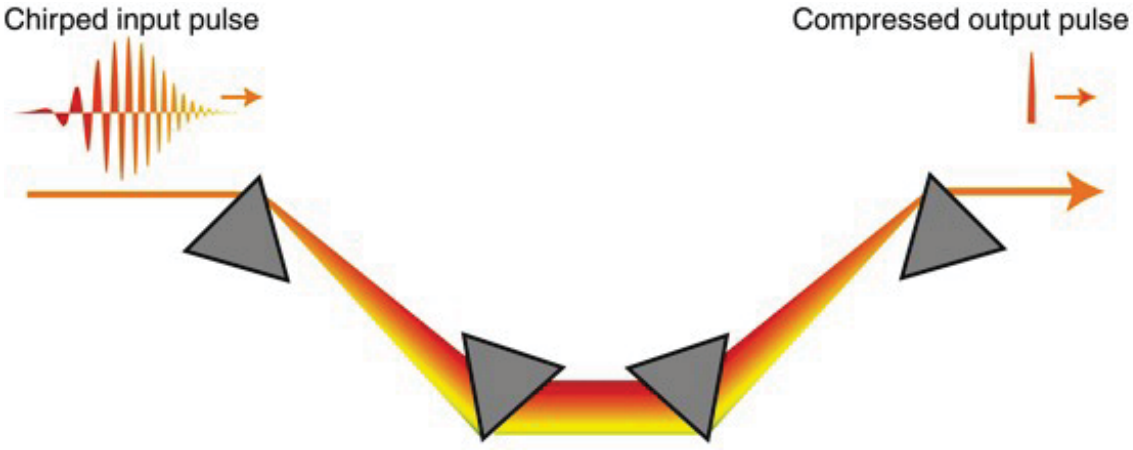

Figure 3.5: The Prism Compressor consists of four prisms with light incident and exit with *Brewster's* angle. (Copyright permission of Professor Rick Trebino, Physics 6567, "Ultrafast Optics", Spring 2007, Georgia Institute of Technology.)

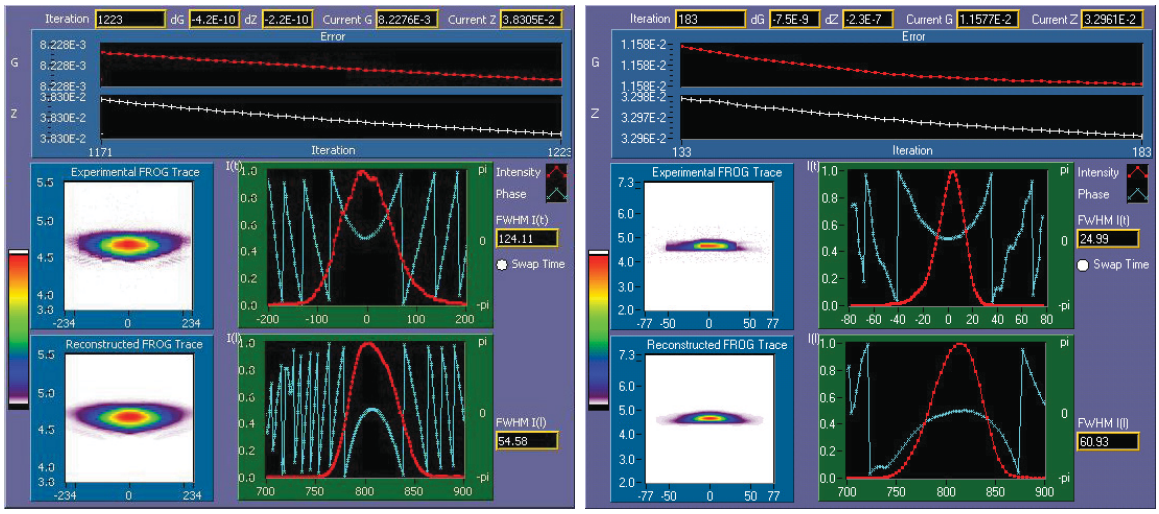

Figure 3.6: The FROG traces for the pulse before (about $125fs$) and after the prism compressor (about $25fs$).

sample holder can extend through the detector stage. A post is screwed to the center of the sample stage and another stage which is capable of moving vertically is screwed to the other side of the post and provides freedom to change the height of the sample. A two-dimensional translation stage is then mounted onto it. All the stages had been aligned to be as concentric as possible. The entire sample holding system is then mounted on top of the two-dimensional translation stage.

The first step of alignment is to make sure the sample is standing vertical. This can be achieved by observing the reflection of the red laser spot through a fully collapsed iris through which the incident laser comes in. Then by adjusting the height and moving the knobs of the top translation stage, the diffraction pattern will show up indicating one array has been aligned to the laser.

The next step is to make sure the array on the sample is placed parallel to the optical table. The hole arrays were fabricated on a piece of quartz slide with dimensions of about $12.5mm$ by $10mm$, and the hole arrays are only about $80\mu m$ by $80\mu m$ for the ones made with EBL, and only about $25\mu m$ by $25\mu m$ for the ones made with FIB. When nanofabrication was performed under the scanning electron microscope with the lowest magnification (in our case, it is about 50x), it is almost impossible to align the array to be exactly parallel to the edge of the quartz slides. This problem has been overcome by using a specially designed sample holder which

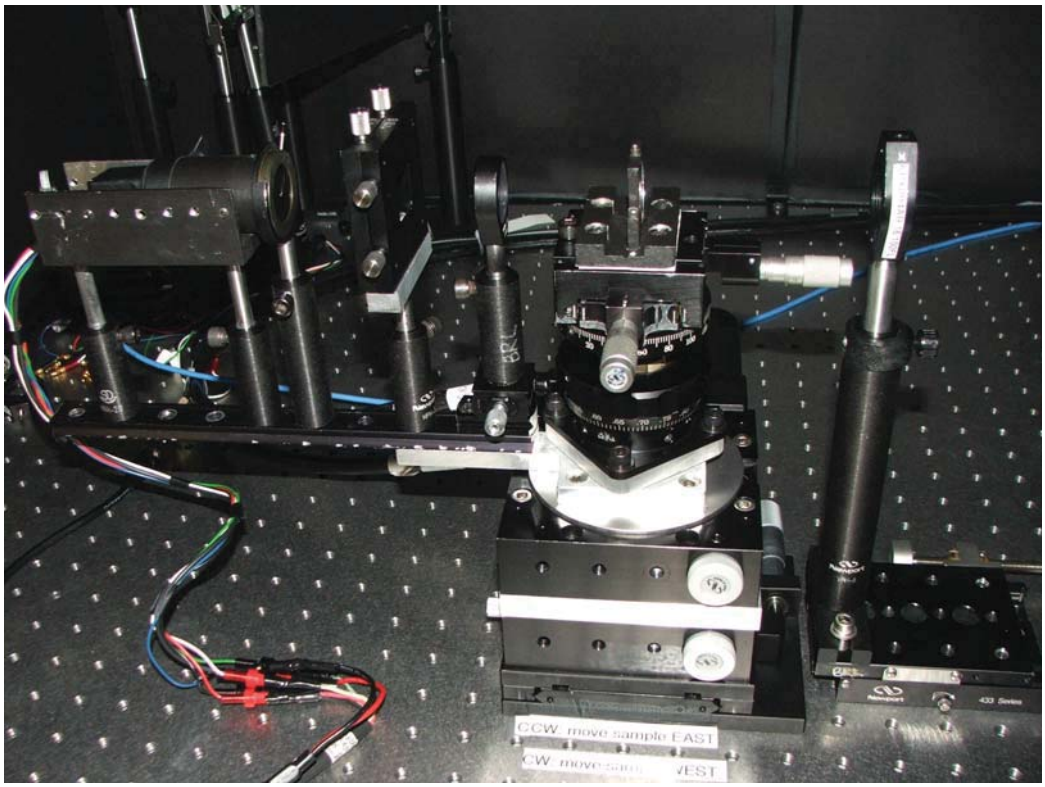

Figure 3.7: A photo shows the actual experiment setup used in this work. From right to left (along the laser propagating direction), focusing lens, sample holder and assembly, collecting lens, adjustable slit, iris, filters and PMT. All the detection components are mounted on a bar and can rotate a very large angle. On the sample holder and assembly part, from bottom to top, one direction translation stage, sample rotation stage, detection rotation stage, vertical translation stage, two-dimensional translation stage, adjustable sample holder which is capable of rotating with any angle within a plane and slightly tilting both horizontally and vertically.

has the capability to rotate and tilt to or away from the incident laser. Placing a white card far away enough from the sample, the transmitted first order diffractions an be detected. A constant height of the diffraction orders is the indication that the sample has been properly leveled.

After this preliminary adjustment, the hole array should be kept engaged with the incident beam for any angle to which the rotational stage that houses the sample turns. This has to be guaranteed when automatic measurements are performed. In order to do this, two translation stages, two rotation stages and a vertical stage are used to build up the measurement setup.

The following diagrams demonstrate the alignment procedure. In general, a white card is placed on the back of the sample. The He:Ne laser was first used to align the sample. Then, it was replaced with the $800nm$ laser from the oscillator and the following alignment procedure has to be carried out again for any possible deviation of the two optical axises. This time an infrared viewer is used to monitor the transmitted diffraction order. The brightest diffraction is considered to be the standard for best engagement at any sample angle.

1. The sample is mounted and adjusted as described earlier. Quite possibly, the center of the rotation stage, the sample and the beam will not be overlapped for each other at the position indicated as the blue dot, as shown in Figure 3.8.

   The goal of the alignment is to bring the rotation center and sample to the focal point of the laser. By only adjusting the top two-dimensional translation stage, the hole arrays can be moved to engage with the laser beam with the help of the diffraction order.

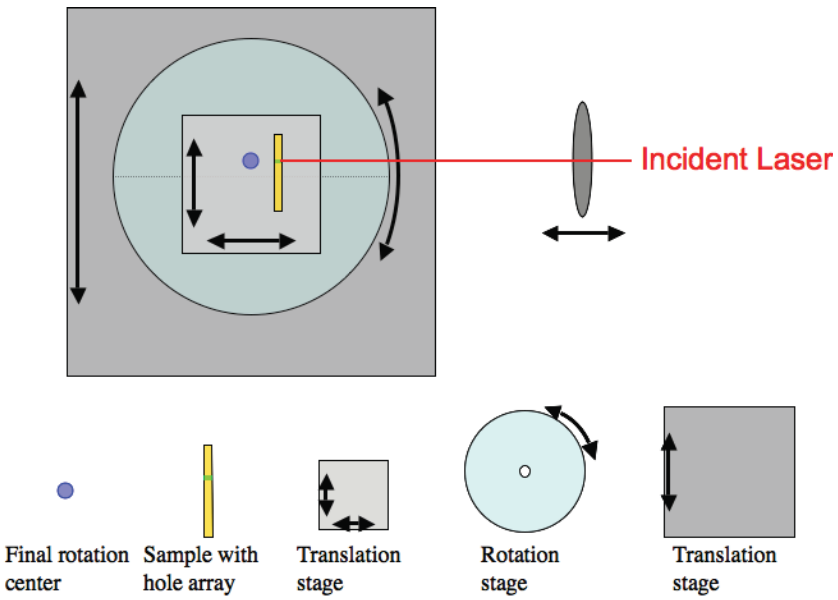

Figure 3.8: The sample has been inserted into the sample holder and engaged with the laser beam. At this point, only the top translation stage has been used. The vertical moving stage is not shown here because it is fixed with the rotation stage and only affects the height of the sample. The two-way arrows indicate the possible moving direction for each stage, and one-way arrows are used to tell the actual moving direction of that step.

2. Turn the rotation stage clockwise (in our case, turn the stage towards the operator). Since the hole array is on the rotation center, it will move away from the laser, and the diffraction order will be dimmed out (Refer to Figure 3.9).

3. Use the bottom translation stage to move the sample to the laser beam. Since everything above is stacked, moving this stage moves everything in the setup. This also brings the rotation center of the sample stage closer to the ideal rotation center (refer to Figure 3.10).

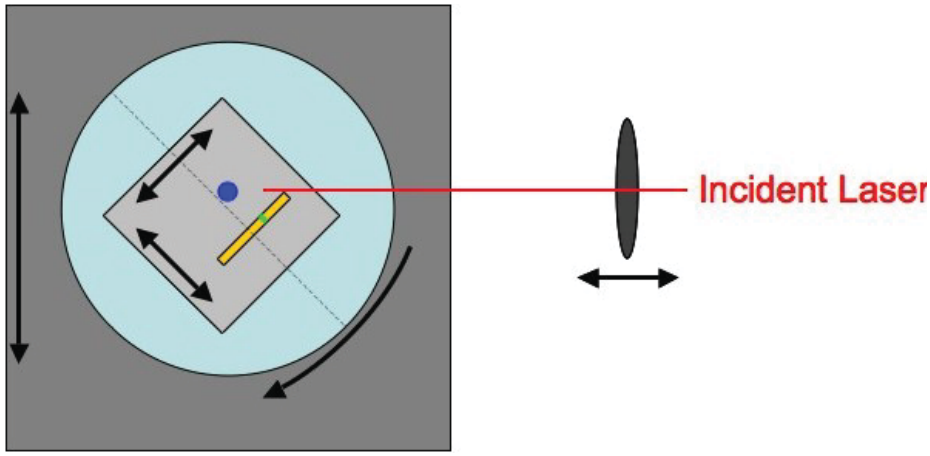

Figure 3.9: Turning the rotation stage clockwise disengages the hole array from the laser beam.

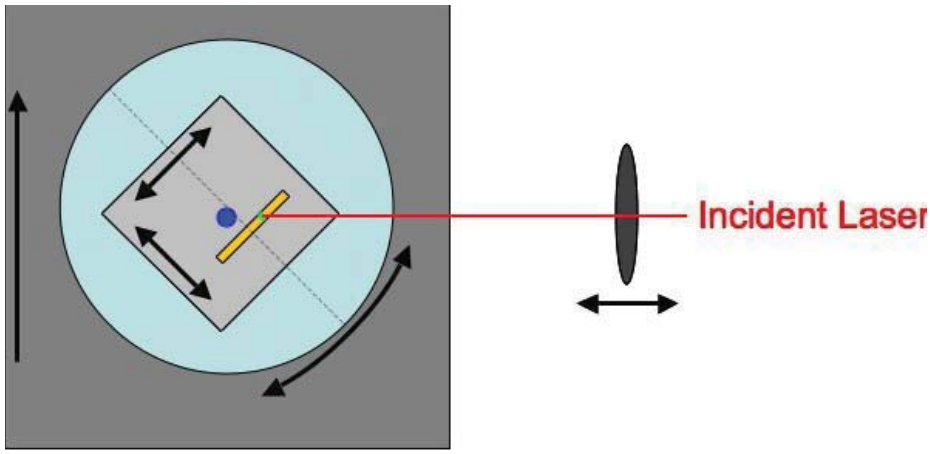

Figure 3.10: Move the bottom translation stage up and engage the hole array to the laser beam. This will bring the rotation center of the sample stage and sample closer to the final rotation center.

4. Turn the sample stage counterclockwise till the sample is at normal incidence. Again, the sample might have lost engagement with the laser beam (refer to Figure 3.11).

5. Use the top two-dimensional translation stage to bring the sample to be engaged with the laser beam. We found out that it is necessary to always use the vertical knob to engage the sample whenever the sample is turned towards the normal incidence position (refer to Figure 3.12).

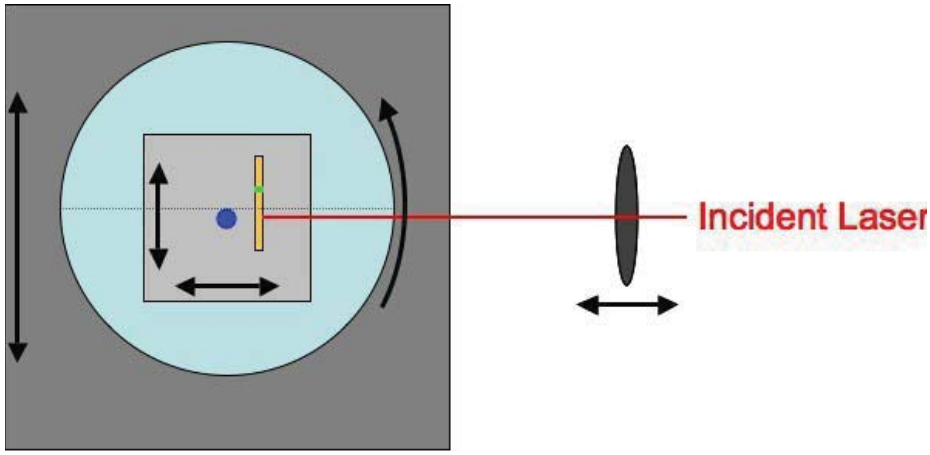

Figure 3.11: Turning the sample stage counterclockwise will disengage the hole array from the laser beam again.

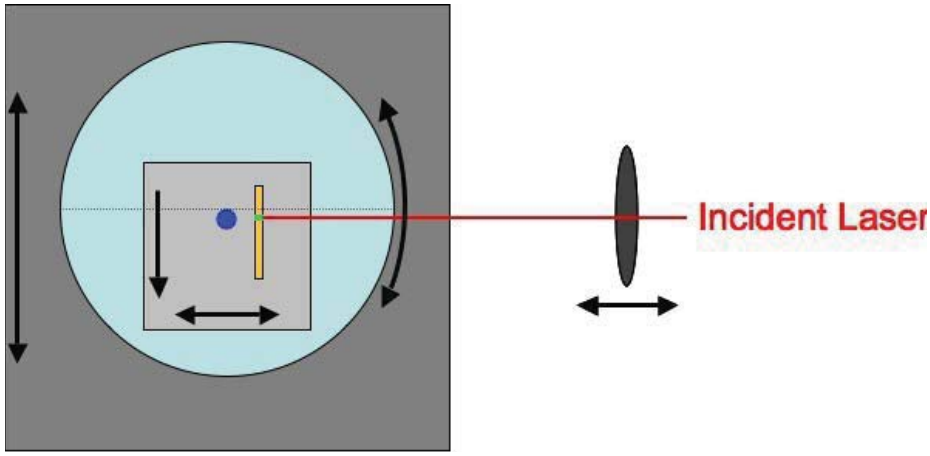

Figure 3.12: The vertical knob of the top two-dimensional translation stage is used to bring the sample to engage with the laser beam.

6. Keep turning the sample rotation stage counterclockwise after the sample passes the normal incidence position (refer to Figure 3.13).

7. Use the horizontal knob of the top two-dimensional translation stage to bring the hole array to the laser beam. And we also found out that this is the only time this knob should be used. From the diagram, the hole array is getting much closer to its final position (the blue dot) (refer to Figure 3.14).

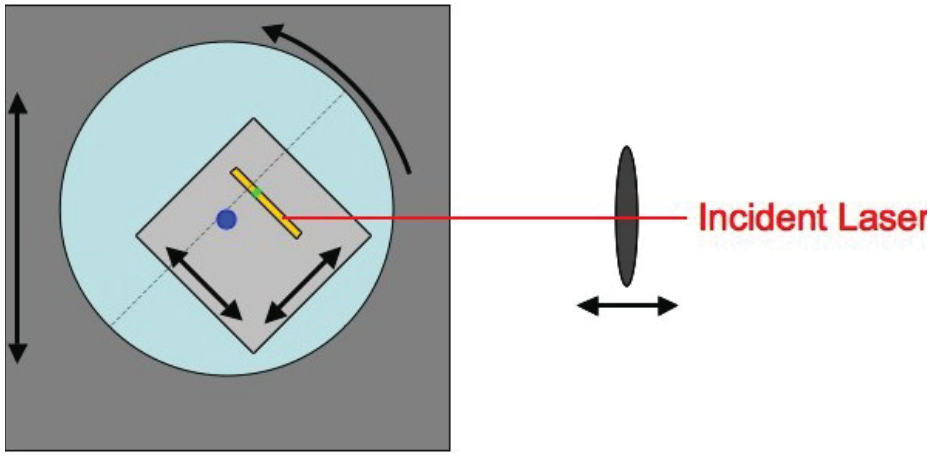

Figure 3.13: The sample will lose engagement again because the rotation center of the sample stage is still off from the final rotation center.

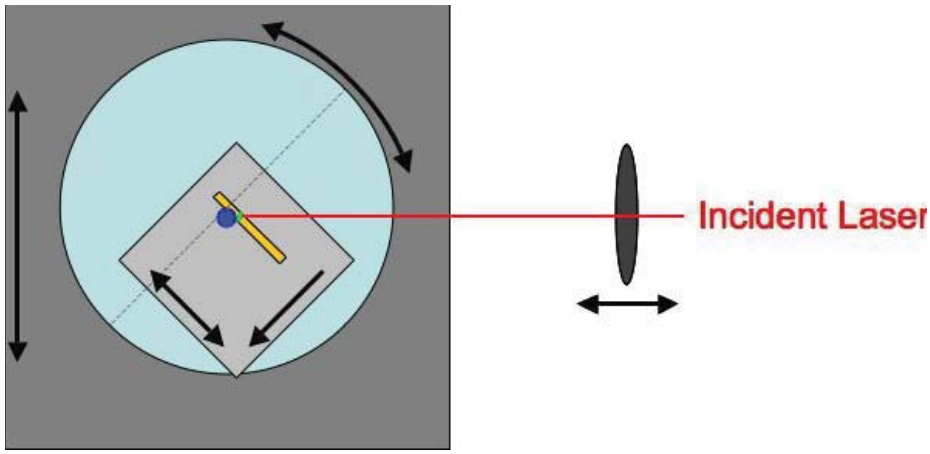

Figure 3.14: The horizontal knob of the top two-dimensional translation stage is used to engage the hole array to the laser beam.

8. Turn the sample stage clockwise towards the normal incidence position (refer to Figure 3.15).

9. Use the vertical knob of the top two-dimensional translation stage to bring the hole array to the laser beam. As stated earlier: always use the vertical knob to engage the sample whenever the sample is turned towards the normal incidence position. This finishes one whole iteration of the alignment procedure. It is clear that after one whole trip, the hole array is getting much closer to its final position if it is still not aligned perfectly well (refer to Figure 3.16).

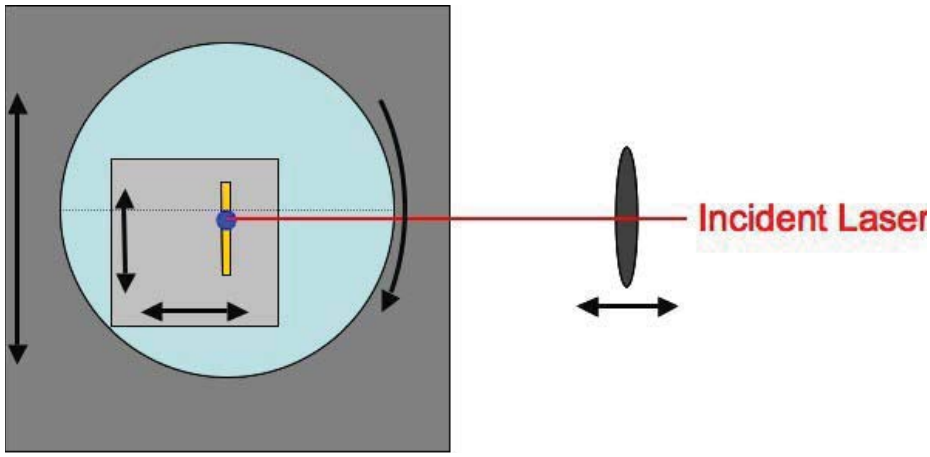

Figure 3.15: Turning the sample stage back to the normal incidence position.

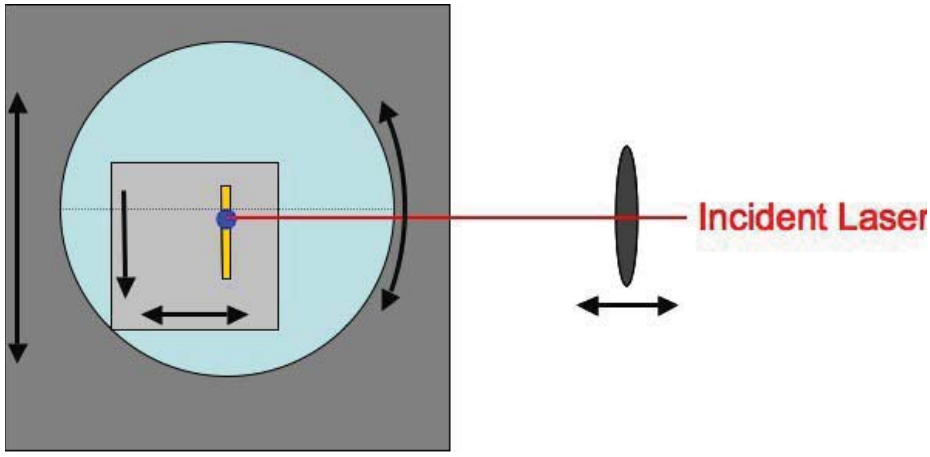

Figure 3.16: Use the vertical knob of the two-dimensional translation stage to engage the laser beam. This brings the setup to its original position but with much better alignment.

10. Repeat step 2 to step 9 if it is necessary.

11. The rotation center of the sample stage, the hole array and the focusing point of the laser beam are aligned to the final rotation center, as schematically shown in Figure 3.17.

Once this is achieved, the bottom translation stage can be locked down. If a new sample is needed, adjusting only the top translation stage with the proper knob while rotating the sample stage will bring the sample to the focal point of the laser beam, because the rotation center of the sample stage is already in the final rotation position.

The above shown procedure is just one method to achieve the alignment, and surely there are other ways doing this. For example, the first step would not necessarily to be rotating the sample stage clockwise. But one thing to keep in mind is: the correct translation knob should be used according to turning direction of the rotation stage.

3.5 Detection Techniques

3.5.1 Consideration of Filters and Signal Recovery

We have measured second harmonic generation at $400nm$, third harmonic generation at $266nm$, and more ambitiously, we have tried to measure supercontinuum

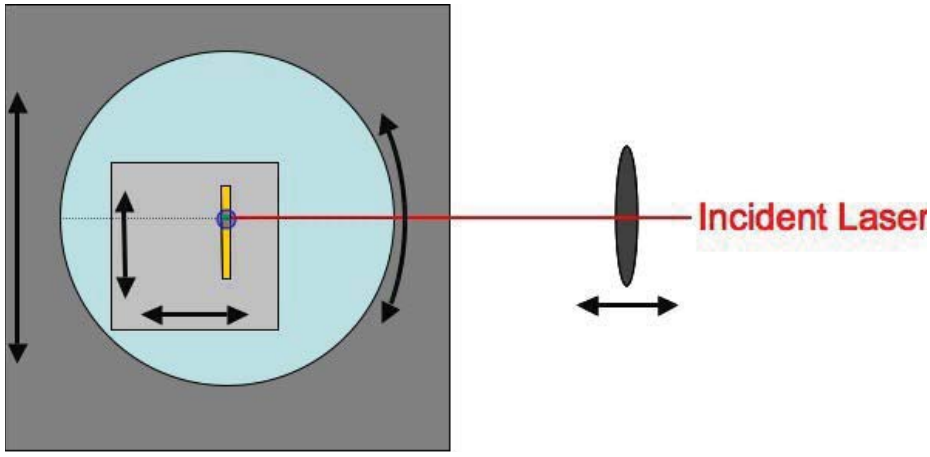

Figure 3.17: In its final position, the rotation center, the hole array and the stage center should be virtually in the same position. Turning the rotation stage any direction will not disengage the hole array and the laser beam.

generation at $450nm$, $500nm$, $550nm$ and $600nm$. Since the converting efficiency is extremely low for these nonlinear processes, the transmitted fundamental light is a big challenge for measuring the output light. Low pass filters have been used to block out the transmitted fundamental $800nm$ light but let the shorter wavelengths pass through. During most of all the measurements, a glass color filter with proper cutoff frequencies has also also been used to further block out the $800nm$ light, of course, with the price of attenuating the desired wavelength. Finally, a bandpass filter with $40nm$ bandwidth is used to select the wavelength of interest. A PMT (photo-multiplier tube) is used to collect the generated wavelength, and send the signal to an ADT converter, such as Lock-in amplifier or Boxcar integrator, which is connected to a computer.

All the nonlinear processes have been generated through the output of an oscillator and a regenerative amplifier, respectively, for different purposes. Since the oscillator is running at about $80MHz$ and the regenerative amplifier is working at $1kHz$, the detection techniques are totally different. After an incident pulse hits the sample, the generated nonlinear signal will last about $20\mu s$. In the case of the oscillator, there is a pulse impact on the sample about every $10ns$. Therefore, compared to $20\mu s$, the nonlinear signal is generating continuously. But in the amplifier case, in only one millisecond, there is one pulse that comes in. Even though its peak power is higher than the oscillator pulse, the signal will be quickly diminished and undetectable. Based on this, a Lock-in amplifier was sensitive enough to recover the signal in the oscillator case but a Boxcar integrator is necessary to collect the signal when the regenerative amplifier was used.

3.5.2 Angular Spectrum Measurement

Once the sample has been properly aligned, the measurements can then be carried out. For all the measurements we have done, the incident light has been fixed and impinged on the sample through an achromatic focusing lens. By rotating the sample and keeping the detection arm aligned with the incident light, we can measurement the angular dependence of the transmitted fundamental light by using an ordinary

light detector and nonlinearly generated signals with the combination of filter sets and PMTs.

3.5.3 Radiation Pattern Scan

Parking the sample stage at a fixed position and scanning the detection arm from one side of the sample to the other side allows us to study the distribution of the transmitted signals. Either the transmitted fundamental light or the generated shorter wavelength lights can be scanned. If we perform the same detector scan for each sample angle, we can generate a two-dimensional map of the transmitted light. This will help us better understand the spatial behavior of the transmitted light.

CHAPTER 4

SECOND HARMONIC GENERATION FROM SUBWAVELENGTH METALLIC HOLE ARRAYS

Historically, second harmonic generation is as old as nonlinear optics. In 1961,[75] P.A. Franken, A.E. Hill, C.W. Peters and G. Weinreich, using a Ruby laser of 694.3nm wavelength with approximately 3 joules energy in $1ms$ pulses, successfully generated second harmonic from a quartz sample for the first time. This opened a brand new arena for optics – nonlinear optics.

In principle, second harmonic generation is prohibited from centrosymmetric materials. For square lattice round hole arrays, there is inversion symmetry with respect to a normally incident laser. However, by varying the incident angle or the detection angle, we can break the local symmetry of the aperture. Furthermore, we can also engineer the arrangement of the apertures to break the symmetry introduced by the lattice. Finally, we can even break the symmetry of the aperture itself by making the apertures in a shape having no symmetry at all.

In this chapter, we study the optical second harmonic generation from subwavelength metallic hole arrays. All the hole arrays used in this chapter were designed to have an average period of $800nm$, and are fabricated with the method described in Chapter 2, with $5nm$ Cr as an adhesion layer, and about $100nm$ Au film on top of quartz slides.

4.1 Symmetry Issues of Second Harmonic Generation

As one of the most important optical properties of a medium, the nonlinear susceptibility tensors have certain forms that reflect the structural symmetry of the

medium. Accordingly, some tensor elements vanish and some are related to each other, greatly reducing the total number of independent elements.

Each material has certain point symmetry with a group of symmetry operations $\{S\}$ under which the medium is invariant. Therefore, the $\chi^{(n)}$ remains unchanged. In the case of second order nonlinearity, S is a third-rank (three-dimensional) tensor with 27 elements. Then, the invariance of $\chi^{(2)}$ under a symmetry operation is explicitly described by,

$$(\hat{i} \cdot S^{\dagger}) \cdot \chi^{(2)} : (S \cdot \hat{j})(S \cdot \hat{k}) = \chi^{(2)}_{ijk} \tag{4.1}$$

n such equations exist for a medium with a symmetry group that consists of n symmetry operations. Equation 4.1 yields many relations between various elements of $\chi^{(2)}$, even though only a few of them are independent. These relations can be used to reduce the 27 elements to a smaller number of independent ones.

An immediate consequence of equation 4.1 is that $\chi^{(2)} = 0$ in the electric dipole approximation[76] for a medium with inversion symmetry: with S being the inversion operation, $S \cdot \hat{e} = -\hat{e}$ ($\hat{e}$ represents $\hat{i}$, $\hat{j}$ and $\hat{k}$), then $\chi^{(2)}_{ijk} = -\chi^{(2)}_{ijk} = 0$. This explains why second harmonic generation can not exist for systems with inversion symmetry.

From the above analysis, the key to generate second harmonic signal out of those symmetric systems is to break the symmetry. We had designed and built some special experimental setups described in the following section to archive this goal.

4.2 Experimental Setup

Figure 4.1 shows the schematic experiment setups used in this work. As detailed in Chapter 3, the only difference between the two setups is the light source and the ADC converter. When the oscillator is used as the light source, a lock-in amplifier is sufficient to detect the signal. But if light from the oscillator is amplified through a regenerative amplifier, a Boxcar amplifier has to be used to collect the data.

During the measurements, the incident power of the unamplified case is about $75mW$, while when using the amplifier, the average incident power was constrained to be lower than $0.5mW$ due to the 1KHz repetition rate. Our experience shows that the samples could have been severely damaged if higher incidence power had been used.

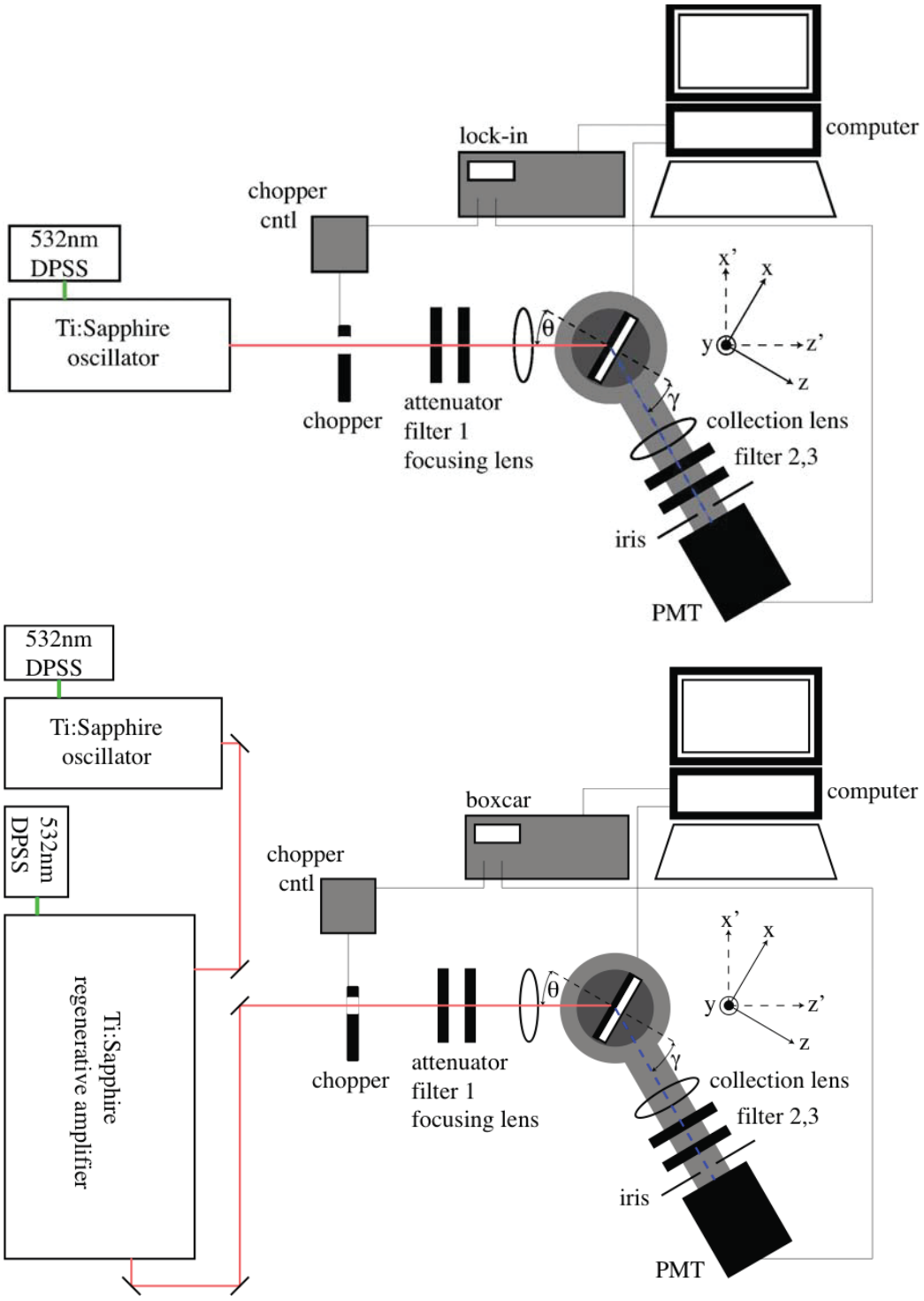

Figure 4.1: The schematic of the experimental setups used for this work. The top shows the setup when the oscillator is used as the light source and the bottom one shows the setup with the regenerative amplifier. The inset shows the coordinate system used for the measurements, where x' denotes the polarization direction of the incident laser, z' denotes the propagation direction. xy plane denotes the sample plane. θ is the incident angle and γ is the detection angle. As illustrated, θ is positive and γ is negative.

4.3 Intensity Buildup Inside Apertures

$FDTD$ calculations with the commercial package from Lumerical Solutions, Inc. were used to find out what was happening inside the apertures with light illuminating from the top. In this calculation, the coordinate system is as shown in the inset of Figure 4.1, where x is the polarization direction of the incident laser, y is along the vertical direction and z is the propagation direction of the incident laser. The aperture is chosen to be $250nm$ in diameter, the film is designated to be $100nm$ thick gold film with $5nm$ chromium adhesion layer to mimic the samples used in this work.

The left column of Figure 4.2 shows the top view of the x, y and z components of the intensity pattern at normal incidence, taken at a position $5nm$ below the aperture entrance. It is very clear that at normal incidence, E_x dominates along the x axis, and E_y dominates along the diagonal direction, suggesting that a local second harmonic signal can arise from the surface $\chi^{(2)}$ component between gold and air.

The right column of Figure 4.2 shows the cross-section view of the x, y and z components of intensity distribution along the height of the aperture, and a $5nm$ indention is also shown on the aperture bottom to mimic the Cr undercut caused during the wet etch process. It is clear that almost all the field inside the aperture is concentrated at the entrance and exit. Even though E_y seems to more uniform along the wall of the aperture, its overall magnitude is almost negligible.

The intensity buildup inside the aperture at normal incidence is then symmetric with respect to the incident and detection directions. Even second harmonic signals can be generated locally at the aperture entrances and exits due to local intensity buildup, but for a whole aperture, the signals will be canceled out by the opposite locations, then the signal from one single aperture is zero. For an array of such apertures, the overall output of second harmonic generation is zero.

As the sample was rotated away from 0° to 30° (Figure 4.3), then to 60° (Figure 4.4), the field distributions for x and z components are no longer symmetric, even though the y component still retains its mirror symmetry. This indicates that the effective $\chi^{(2)}$ is not zero any more. Also, the intensities for different positions are getting larger and larger, potentially suggesting the nonlinear response at higher angle is getting stronger as the sample moves away from the normal position.

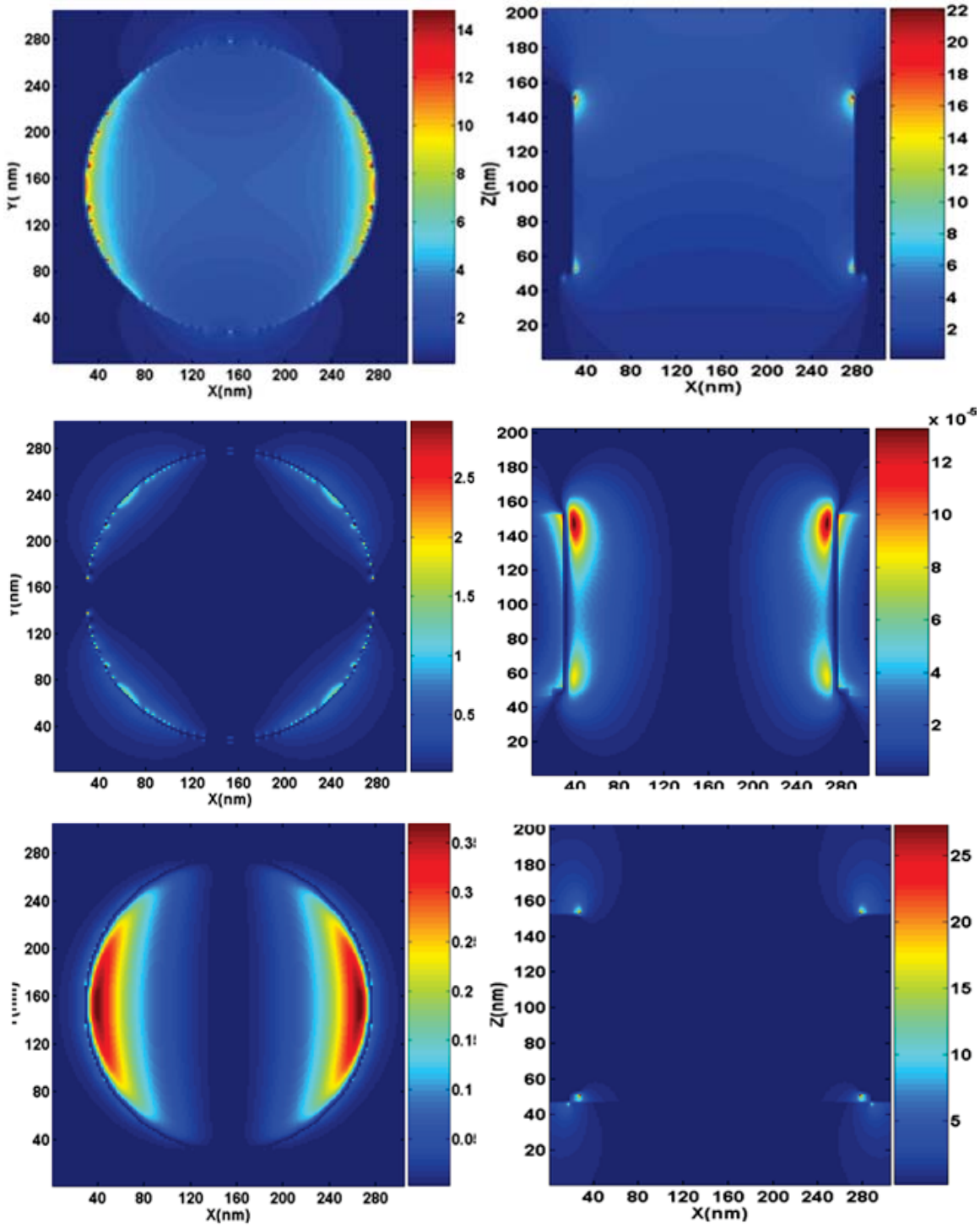

Figure 4.2: (Reprinted with permission from Xiaojin Jiao) Top-down view (left column) and cross-section view (right column) of the intensity distribution inside the aperture at normal incidence. From top to bottom for the left and right columns, the pictures show the intensity $|E_x|^2$, $|E_y|^2$ and $|E_z|^2$ inside the aperture respectively.

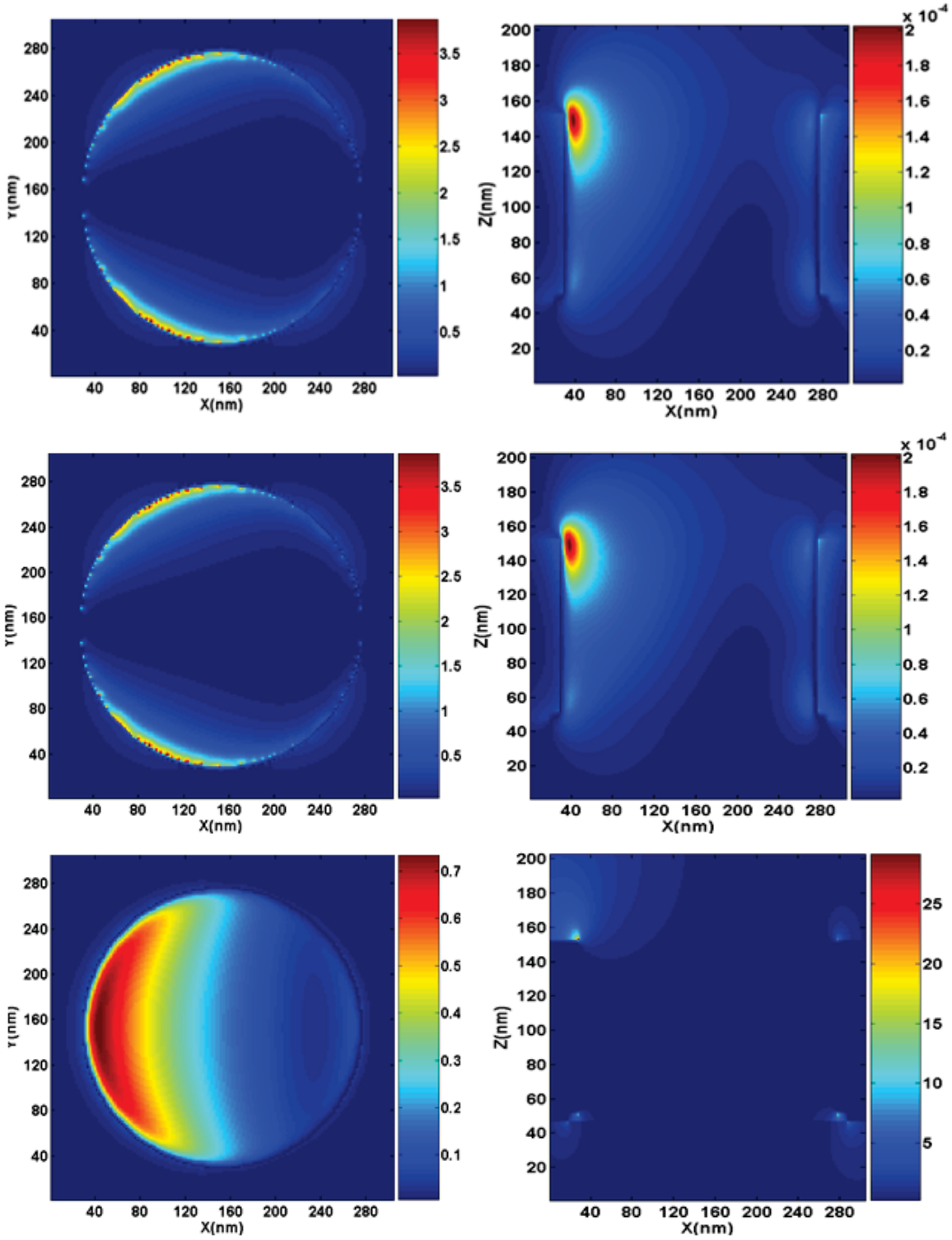

Figure 4.3: (Reprinted with permission from Xiaojin Jiao) Top-down view (left column) and cross-section view (right column) of the intensity distribution inside the aperture at a 30 degrees incidence angle.From top to bottom for the left and right columns, the pictures show the intensity $|E_x|^2$, $|E_y|^2$ and $|E_z|^2$ inside the aperture, respectively.

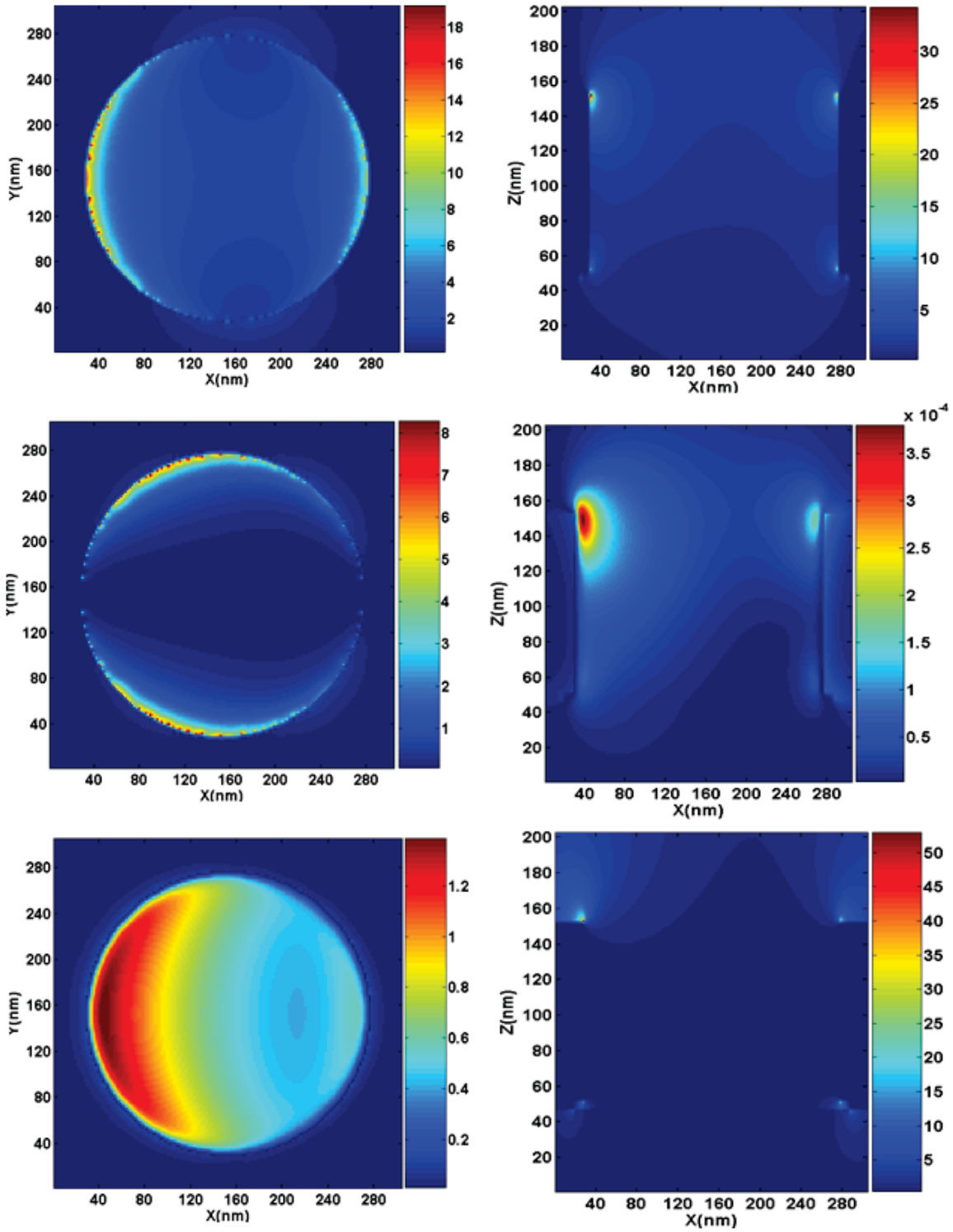

Figure 4.4: (Reprinted with permission from Xiaojin Jiao) Top-down view (left column) and cross-section view (right column) of the intensity distribution inside the aperture at 60 degrees incidence angle.From top to bottom for the left and right columns, the pictures show the intensity $|E_x|^2$, $|E_y|^2$ and $|E_z|^2$ inside the aperture, respectively.

4.4 Second Harmonic Generation from Periodic Round Hole Arrays

We have started our second harmonic generation study with the square lattice round hole arrays since this is the simplest case. The first and most important impression of Figure 4.5 and Figure 4.6 is the well-defined peaks both for fundamental transmission and second harmonic generation. According to surface plasmon theory, the fundamental transmission peaks are defined by the resonance of the surface wave. For almost all our experimental results, the second harmonic signal always peaks near the fundamental peak locations.

4.5 Verification of Second Harmonic Generation

Even though we have shown quite a lot results of our second harmonic generation studies, there is still a fundamental question that needs to be answered: are we really measuring the signal at the second harmonic wavelength? The most direct way would be to put a spectrometer to read the wavelength directly, but this is not realistic because the generated second harmonic signal is so weak we have to use PMT to detect it. Fortunately, except for using the combination of the filter set to

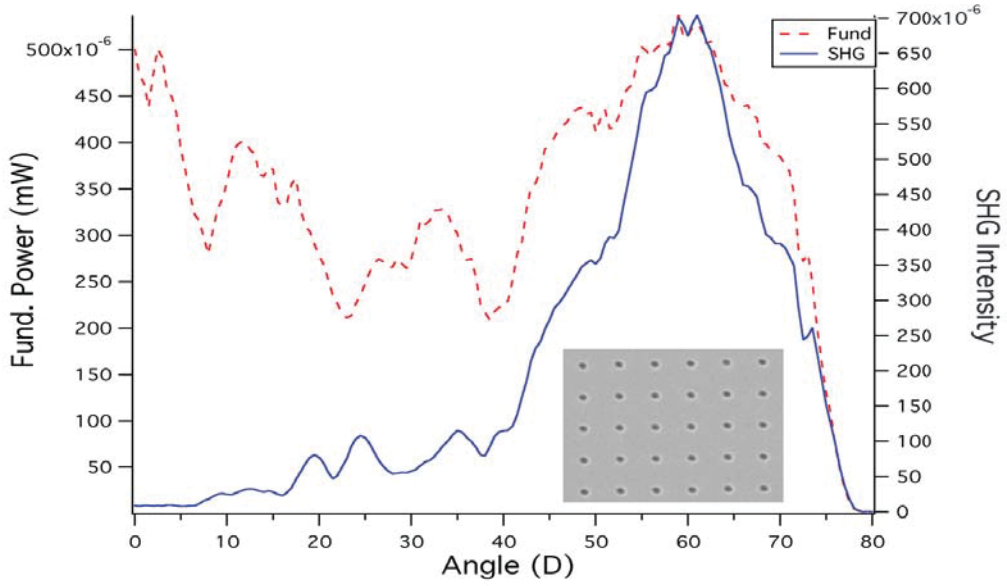

Figure 4.5: A square lattice round hole array fabricated with electron beam lithography (inset) and its transmitted fundamental and second harmonic signals, excited by a TM incident light.

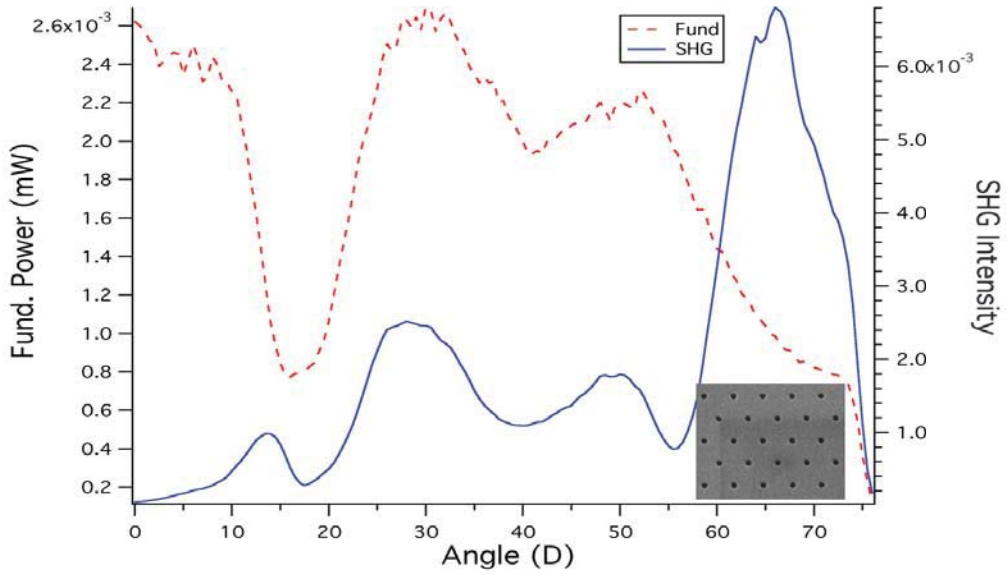

Figure 4.6: A triangular lattice round hole array (inset) and its transmitted fundamental signal and second harmonic generation, excited by a TM incident light.

ensure the right wavelength, we have some other ways to verify we are doing things right. We have chosen a square lattice asymmetric hole array for the verification of second harmonic generation signals. One of the reasons is it generates quite a strong signal at normal incidence and this simplifies the calculations quite a bit. We have also chosen a nonzero position to verify our results. Although these studies are only performed on a specific sample, the results should be applicable for all the samples.

4.5.1 Power Dependence of Second Harmonic Generation

Second harmonic generation intensity is proportional to the second power of the incident light according to the classical nonlinear theory.[2] Under the undepleted wave approximation, the generated second harmonic signal will have the intensity of,

$$I_2(z=l) = \frac{2\omega_3^2 d_{eff}^2}{n_1^2 n_2 c^3 \epsilon_0} l^2 I_1^2 \left[\frac{sin\Delta kl/2}{\Delta kl/2}\right]^2 \tag{4.2}$$

Therefore, if we plot the measured signals with the corresponding incident power, there should be a power 2 relationship between them.

The plot and the fitting in Figure 4.7 clearly show that the measured signal does have a second order power dependence to the incident laser power.

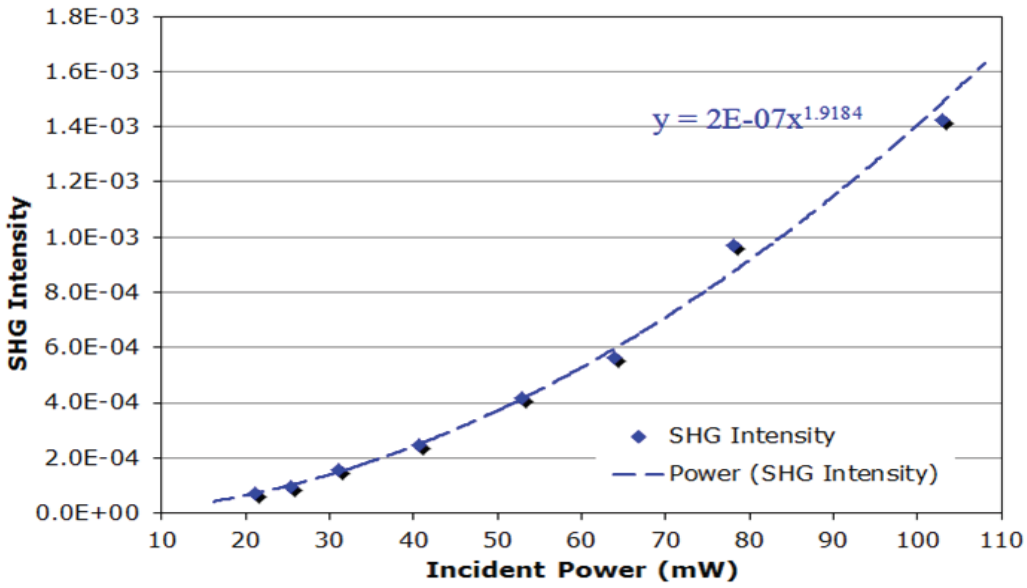

Figure 4.7: Power dependence of second harmonic generation from a square lattice asymmetric hole array with the hole array sitting at 45 degree, one of the second harmonic generation peak positions.

4.5.2 Angular Distribution of Second Harmonic Generation

For surface plasmons on a two-dimensional lattice, the momentum conservation is given by,

$$\vec{K_{sp}} = K_x\hat{x} + iG_x\hat{x} + jG_y\hat{y} \tag{4.3}$$

where K_{sp} is the surface plasmon wavevector, $K_x = (2\pi/\lambda)sin\theta$ is the component of the wavevector of the incident light that lies in the plane ($\theta = 0$ for normal incidence), G_x and G_y are the reciprocal lattice vectors of the two-dimensional photonic crystal, and i and j are integers. In the case of a square lattice with lattice constant a_0, the reciprocal lattice vectors are simply $G_x = G_y = 2\pi/a_0$, and the conservation of momentum is given by

$$|K_{sp}| = \left[\left(\frac{2\pi}{\lambda}sin\theta + i\frac{2\pi}{a_0}\right)^2 + \left(j\frac{2\pi}{a_0}\right)^2\right]^{1/2} \tag{4.4}$$

On the other hand,

$$|K_{sp}| = \frac{2\pi}{\lambda}\left(\frac{\epsilon_d\epsilon_m}{\epsilon_d + \epsilon_m}\right)^{1/2} \tag{4.5}$$

where ϵ_d is the dielectric constant of the medium in contact with the metal and ϵ_m is that of the metal.

Combining equation 4.4 and 4.5, we have the angular position of the extraordinary transmission for the fundamental light.

$$sin\theta = -i\left(\frac{\lambda_0}{a_0}\right) \pm \sqrt{\frac{\epsilon_d \epsilon_m}{\epsilon_d + \epsilon_m} - \left(\frac{j\lambda_0}{a_0}\right)^2} \tag{4.6}$$

where i, j are also called mode numbers.

Figure 4.8 shows the angular distribution of the transmitted fundamental signal peaks, corresponding to the different modes from two different interfaces.

Even though equation 4.6 has been derived for fundamental transmission, it also very well describes the location of the second harmonic generation peaks from our experiments.

Wood's anomaly can also be used to describe the valleys of the fundamental transmission. Using the same idea for momentum conservation, the angular distribution of valley positions can be described by the following equation,

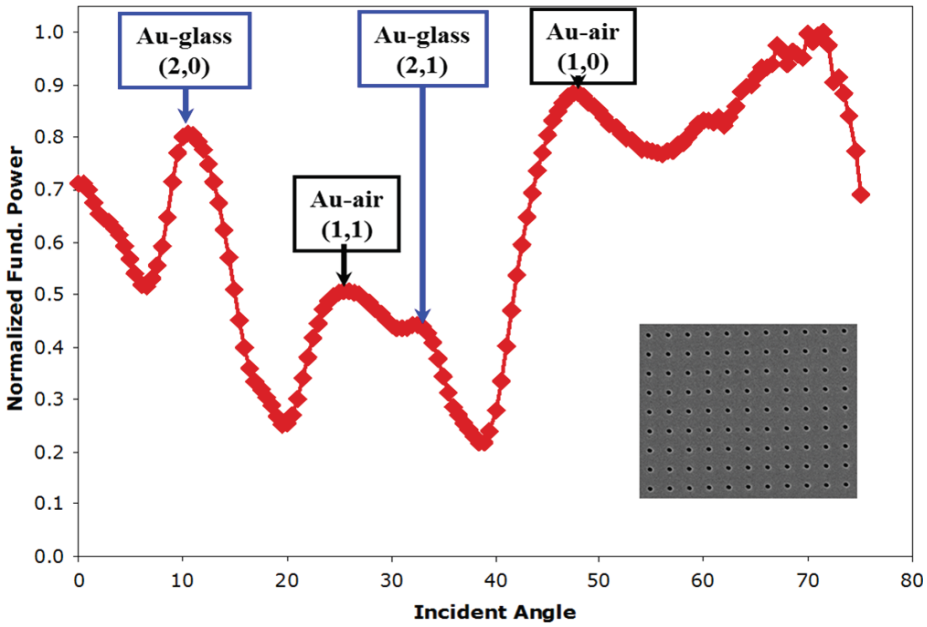

Figure 4.8: Angular distribution of the extraordinary transmitted fundamental power from an array of round holes. Different peaks originate from different interfaces (Au-air or Au-glass), and are well defined by equation 4.6.

$$sin\theta = -i\left(\frac{\lambda_0}{a_0}\right) \pm \sqrt{\epsilon_d - \left(\frac{j\lambda_0}{a_0}\right)^2} \tag{4.7}$$

where i, j are mode numbers.

Figure 4.9 shows the angular distribution of the transmitted fundamental signal valleys, corresponding to the different Wood's anomaly modes from two different interfaces.

Accordingly, the fundamental valley positions should also correspond to second harmonic generation valley positions.

Even though the peak position calculation is only performed for fundamental light, from the $FDTD$ calculation and the experimental results, we can say that upon the condition of enhanced light transmission, optical intensity buildup inside aperture occurs, so the second harmonic generations also peak at the corresponding positions. But the second harmonic generation is way more sensitive than fundamental, there are also places the second harmonic generation don't peak up but the fundamentals do.

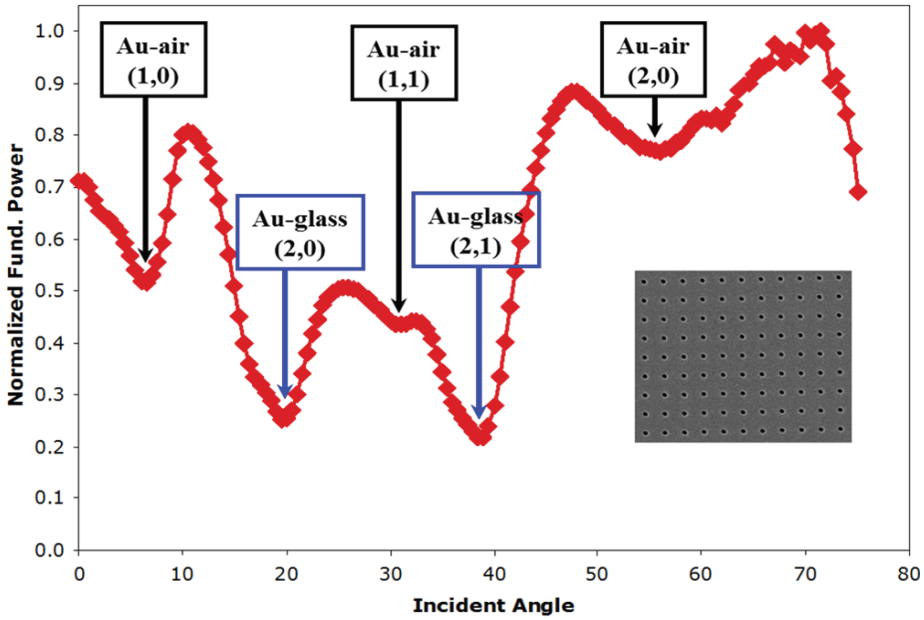

Figure 4.9: Angular distribution of Wood's anomaly from an array of round holes. The valley positions are associated with different interfaces (Au-air or Au-glass), and are well defined by equation 4.7.

4.5.3 Diffraction Pattern of Second Harmonic Generation

Another way to verify if the measured signals are second harmonic or not is from the diffraction pattern. The detected far-field radiation pattern is the result of sources of second harmonic radiation which are periodically arranged. From this standpoint, the second harmonic wavevector satisfies the following momentum matching condition:

$$K_t^{2\omega} = 2K_t^{\omega} + mG \tag{4.8}$$

It is assumed that, at the second harmonic wavelength, there is no coupling between the apertures due to the surface waves, because the surface plasmon polariton propagation distance is less than the aperture spacing.[77] If the second harmonic SPP were not negligible, additional phase matching considerations would come into play.[83] For the square lattice, and assuming that the optical wavevectors have only $\hat{x}$ and $\hat{z}$ components, equation 4.8 can be written as:

$$sin\gamma = sin\theta + m\frac{\lambda}{2a_0} \tag{4.9}$$

As shown in Figure 4.5, this equation closely describes the trajectories of the second harmonic generation peaks.

Table 4.1 gives the diffraction peak positions of the calculated and measured values shown in Figure 4.10. The measurements and the calculation matched very well.

The choice of incident angle at zero degree may cause some confusion if the equation 4.9 only works for the normal incidence. To clear this ambiguity, we have also chosen another incident angle at -24 degrees and repeated the same plotting and

Table 4.1: Diffraction peak positions for the second harmonic generation for a square lattice metallic hole array. The sample was sitting at zero degree, so θ is 0. The lattice constant a_0 was fitted to be $880nm$ even though it has been designed to be $800nm$. The wavelength used here is $800nm$. All calculations are based on equation 4.9. The angles θ and γ are shown in Figure 4.1. The numbers shown on first row are diffraction orders.

θ=0	-2	-1	0	1	2
Calculated γ	-65.4	-27.0	0	27.1	65.4
Measured γ	-65	-27	0	27	65

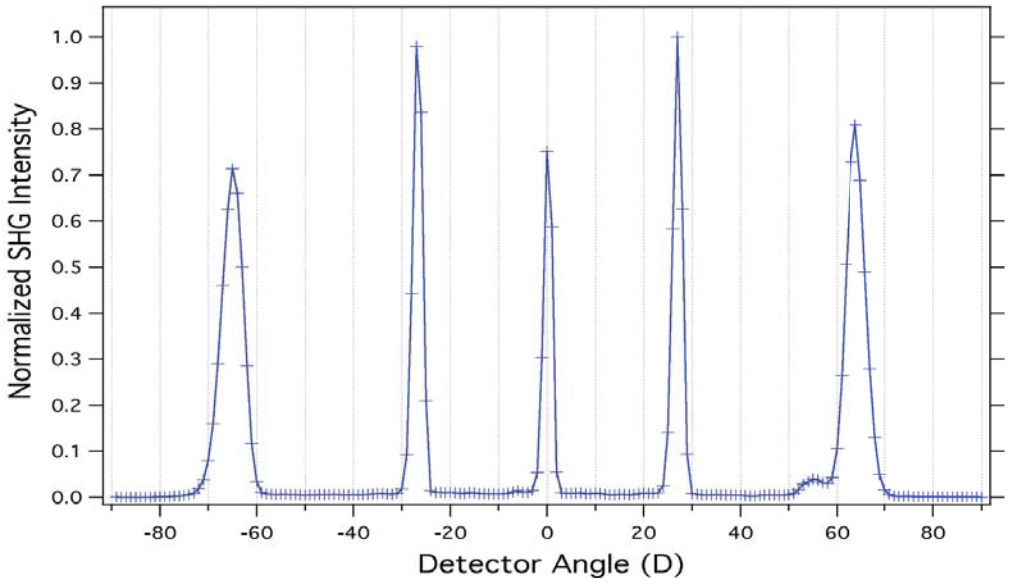

Figure 4.10: The diffraction order distribution of second harmonic generation from a square lattice asymmetric hole array. The sample is at normal incidence. The diffraction orders are: -2, -1, 0, 1 and 2, respectively, from left to right.

calculation, and the theory and the experiment results were again well matched, as shown in Table 4.2 and Figure 4.11.

Another better way to look at this is to look at the whole two-dimensional scan of the same sample. This two-dimension scan shown in Figure 4.12 picks up the diffraction order distribution at all the available incident angles. The contour map on the top of this plot are the calculated diffraction peaks. As a matter of fact, Figure 4.10 and Figure 4.11 are the cross-section view of Figure 4.12 at zero degree and -24 degrees.

Table 4.2: Diffraction peak positions for the second harmonic generation for the same square lattice metallic hole array shown above. The incidence angle for this one is -24 degrees. The lattice constant a_0 was fitted to be $880nm$ even though it has been designed to be $800nm$. The wavelength used here is $800nm$. All calculations are based on equation 4.9. The angles θ and γ are shown in Figure 4.1.

θ=-24	-1	0	1	2	3
Calculated γ	-59.5	-24.0	2.7	30.2	73.1
Measured γ	-59	-24	3	30	73

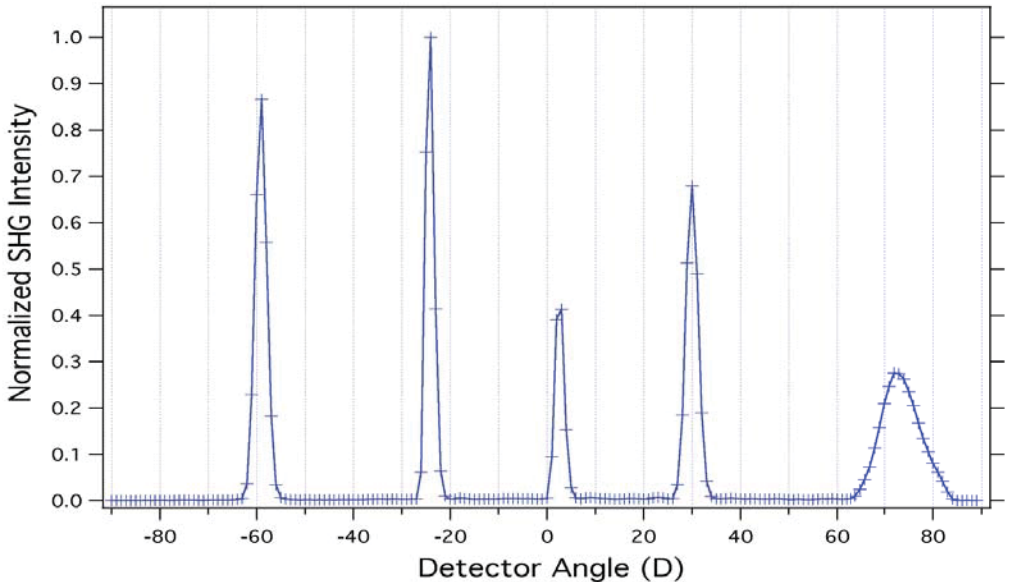

Figure 4.11: The diffraction order distribution of second harmonic generation from the same hole array as used in Figure 4.10. The sample is sitting at -24 degrees. The diffraction orders are: -1, 0, 1, 2 and 3, respectively, from left to right. Compared to Figure 4.10, the positions of the diffraction orders shift as the incident angle changes.

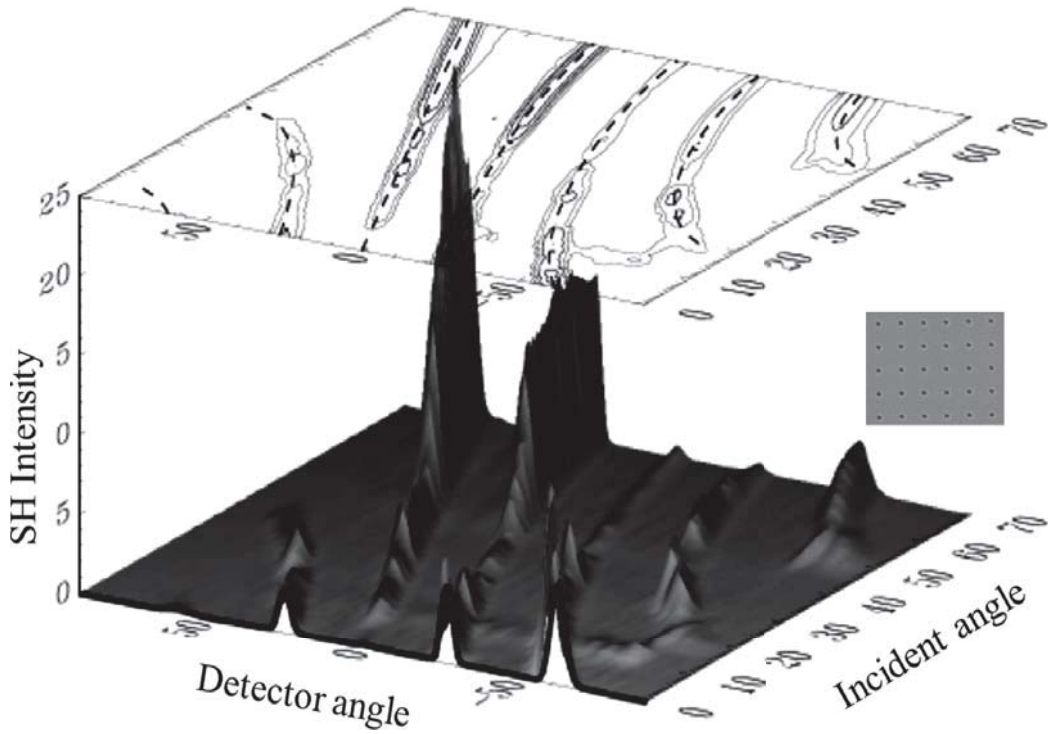

Figure 4.12: Two-dimensional scan of second harmonic generation from a square lattice round hole array (shown in the inset) and the calculated results.

4.6 Second Harmonic Generation from Quasi-Periodic Round Hole Arrays

The Penrose arrangement has five-fold rotational symmetry, and has 10-fold rotational symmetry in the reciprocal space, as plotted in Figure 4.13, with peaks indexed by the transverse spatial frequencies f_x and f_y. Since the reciprocal space is densely packed as compared to that for a square lattice (i.e. there are no primitive vectors), not all peaks are plotted, only those of sufficient magnitude that can be distinctly identified from our measurements.

As a comparison, the same *Fourier* transform had also been performed for a disordered hole array, as shown in the right hand side of Figure 4.13. Unlike the *Penrose* arrangement, which possesses rotational symmetry in the real space, there are no lattice arrangements or symmetry for disordered array. Then in the reciprocal space, there are no other peaks besides the DC.

Figure 4.14 and Figure 4.15 are the transmitted second harmonic generation from a *Penrose* round hole array and a disordered round hole array with same averaged spacings.

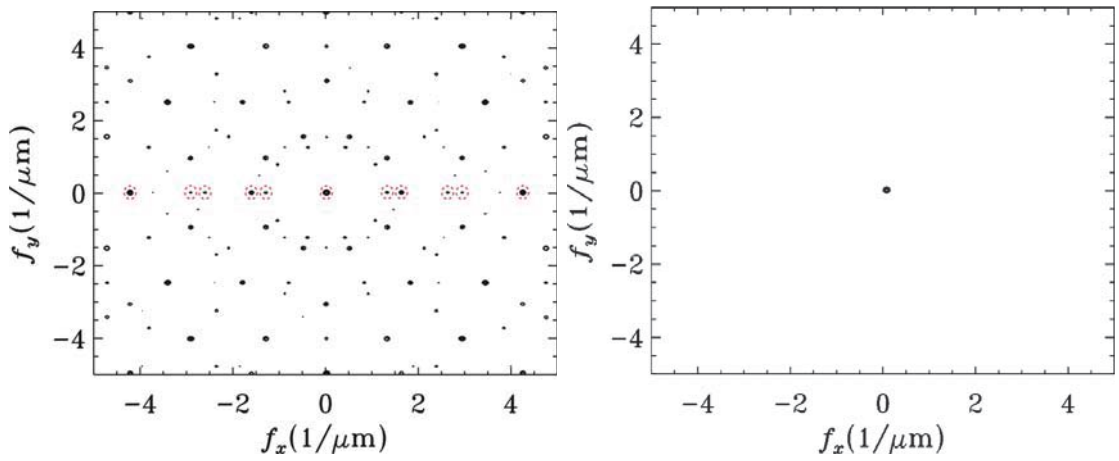

Figure 4.13: The calculated reciprocal space of a *Penrose* (left) and a disordered (right) arrangement. The diameter of each peak is indicative of its magnitude. The red circles represent the spatial frequencies that are used in the fitting of diffraction orders in the experimental plots, which are f_x = 0,1.35,1.65, 2.65, 2.95, and 4.25 $1/\mu m$. For the disordered array, there is only one strong DC shown in the reciprocal space.

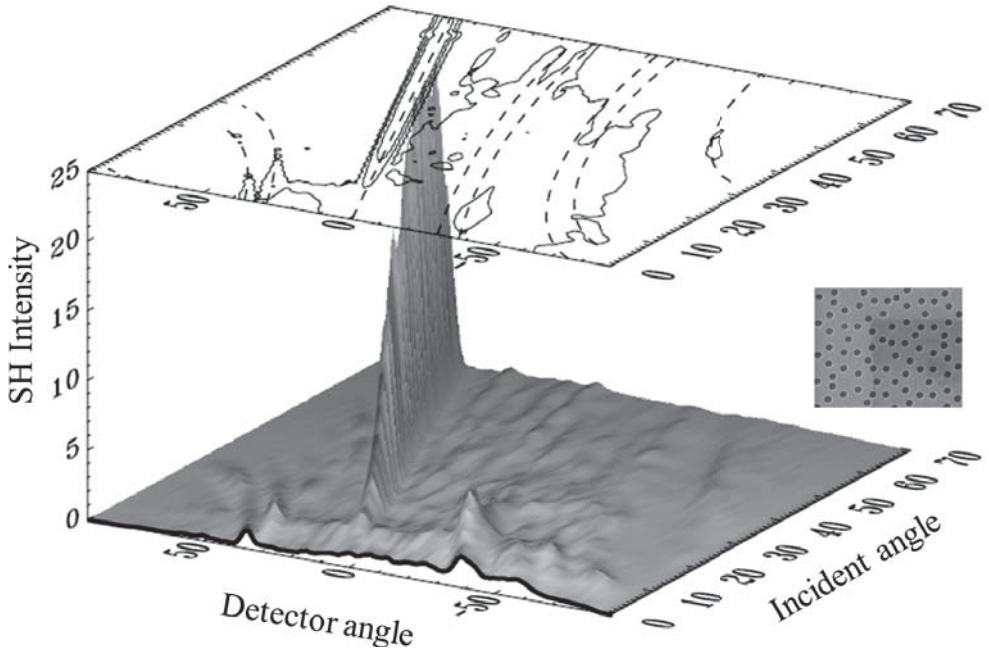

Figure 4.14: A *Penrose* arranged round hole array *SEM* image (inset) and its transmitted two dimensional second harmonic generation scan. Most of the diffracted energy has been distributed to the normal detection and the background is getting less distinctive than the square lattice array because of the reduced symmetry.

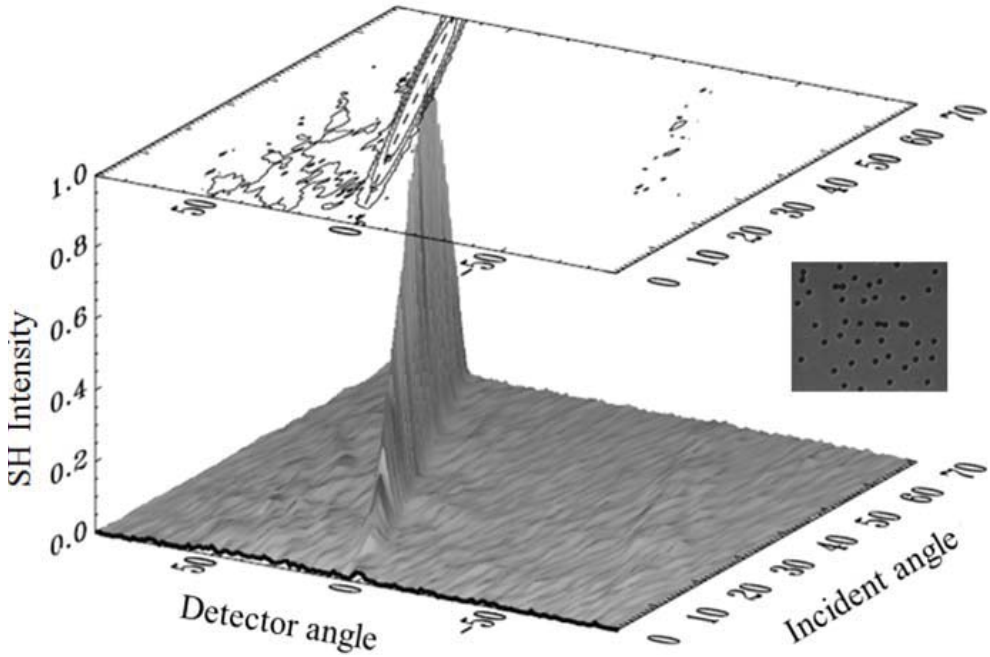

Figure 4.15: A disordered round hole array *SEM* image (inset) and its transmitted two-dimensional second harmonic generation signal. Since the array is highly disordered, there is no symmetry for the array at all. So as a whole, the array can not distribute any energy to any off-axis directions.

From square lattice to *Penrose* structure to disordered arrangement, the degree of symmetry of the lattices is decreasing, so the peaks of the fundamental and second harmonic generation are getting much less distinctive. With disordered array, there is no peak at all because the holes are distributed randomly, and there is no symmetry for the array either.

4.7 Mathematical Model for Absence of Peaks at Normal Incidence

For many of the second harmonic measurements we have seen so far, there is no peak at normal incidence for all kinds of lattice arrangements. There is a simple mathematic model which is capable of providing an explanation. Looking at the intensity distribution inside the aperture shown in Figure 4.2, it is reasonable to approximate the second harmonic generation from each aperture as two point sources on the opposing sides of the aperture and aligned along the polarization direction of the incident light. Inversion symmetry demands that these two point sources be out of phase. Mathematically, the array of second harmonic generation source terms can be expressed by:

$$\left[comb\left(\frac{x+d/2}{\Lambda}\right) - comb\left(\frac{x-d/2}{\Lambda}\right)\right] comb\left(\frac{\lambda}{\Lambda}\right) \tag{4.10}$$

in real space, where d is the aperture diameter and Λ is the lattice spacing. By taking the 2-D Fourier transform (with f_x and f_y the transverse spatial frequencies), the second harmonic generation can be expressed in angular space as:

$$comb(f_x\Lambda)sin(\pi f_x d)comb(f_x\Lambda) \tag{4.11}$$

Because of the *sin* factor in equation 4.11, the second harmonic generation diffraction pattern has no zeroth order (i.e. where $f_x = 0$). Furthermore, opposing diffraction orders must be out of phase with respect to each other, meaning that if detected symmetrically, they would interfere destructively and cancel. This is the case for the measurements done with the detector parked alongside with the incident light. But if the detector is not detecting symmetrically, as in the case γ not equal to zero, the diffracted second harmonic generation signal should be able to be detected. This is true as shown in the following two-dimensional scans.

The expression in equation 4.11 also predicts that for higher diffraction orders, the intensity follows $sin^2(\pi f_x d)$, which has been shown for SH from arrays of symmetric particles.[79]

4.8 Second Harmonic Generation from Asymmetric Hole Arrays

Another way to break symmetry is to change the symmetry of the aperture itself. The aperture was designed to be a three-armed star-like structure, with angles between adjacent arms to be 90^o, 120^o and 150^o. So there is no rotational symmetry for the aperture itself. In this case, the inversion symmetry of the aperture has been broken so as to introduce asymmetry in the local field distribution.[80] [81] [82]

The same $FDTD$ calculation was carried out and the intensity distributions inside the aperture under normal incidence are shown in Figure 4.16.

It is apparent that the intensity distribution is more complex than that of the round aperture, with E_x and E_y components reaching roughly the same magnitudes. Even though the magnitudes of both E_x and E_y are less than that obtained for E_x with the round aperture, none of them could be canceled at normal incidence, which provides the possibility of a nonzero $\chi^{(2)}$.

The break of the aperture symmetry is exhibited from the second harmonic generation signal shown in Figure 4.17 and Figure 4.18 at normal incidence. They are not zero or minimum any more because of the local symmetry breaking of the apertures themselves.

4.9 Conclusions and Discussions

With all the samples we fabricated, we have generated second harmonic signals from each one of them successfully.

Generally, the extraordinary optical transmission follows the prediction of surface plasmon theory. The second harmonic is generated from the apertures and peaks under the condition of localization of incident light at the fundamental frequency at the incidence angles corresponding to enhanced transmission. Therefore, on the transmission angular spectrum, the second harmonic generations are strongly angular dependent and follow the trend of the fundamental transmission.

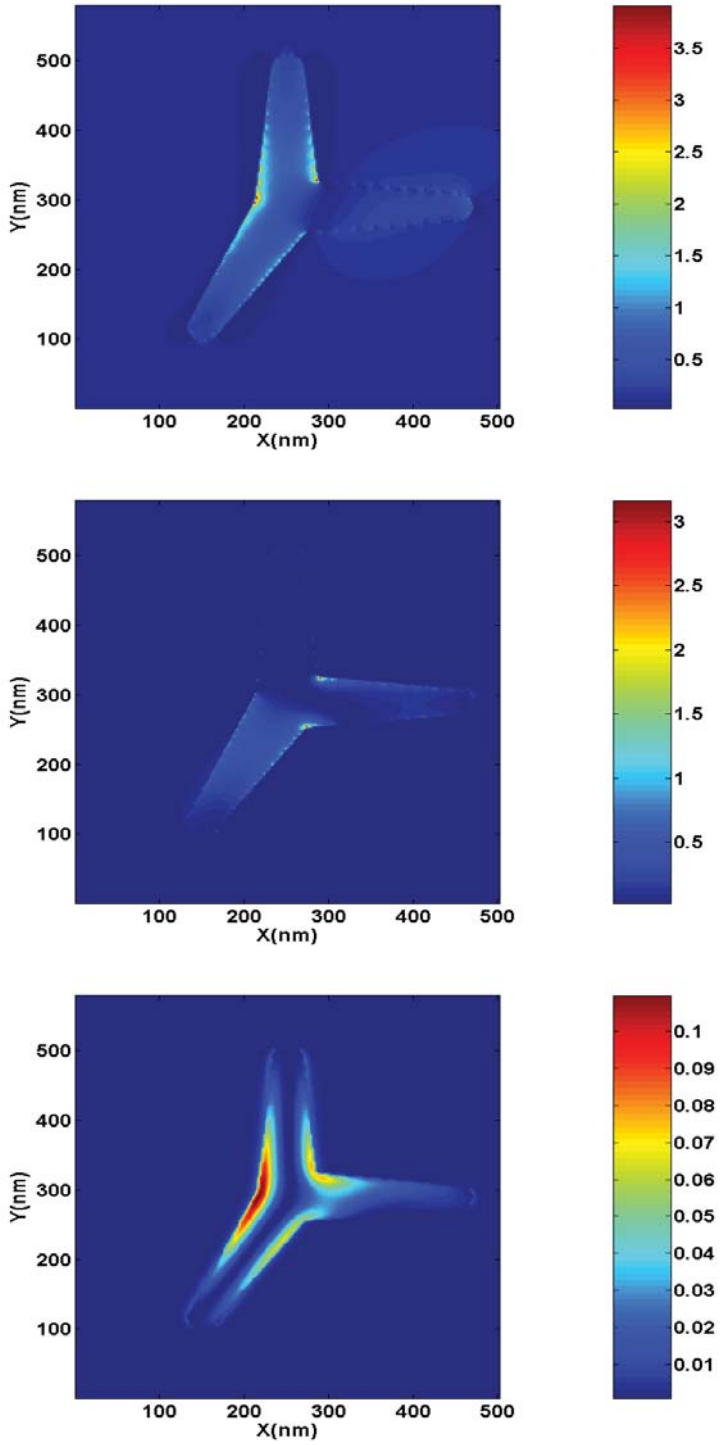

Figure 4.16: (Reprinted with permission from Xiaojin Jiao) Top view of feld distribution inside asymmetric apertures at normal incidence. From top down, they are $|E_x|^2$, $|E_y|^2$ and $|E_z|^2$ respectively.

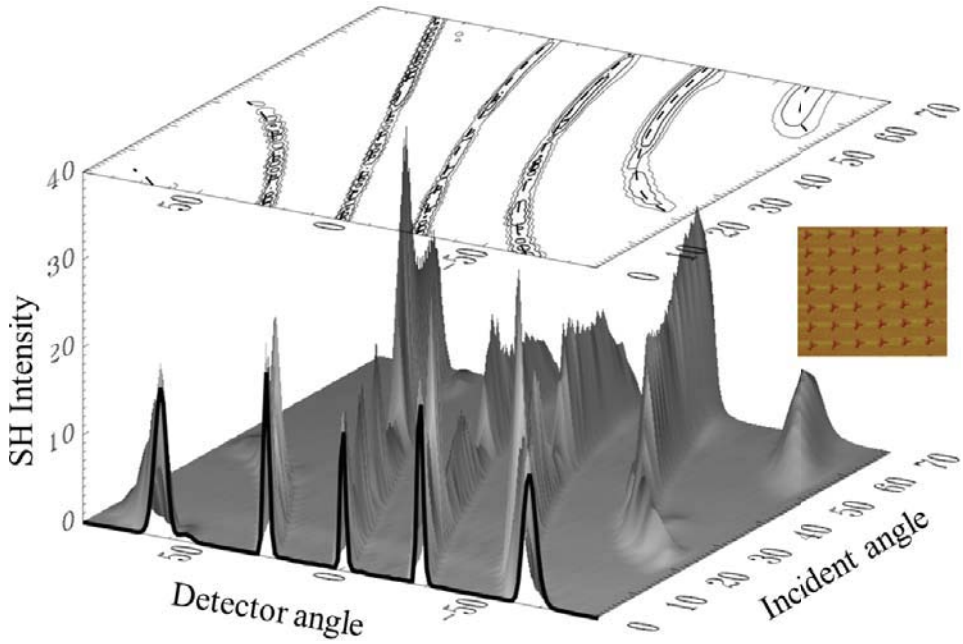

Figure 4.17: An AFM image of a square lattice asymmetric hole array (inset) and the double angle scan for the transmitted second harmonic signal. A second harmonic generation peak clearly shows up at the normal incidence, and the energies have been distributed to well-defined positions because of the highly ordered square lattice arrangement.

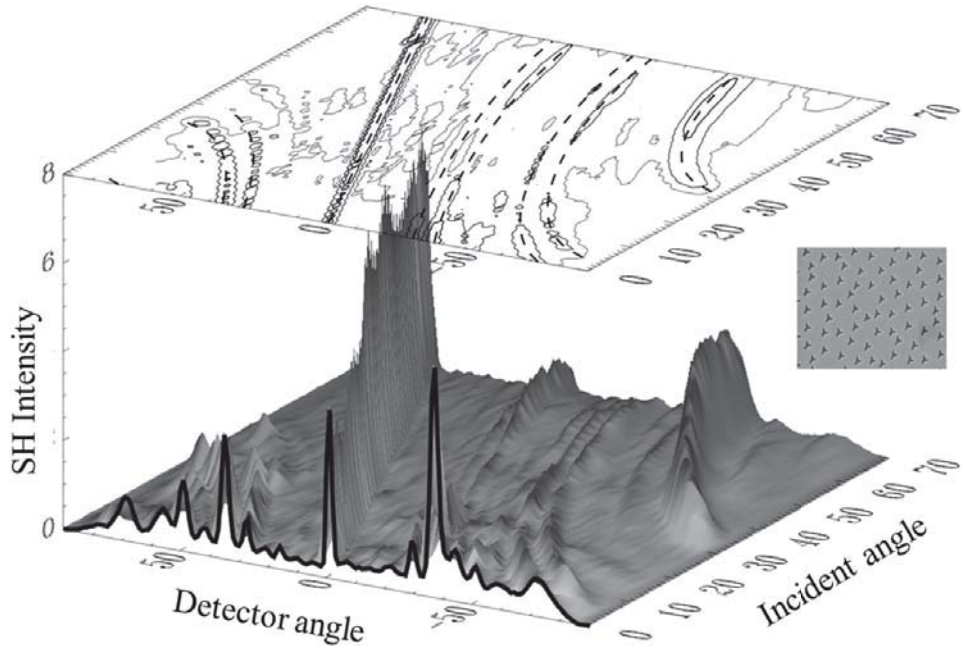

Figure 4.18: A Penrose lattice asymmetric hole array *SEM* image (inset) and the double angle scan for the transmitted second harmonic signal. Even though the second harmonic generation signal at normal incidence is clearly seen, the off-normal signals are much weaker due to the reduced symmetry.

Symmetry played the most important role in the generation of second harmonic signal.

1. Very different behavior in the second harmonic emission pattern is observed as a function of lattice arrangement. The disordered arrangement cannot produce off-axis SH peaks because of the lack of any short-range or long-range periodicity that would allow for coherent addition of local sources in directions off that of the fundamental. The Penrose arrangement is quasi-periodic, allowing this coherent addition to occur, but with weaker diffraction efficiency than obtained for a periodic lattice.

2. The symmetry can be broken with off-axis illumination and off-axis detection. Our calculations and experiments suggest that upon off-axis illumination, second harmonic generation from the two point source of the aperture can not be canceled out, so there are peaks at off-axis incidence but not at normal incidence.

3. The symmetry can also be broken by breaking the symmetry of the aperture itself. Because of the lack of symmetry of the aperture, the local field distribution at normal incidence is no longer symmetric as that of the symmetric apertures. Then a distinctive peak at normal incidence shows up.

CHAPTER 5

THIRD HARMONIC GENERATION FROM SUBWAVELENGTH METALLIC HOLE ARRAYS

Compared to second harmonic generation, which is prohibited in many cases because of symmetry, the constraints of third harmonic generation are much looser, and essentially, it is always allowed. On the other hand, the nonlinear susceptibility responsible for third harmonic generation is orders of magnitude smaller than the second order susceptibility,[4] but to increase the laser power by orders of magnitude is not trivial, so the overall result is that it is not easy to generate higher order harmonics and that is why field enhancement is so important.

In this chapter, we report results on third harmonic generation from subwavelength metallic hole arrays. We have used the mode locked output from the oscillator and high energy output of a Ti:Sapphire regenerative amplifier as the incident light. In both cases, we have successfully generated third harmonic signals with very similar results.

5.1 Third Order Nonlinearity

With the third order $\chi^{(3)}$ nonlinear susceptibility, the generic process is four wave mixing $\chi^{(3)}_{lmno}(\omega_i;\omega_j,\omega_k,\omega_l)$. Of particular interest is the degenerate case, where $\omega_1 = \omega_2 = \omega_3 = \omega$, resulting in third harmonic generation.

Third harmonic generation in the limit of negligible pump depletion is similar as that for second harmonic generation with $P^{(2)}(2\omega)$ replaced by $P^{(3)}(3\omega) = \chi^{(3)}(3\omega = (\omega+\omega+\omega) : E(\omega)E(\omega)E(\omega)$. Since $\chi^{(3)}$ is usually small, and the laser intensity is often limited by optical damage in the medium, the conversion efficiency for third harmonic generation is very low.

One of the most efficient ways of generating a third harmonic is to have two nonlinear media in series and making use of phase matched $\chi^{(2)}$. The first medium generates a second harmonic beam. The transmitted fundamental beam and the second harmonic output beam are then combined in the second medium to yield a third harmonic output by sum frequency generation. With a sufficiently intense fundamental beam, the overall efficiency of THG can be fairly high.[1]

5.2 Some Experimental Considerations

Since the third harmonic wavelength at $266nm$ is in the ultraviolet regime, and can be strongly absorbed by many materials, care needs to be taken to collect and detect the generated signal.

First of all, the substrate must be transparent to UV light. Fortunately, all of our samples use quartz as a substrate, so the generated third harmonic can easily pass through a relatively thick quartz slab of about 1 mm without losing too much power according to the transmission curve provided by the vendor shown in Figure 5.1.

Another very important aspect is the right detector. The $H5784-03$ PMT provides very good optical response at $266nm$ and has almost no response to the

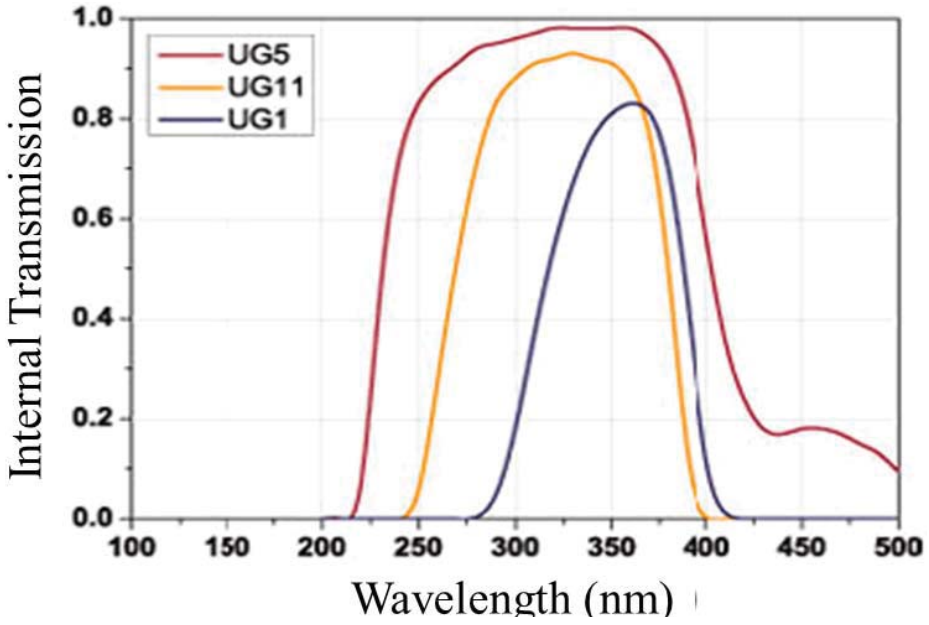

Figure 5.1: The specifications for the glass filter used for third harmonic generation measurements. The glass filters are made from $UG5$ from $ThorLabs$.

fundamental wavelength at $800nm$, as shown in Figure 5.2. Combined with properly chosen spectral filters, it works very well to detect the generated third harmonic signals.

There are two spectral filters used to detect the third harmonic signal from the metallic hole arrays. After passing through the collecting lens, the generated signal is filtered by a color glass filter $UG5$ from $ThorLabs$, which has a pass band around $220nm$ to $400nm$. The transmitted signal is then further selected by an interference bandpass filter with $20nm$ passband centered at $265nm$.

There are also restrictions for the optics used to collect the signals, and one of the most important is the collecting lens right after the sample. When taking second harmonic generation measurements, since the wavelength at $400nm$ is longer than $266nm$, we do not have any difficulty of collecting second harmonic signal with regular achromatic doublets as the focusing lens. But when we first try to measure third harmonic generation with the same achromatic collecting lens, there is no response from the PMT at all. The achromatic doublet is too thick to let any short wavelength

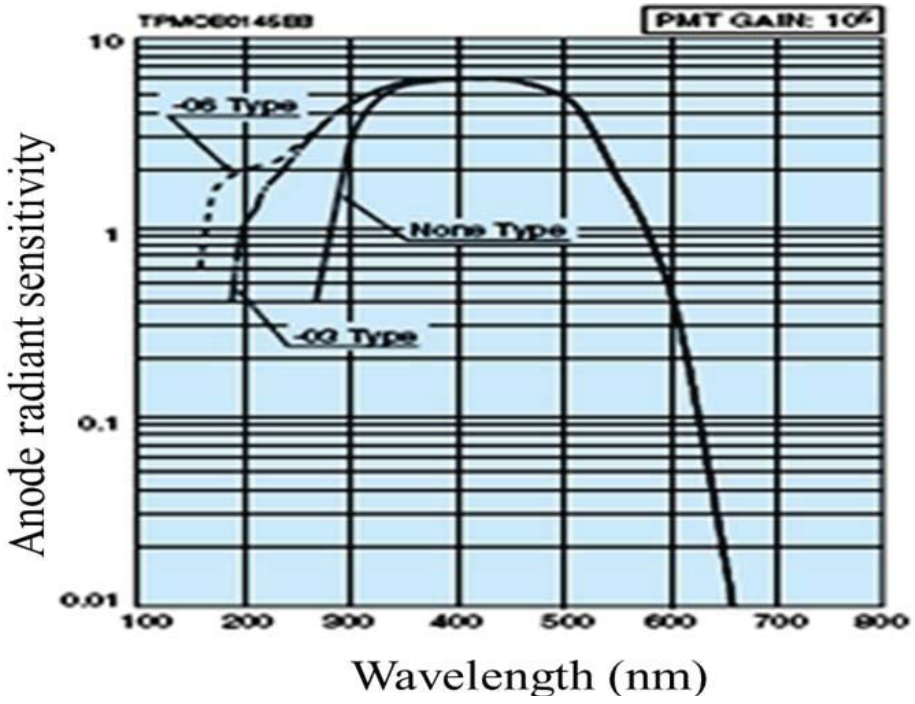

Figure 5.2: The specifications for the detector used for third harmonic generation measurements. The detector is from $Hamamatsu$ with part number H5784-03.

light to pass through. As soon as we switched to a focusing lens made from fused silica, we obtained very strong third harmonic signal.

We also used the output light from a Ti:Sapphire regenerative amplifier as the light source, and a boxcar averager system was used to collect data. The schematics shown in Figure 5.3 show the setup we have used for the third harmonic generation measurements.

5.3 Third Harmonic Generation from Square Lattice Hole Arrays

Just like second harmonic generation, we believe that the surface plasmon enhancement plays an important role in third harmonic generation. When surface plasmon modes are excited, the electric field inside the holes is strongly enhanced, leading to the extraordinary optical transmission. The enhanced fundamental transmission also generates transmission peaks of the third harmonic signal, since its intensity is proportional to the third power of the intensity of the fundamental intensity.

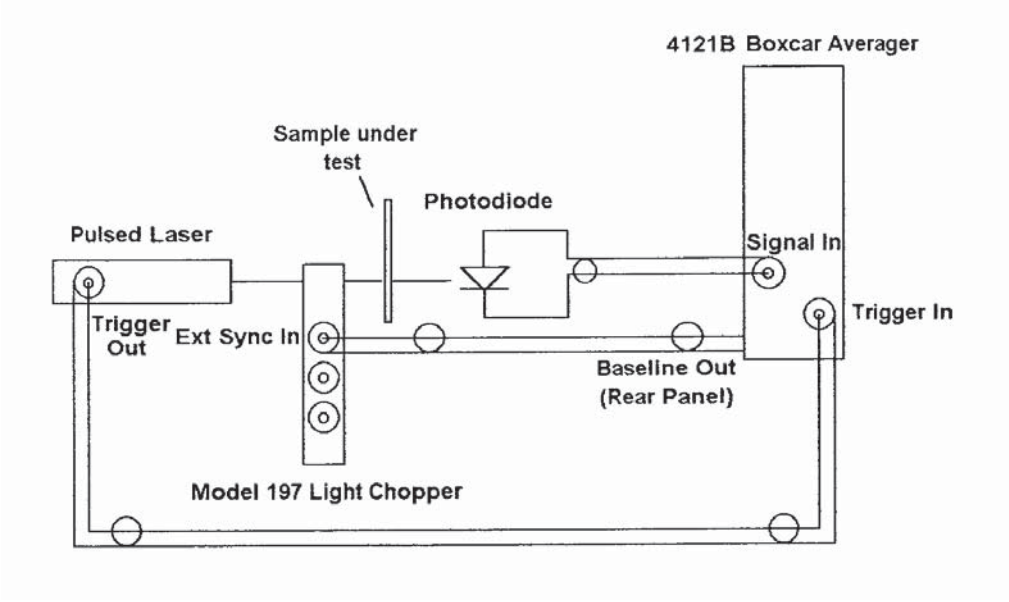

Figure 5.3: The boxcar averager system used to measure the generated third harmonic from the metallic hole arrays. A single channel is used with baseline subtracted, presumably giving cleaner results. Instead of using the chopper specified in this diagram, we have used a regular mechanical chopper modulated by the output from the boxcar and running at half the frequency of the boxcar, $500Hz$, allowing continuous baseline subtraction.

According to theory, the fundamental beam couples to the surface plasmon polariton waves under the following condition,

$$sin\theta = -i\left(\frac{\lambda_0}{a_0}\right) \pm \sqrt{-\left(\frac{j\lambda_0}{a_0}\right)^2 + \frac{\epsilon_d \epsilon_m}{\epsilon_d + \epsilon_m}} \tag{5.1}$$

where i, j are mode numbers and λ_0 is the wavelength of the incident light which is $800nm$ in our work. So accordingly, the transmitted third harmonic generation should have very similar angular distribution.

As a comparison, both second and third harmonic generation from a same hole array are shown in Figure 5.4. It is clear from this plot that:

1. As we have discussed for second harmonic generation, the third harmonic signal follows the transmitted fundamental signal trend better than second harmonic generation.

2. Unlike second harmonic generation, third harmonic generation is allowed at normal incidence.

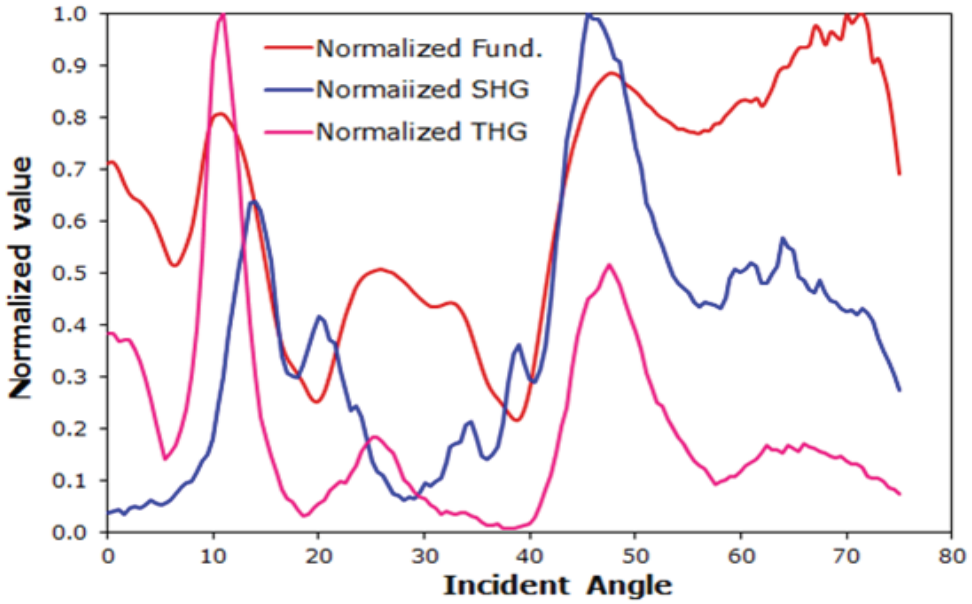

Figure 5.4: SHG and THG normalized signal from a square lattice round hole array and the corresponding fundamental transmission from the same hole array. The holes are fabricated on $100nm$ Au film with a $5nm$ Cr adhesion layer. The holes are about $250nm$ in diameter and arranged in a square lattice with about $910nm$ spacing.

3. Another difference between second harmonic generation and third harmonic generation is that the third harmonic peaks at exactly the same sample angle, but almost all the second harmonic generation angles are slightly off the fundamental peaks.

4. In theory, SHG intensity should be proportional to the square of transmitted fundamental power, and THG to the cubic of transmitted fundamental power. If we plot the normalized transmitted power, the square of normalized transmitted power and normalized SHG intensity together, as shown on the top plot in Figure 5.5, the curves did not match very well, especially at lower angles.

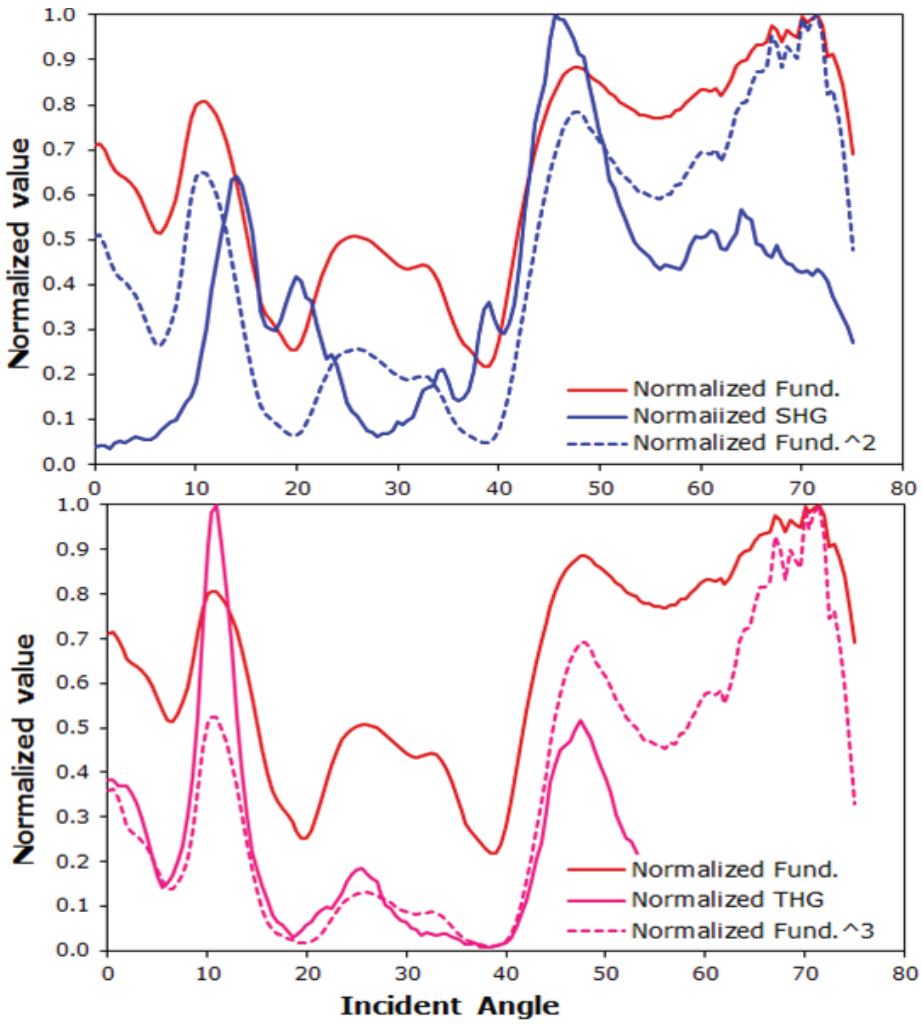

Figure 5.5: Comparison of normalized fundamental transmission, its second order power and third order power, second harmonic generation and third harmonic generation from a square lattice round hole array.

However, if we plot the normalized transmitted power, the cubic of normalized transmitted power and normalized third harmonic generation intensity together, as shown on the bottom plot in Figure 5.5, the curves matched much better. This also indicates that the symmetry did not play as important a role for third harmonic generation as that of the second harmonic generation.

Figure 5.6 shows the comparison of third harmonic generation measurements with the boxcar averager system and the lock-in system. We found very similar results from the lock-in amplifier with an oscillator as the light source. As a matter of fact, all the experimental setup is the same, except that the light source and the ADC or the signal averaging part are different.

5.4 Verification of Third Harmonic Generation

The same questions arise as in the second harmonic generation: are these signals really third harmonic generated from the incident light? The simplest way to find out the answer is to use a spectrometer to measure the wavelength of the output

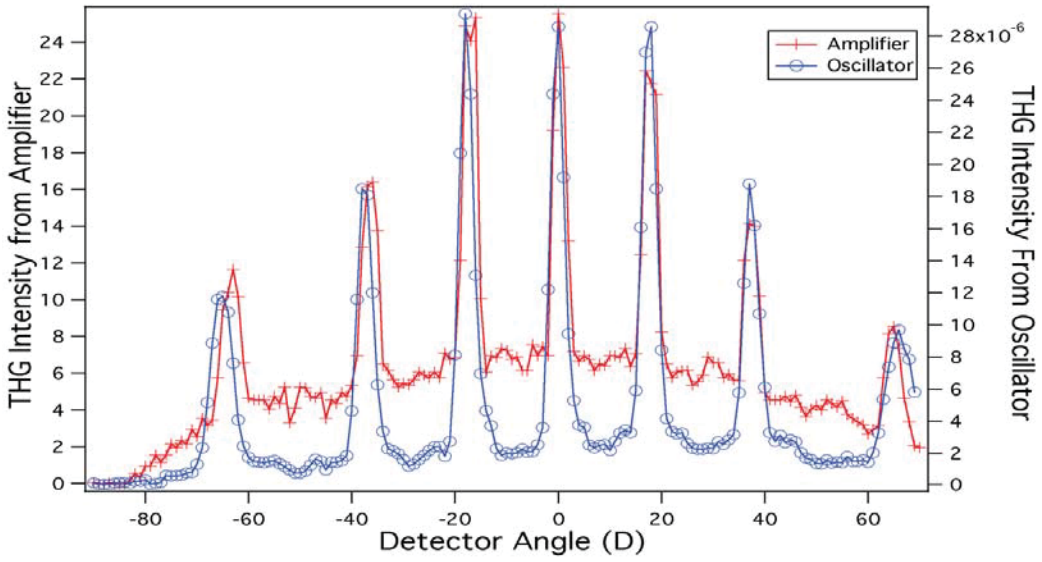

Figure 5.6: Comparison of the detector scan for measurements taken from a regular Ti:Sapphire oscillator and a regenerative amplifier. The samples are fabricated at the same time and went through the same processes, but the sample for the amplifier has $220nm$ of SiO_2 on top. The samples were sitting at zero degrees so the incidences were at normal. In the case of the oscillator, the average power was about $40mW$, and about $0.3mW$ when the amplifier was used.

from the hole arrays, but it is not practical because of the extremely low conversion efficiency. There is also another ambiguity for third harmonic generation: unlike second harmonic generation, it is not forbidden for any medium, so any material exposed on the incident light might will contribute to the output signal, like signals from metal film itself, or even the signals from the quartz substrate.

Similar to what we did to identify second harmonic generation, we also use power dependence, angular dependence and diffraction patterns to distinguish the different sources of the third harmonic generation.

5.4.1 Power Dependence

Just like second harmonic generation, power dependence is the first thought when it comes to verify that the generated signals are really third harmonic. Figure 5.7 shows the power dependence of the generated third harmonic signal. The measurements were taken with bare quartz and pure *Au* film sitting at normal incidence, and from a hole array at 45 degrees to maximize the signal. All the curves show a cubic power dependence, which at least suggests that the measured signals are from third harmonic generation.

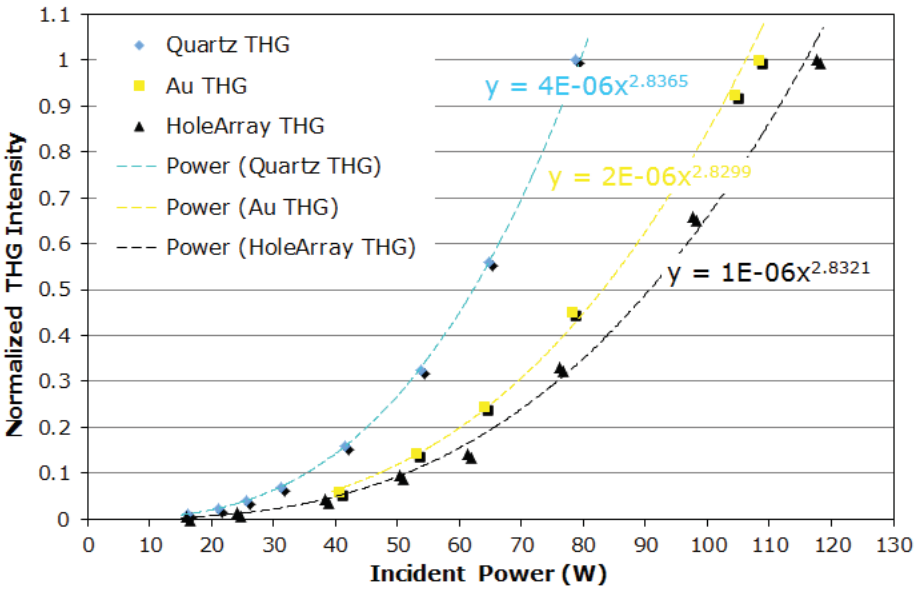

Figure 5.7: Power dependence of the third harmonic signal from bare quartz, pure *Au* film and a square lattice round hole array. The corresponding fitting curves show a power dependence very close to 3.

5.4.2 Angular Dependence

Power dependence of the output alone can only prove the measured signals are resulting from a three-photon process, but do not answer the questions of whether the signal is from the hole array or from the pure metal film, or even from the substrate. Angular dependence can provide further evidence to distinguish the source of the signal. If the signal is from the quartz substrate, there will not be any difference between the sample at normal incidence and the sample at an oblique angle, except that the optical path will be slightly longer. If the signal is from the metal film, the signal will be very weak.

Figure 5.8 shows the third harmonic signals from a piece of quartz slide and a $100nm$ Au film. The third harmonic signal from quartz decreases when the sample is turned away from normal incidence. In the case of pure Au film, the variation of the third harmonic generation signal level is much smaller because the Au film is primarily reflecting. The sudden drop at 50 degrees is probably caused by Fresnel

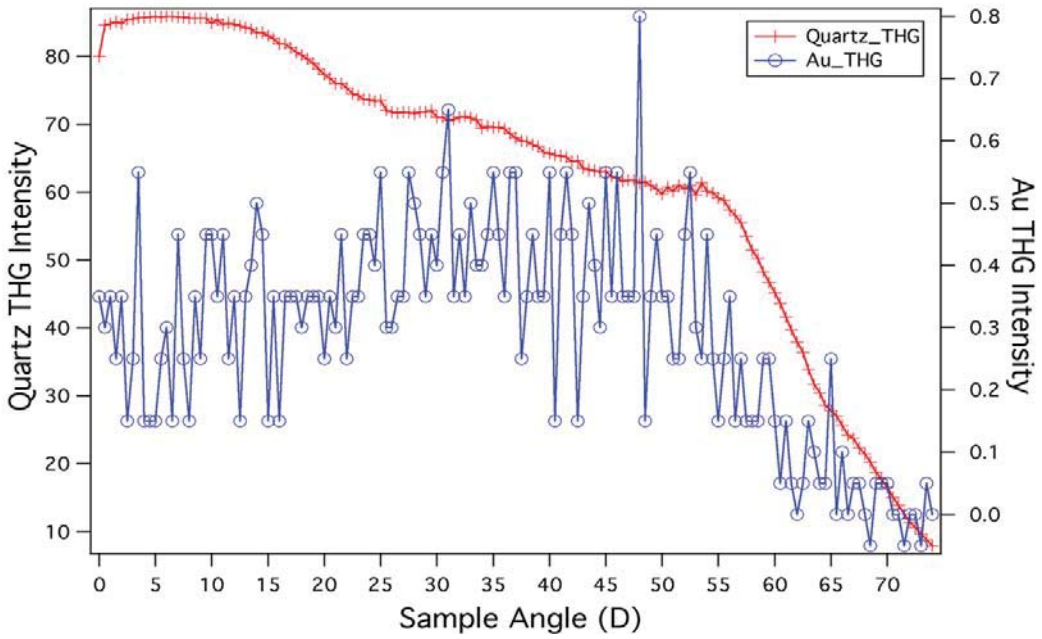

Figure 5.8: The angular distribution of third harmonic generation from quartz substrate (left) and $100nm$ gold film (right). The maxima appear at normal incidence and there are no other third harmonic generation peaks. The measurements were performed with output from a regenerative Ti:Sapphire amplifier with an average power of about $0.3mW$.

reflection from the quartz substrate and this matches very well the sudden drop from that of quartz.

Comparing Figure 5.4 and Figure 5.8, it is very clear that there is negligible contribution to third harmonic generation from the quartz substrate and gold film. In contrast, the angular dependence of the hole array is dominant.

5.4.3 Diffraction Pattern at Third Harmonic Generation Wavelength

There is still one question remaining: is the three photon process third harmonic generation? To answer this, we can look at the diffraction pattern at the output, which can only be produced by a coherent process. For a square lattice hole array with lattice constant Λ, after coupling out from the holes, there are diffraction orders on the back of the sample, described by the following equation,

$$sin\gamma = sin\theta + m\frac{\lambda}{3\Lambda} \tag{5.2}$$

where λ is the fundamental wavelength, and m is the diffraction order, which can have the values of 0, ± 1, ± 2, $\cdots$

According to equation 5.2, the third harmonic diffraction peaks for a square lattice hole array will appear at the positions shown in Table 5.1. The calculated peak positions for all the diffraction orders match the measurements very well, as shown in Figure 5.9 for the diffraction scan of a square lattice of round holes at normal incidence.

We have also performed the same calculation for the same sample at different incident angles in order to exclude any coincidence for certain situations which only

Table 5.1: Diffraction peak positions for the third harmonic generation from a square latticed metallic hole array. The sample was sitting at zero degrees, so θ is 0. The lattice constant a_0 was fitted to be $880nm$ even though it has been designed to be $800nm$. The wavelength used here is $800nm$. All calculations are based on equation 5.2. The angles θ and γ are shown in Figure 4.1.

Diffraction Order m	-3	-2	-1	0	1	2	3
Calculated γ	-67.7	-38.1	-18.0	0	18.0	38.1	67.7
Measured γ	-68	-38	-18	0	18	38	68

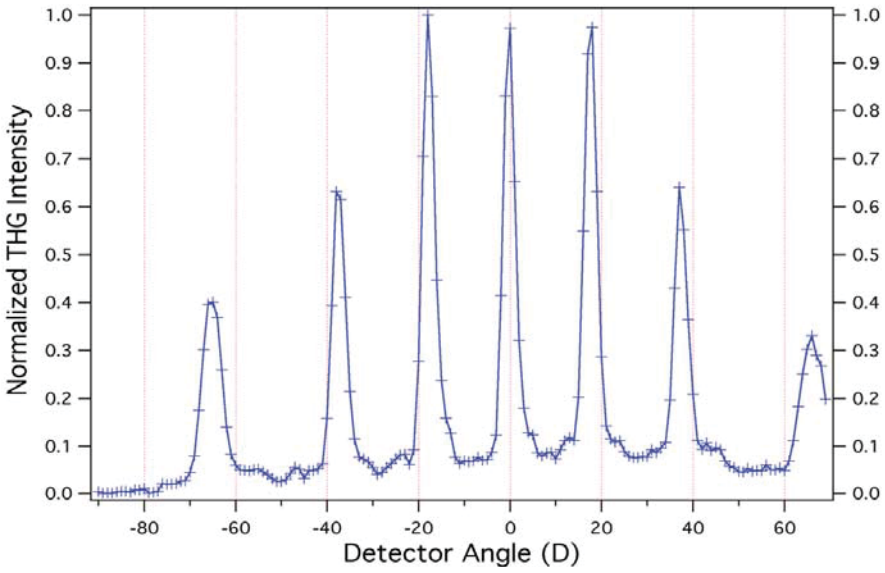

Figure 5.9: The diffracted third harmonic generation signal from the square lattice round hole array. The incidence was at normal incidence. The diffraction orders for the third harmonic generation shown here are: -3, -2, -1, 0, 1, 2, 3 respectively from left to right. The holes are fabricated on $100nm$ Au film with $5nm$ Cr adhesion layer. The holes are about $250nm$ in diameter and arranged in square lattice with about $880nm$ spacing.

apply to normal incidence. We have picked another peak position at -48 degrees and the results are shown in Table 5.2 and Figure 5.10.

On the other hand, if we scan the detector with pure quartz or bare Au film sitting at normal incidence, which is the position for them to have the largest third harmonic signal, we did not see any diffraction orders (except the 0th order or the direct transmission) at the third harmonic wavelength ($266nm$ for $800nm$ incidence laser), as shown in Figure 5.11.

Table 5.2: Diffraction peak positions for the third harmonic generation from a square latticed metallic hole array. The sample was sitting at $\theta = -48$ degrees. The lattice constant a_0 was fitted to be $880nm$ even though it has been designed to be $800nm$. The wavelength used here is $800nm$. All calculations are based on equation 5.2. The angles θ and γ are shown in Figure 4.1.

Diffraction Order m	0	1	2	3	4	5
Calculated γ	-48	-26.1	-7.9	9.6	28.0	50.5
Measured γ	-48	-26	-8	9	28	50

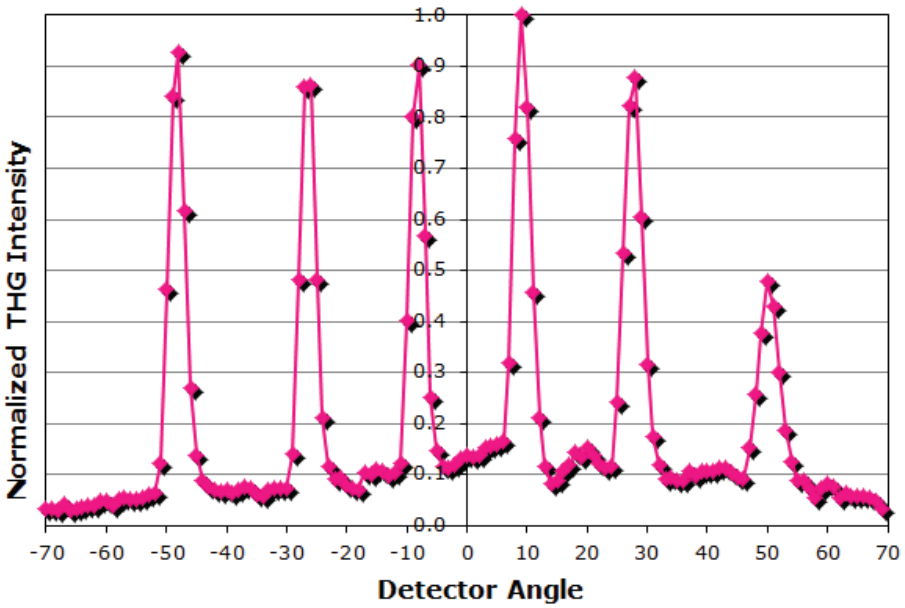

Figure 5.10: The diffracted third harmonic signal from a square lattice of round holes with sample sitting at -48 ($\gamma = -48^o$). The diffraction order for the third harmonic generation shown here is: 0, 1, 2, 3, 4, 5, respectively, from left to right. Because the sample is shifted in one side, the diffraction orders on one side did not exist, and more diffraction orders on the other side appear.

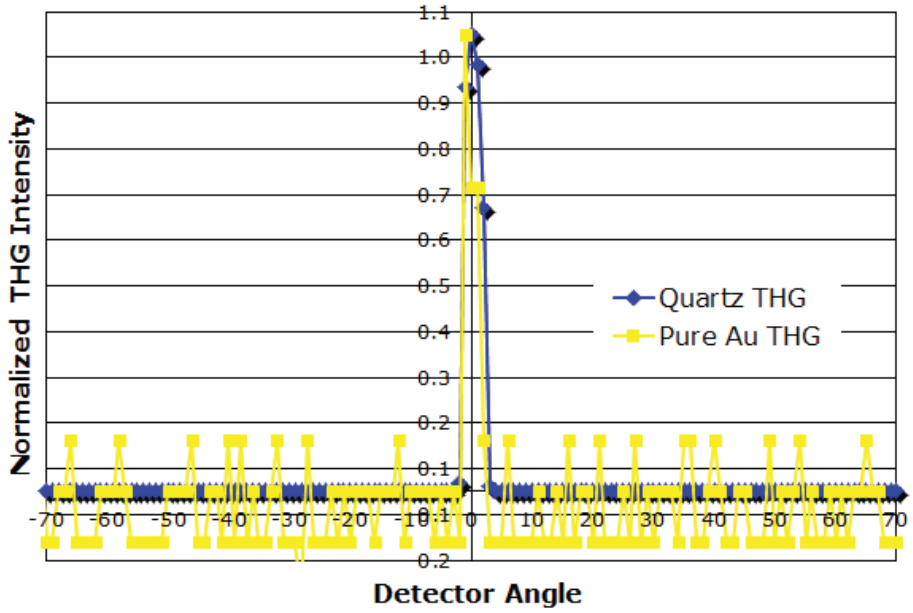

Figure 5.11: Detector scan for the quartz substrate and $100nm$ gold films. There is only one peak when the detector is aligned with the incident light and it is clear that there are no diffraction peaks. The measurements were performed with output from a regenerative Ti:Sapphire amplifier with an average power of about $0.3mW$.

From Figure 5.8, 5.9 and 5.11, we are very confident that the measured third harmonic signals are really generated from the metallic hole arrays, not from the substrate, nor from pure gold film.

The diffraction pattern can be more clearly seen by the two-dimensional scan, as shown in Figure 5.12, for the third harmonic generation from a square lattice asymmetric hole array. The third harmonic generation signals are shown at the angles predicated by equation 5.1 and equation 5.2.

On the other hand, as shown in the same Figure 5.12, the third harmonic generation from a hole array of the same unit aperture, but with disordered arrangement, has no clear third harmonic generation diffraction pattern, except along the line where the detector angle aligned with the incidence angle.

After independent verification from the three different methods, we are now confident that the output signals are really third harmonic generation, and they are generated from the hole arrays, not from the quartz substrate or the gold film. The contributions of the substrate and pure gold film only provide a constant and decreasing background for our measurements. We can also see that the quartz substrate contributes more to the third harmonic generation than gold film, but when we focus the laser on the hole arrays, this effect has been minimized. This also proves that we engaged with the hole arrays very well during the whole measurement processes.

5.5 Conclusions and Discussions

We have successfully measured third harmonic generation signals from subwavelength metallic hole arrays.

The generated third harmonic generation signals also have very strong angular dependence, and the third harmonic generation transmission peaks follow the transmission peaks of the fundamental wavelength, which indicates that third harmonic is generated upon intensity buildup inside the apertures.

The third harmonic generation diffraction orders are more compactly positioned comparing to those of the second harmonic generation when scanning the detector,

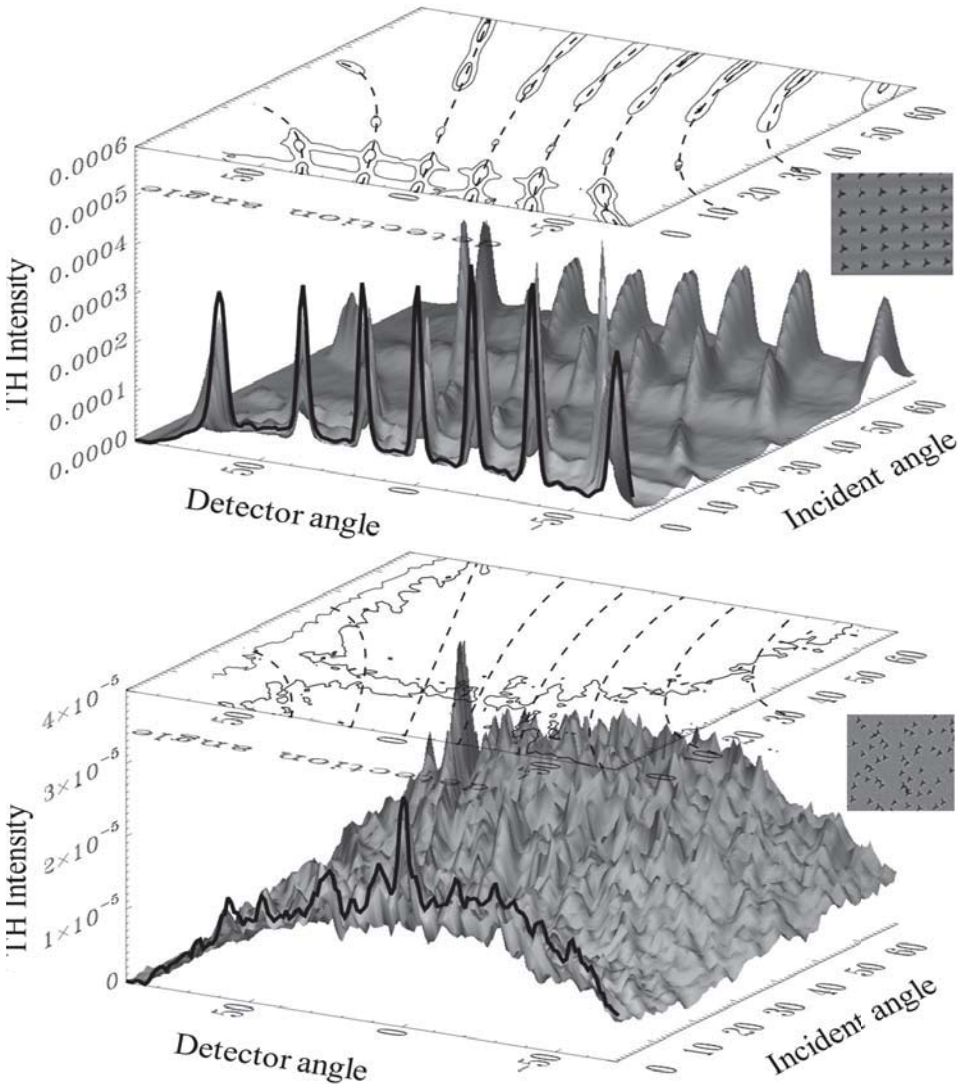

Figure 5.12: Third harmonic generation from asymmetric hole arrays. The top plot shows the AFM image of a square lattice arranged asymmetric hole array and the well-defined third harmonic generation signal. The bottom plot shows the SEM image of a disordered asymmetric hole array and the third harmonic signal detected from it. Even though both hole arrays have the same unit apertures, the third harmonic generation diffraction patterns are totally different.

and this also validated that the wavelength we have been working at is really at the third harmonic wavelength, which is shorter than the second harmonic wavelength.

Similar to second harmonic generation, lattice arrangement also has strong impact on the transmitted third harmonic generation. Unique to the third harmonic generation, there is always a strong signal at the normal incidence because of the lacking of symmetry constraints.

CHAPTER 6

SHG AND THG INFLUENCING FACTORS: ADHESION LAYER, LATTICE PERIOD, FILLING MATERIALS AND APERTURE SHAPE

Harmonic generation is very sensitive to minor variations of the samples if we keep the incident laser constant. In this chapter, we have studied factors which might affect the generation of harmonics, like the adhesion layer, period of lattice, aperture shapes, and filling materials in the holes.

6.1 Effects of Adhesion Layer

A practical issue not always addressed for plasmonic structures is the adhesion layer. Oftentimes, a thin layer of Cr is used to promote the adhesion of Au to a glass substrate. However, Cr is a highly lossy material, and can cause significant attenuation of surface plasmon polariton propagation at the metal substrate interface. In order to study the effects of adhesion layers, we have used Cr and TiO_2 with different thicknesses as adhesion layers. We have followed exactly the same nanohole array fabrication process for those types of samples.

The method of sputtering the Cr adhesion layer has been described before. To sputter the TiO_2 adhesion layer, we have used reactive sputtering by introducing O_2 to the sputtering process. We have kept the flow rate of Ar and O_2 gases at the ratio of $1:1$ during sputtering. After this, we have let the pure O_2 gas flow through the chamber for about 10 minutes in order to fully oxidize the Ti layer. Then without opening the chamber, $100nm$ gold film and the top $20nm$ Cr cover layer were sputtered. Since the TiO_2 layer is only less than $10nm$, it should have

been etched through by the Ar ion milling. Also one advantage of using TiO_2 as the adhesion layer over Cr is, during the last step to remove the top Cr layer, the Cr wet etchant is less likely to attack TiO_2, then the undercut might be avoided.

6.1.1 Effects on Plasmonic Fluorescence Enhancement

As a parallel effort to study the adhesion layer effect on the plasmonic field enhancement, we have made some $200nm$ thick Au films on top of Cr, Ti and TiO_2 adhesion layers with different thicknesses on $150\mu m$ thick quartz coverslips. A single aperture of about $120nm$[87] [88] round hole was then defined by FIB on all the test films.

Florescence correlation spectroscopy (FCS) was used to detect the single molecule florescence enhancement from a fluor. The results shown in Figure 6.1 indicate that in the case of $10nm$ TiO_2, the florescence can be enhanced as high as a factor of 25. This is a solid evidence that upon optimized adhesion layer, the field inside a nanoaperture can also be greatly enhanced, since the fluorescence emission of an emitter located inside a nanoaperture may be affected in two ways: by the local enhancement of the excitation intensity, or by the modification of the electromagnetic environment of the emitter.

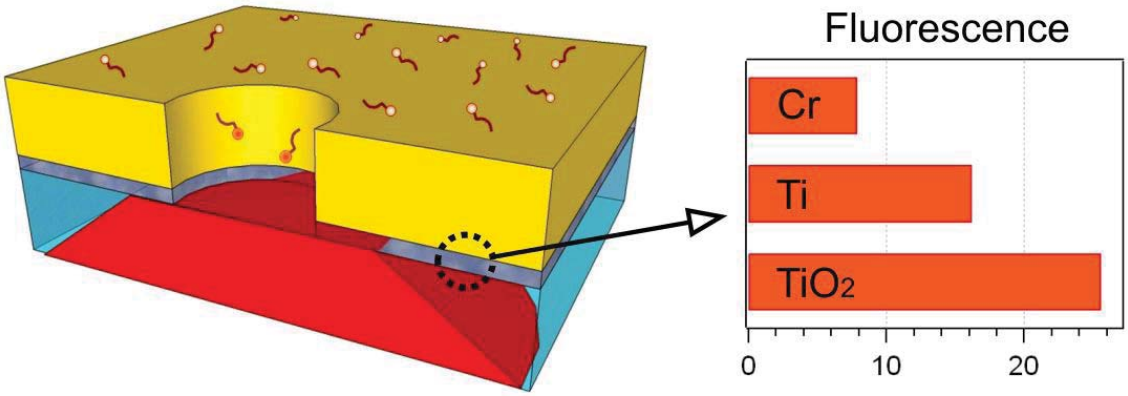

Figure 6.1: (Copyright permission of H. Aouani) Experimental schematic for single molecule florescence detection and simplified results for florescence enhancement. The fluor used here is Alexa-Fluor 647, which is a commonly used dye with emission spectrum ranging from 650 to $710nm$ and peak emission at $670nm$, and is excited by a $633nm$ He-Ne laser.[89]

6.1.2 Effects on Second Harmonic Generation and Third Harmonic Generation

In order to explore the adhesion layer effects on second order and third order harmonic generations, we had made the second harmonic generation and third harmonic generation double angle scans on a Cr adhesion sample, shown in Figure 6.2, and a TiO_2 adhesion sample, shown in Figure 6.3.

There is not much difference in the output signal levels for both second harmonic generation and third harmonic generation, which is contrary from what we expected. One possible reason is the harmonic signals are generated at the top surface. So if

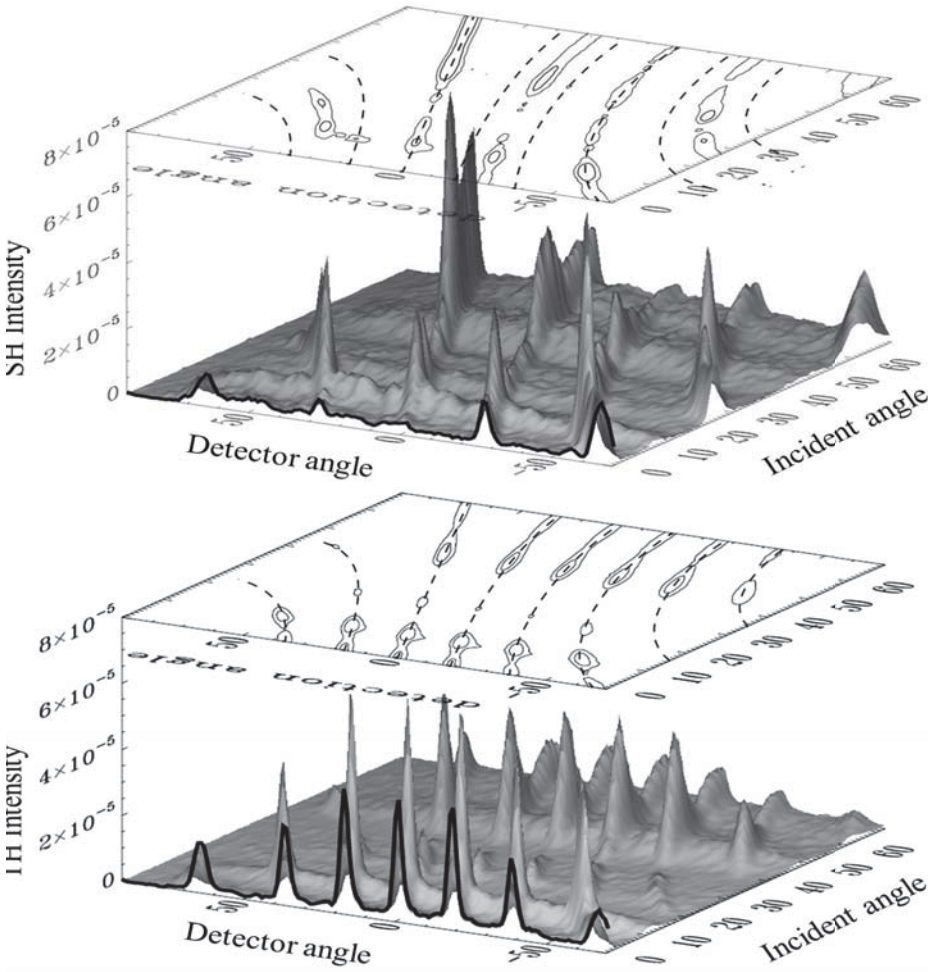

Figure 6.2: Double angle scan of second harmonic generation (top) and third harmonic generation (bottom) for a metallic hole array with $5nm$ Cr adhesion layer and $100nm$ Au, and the holes are arranged in square lattice with diameter of about $250nm$. Incident light is from the oscillator with average power about $40mW$.

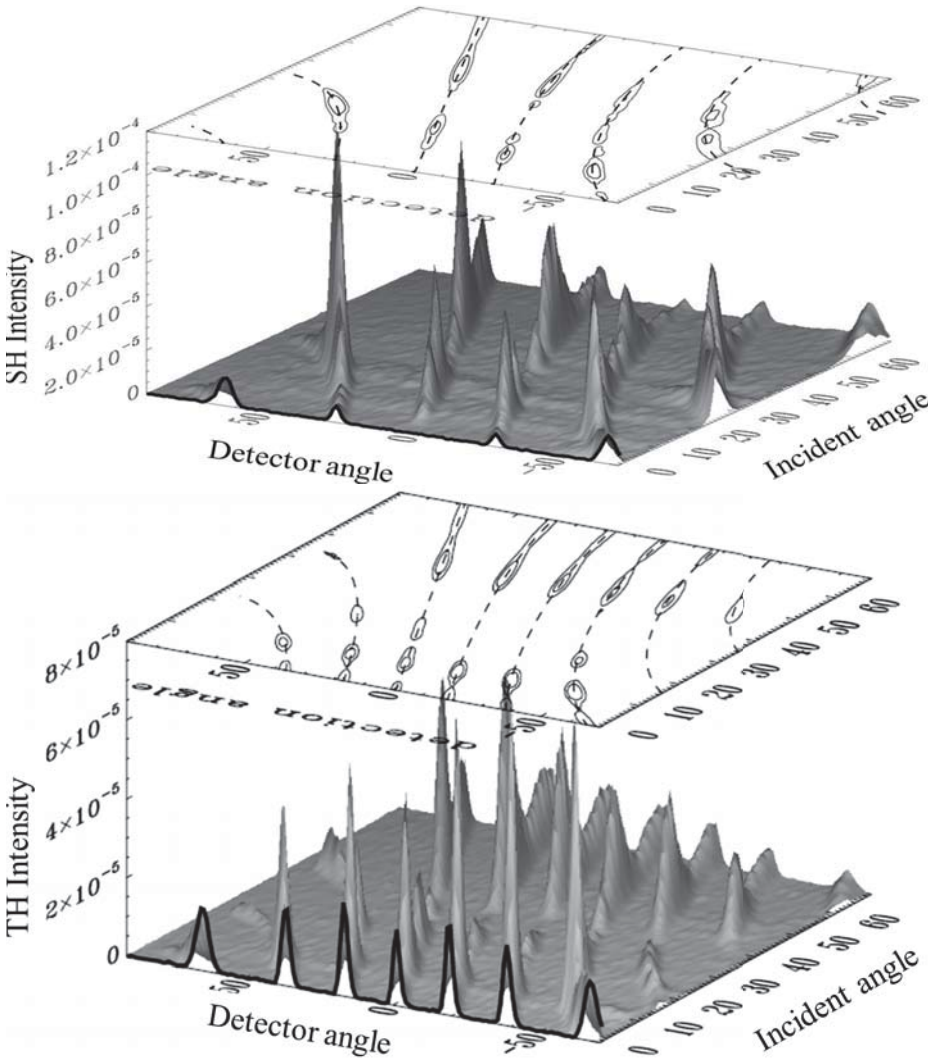

Figure 6.3: Double angle scan of second harmonic generation (top) and third harmonic generation (bottom) for a metallic hole array with $5nm$ TiO_2 adhesion layer and $100nm$ Au, and the holes are arranged in square lattice with diameter of about $250nm$. Incident light is from the oscillator with average power about $40mW$.

there is a difference between the adhesion layers, they can only impose some limited influences on second harmonic and third harmonic generation.

However, there are some differences between the second harmonic and third harmonic signals from different adhesion layers. The signals from the Cr adhesion layer have a higher level of background luminescence. The ones with TiO_2 have almost no background. Furthermore, the second harmonic generation signal from the TiO_2 adhesion layer is almost twice that of the Cr adhesion layer under the same experimental conditions.

6.2 Effects of Lattice Constant

The angular distribution of the extraordinary optical transmission for a square lattice hole array obeys the following relationship,

$$sin\theta = -i\left(\frac{\lambda_0}{a_0}\right) \pm \sqrt{-\left(\frac{j\lambda_0}{a_0}\right)^2 + \frac{\epsilon_d \epsilon_m}{\epsilon_d + \epsilon_m}} \tag{6.1}$$

Here, a_0 is the lattice constant of the hole array. When all the other conditions are held constant, such as keeping incident wavelength λ_0 at $800nm$, the peak positions will shift with change of the lattice constant a_0. Figure 6.4 plotted the measured fundamental transmission signal from hole arrays with different lattice spacings. It is clear that all the fundamental transmissions have followed the description of equation 6.1. And as the spacing becomes larger, the first peak has been shifted to a longer wavelength (or larger incidence angle in our case).

Similarly, the diffraction pattern also changes with the variation of lattice constant. Here we have used Λ to denote the lattice period, as illustrated in Figure 6.5.

$$sin\gamma = sin\theta + m\frac{\lambda}{2\Lambda} \tag{6.2}$$

$$sin\gamma = sin\theta + m\frac{\lambda}{3\Lambda} \tag{6.3}$$

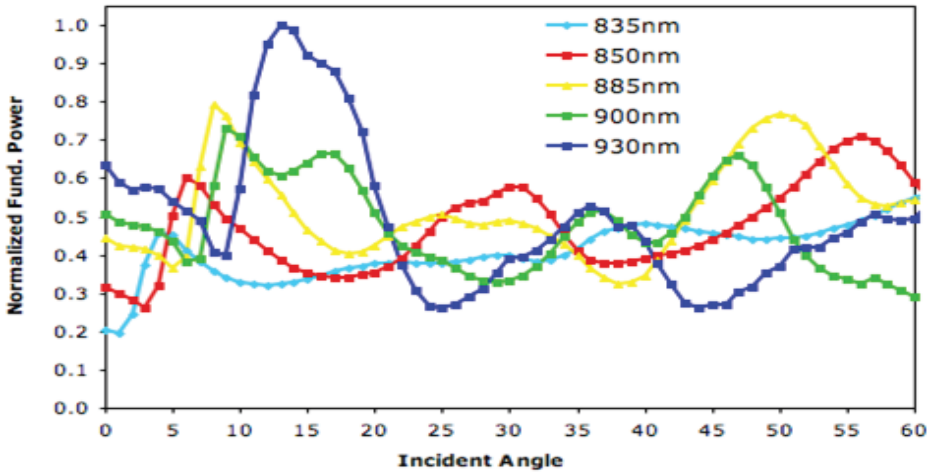

Figure 6.4: Fundamental transmission from a series of round hole arrays arranged in a square lattice with different spacing but having approximately the same aperture sizes. This sample has $5nm$ TiO_2 as an adhesion layer and $100nm$ Au film.

From these equations, we can see, for both second harmonic generation and third harmonic generation, the diffraction peaks are positioned further away with smaller lattice spacing. Both second harmonic generation and third harmonic generation diffraction orders follow the prediction of equations 6.3, as shown in Figure 6.5.

A clear trend can be seen if we plot together the second harmonic and third harmonic generations from a series of hole arrays with the same aperture size but different spacing, as shown in Figure 6.6. For second harmonic generation, all the angular peak positions shown here possess the characteristics we have discussed earlier: there is

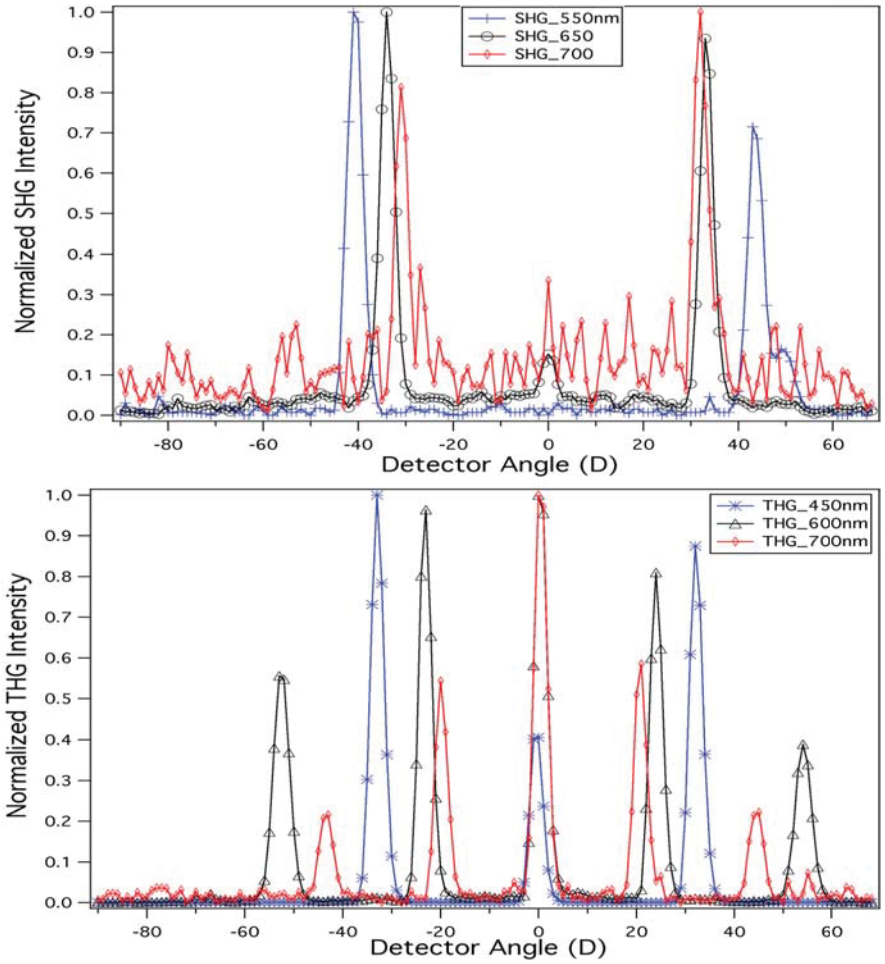

Figure 6.5: The diffraction order distribution of second harmonic generation and third harmonic generation from square lattice metallic hole arrays with different lattice constant: $550nm$, $650nm$ and $700nm$. The incident angle is zero degrees. With the increase of the lattice constant, the ± 1 orders appear at larger diffraction angles. The measurements are taken from hole arrays on the same chip with $5nm$ TiO_2 and $100nm$ Au and fabricated with the method described before.

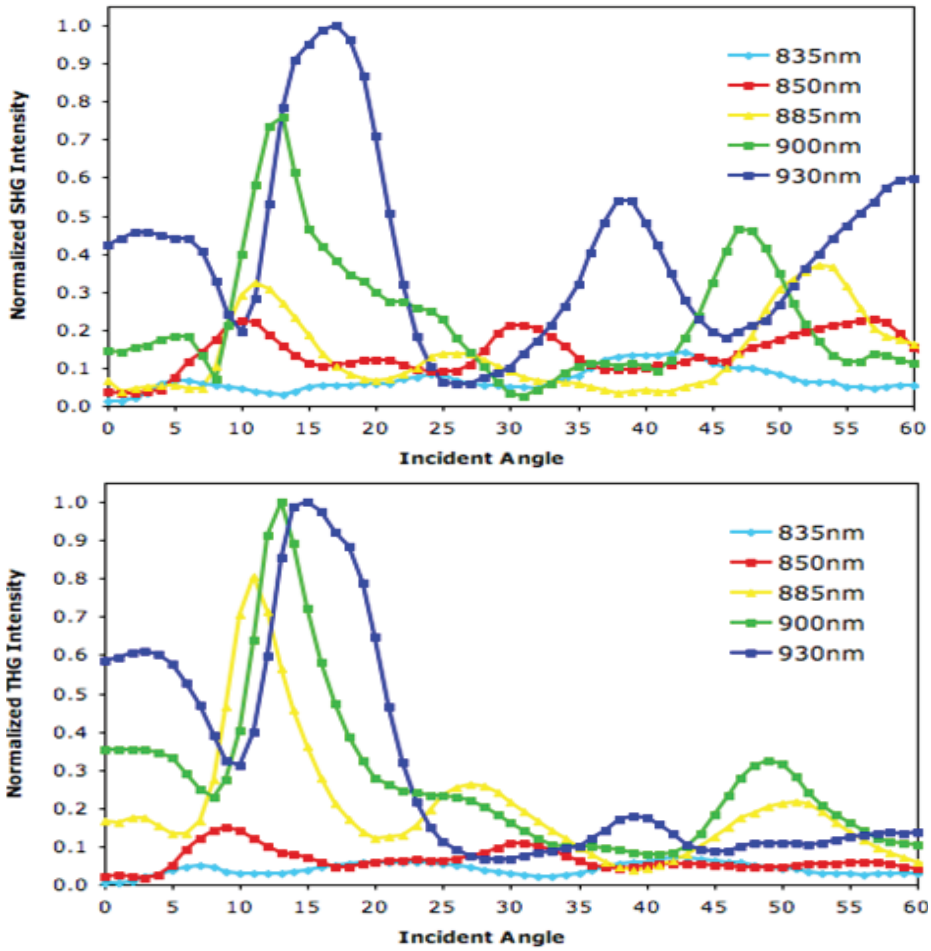

Figure 6.6: The angular distribution of second harmonic generation and third harmonic generation from the same samples used in Figure 6.4.

minimum intensity at normal incidence because of the inversion symmetry of the hole array, and the peak positions follow the description of equation 6.1. For angular distribution of the third harmonic generation for subwavelength metallic hole arrays, we would have expected a peak at normal incidence, because there is essentially no restriction for third harmonic generations at zero degrees incident angle. For both second harmonic generation and third harmonic generation, they all follow the peak positions of the fundamental transmission and also shows the angular shifts.

6.3 Effects of Aperture Shape

It has been shown previously that aperture shape has a strong influence on second harmonic generation at normal incidence, because the second harmonic generation

will be canceled out due to symmetry of the hole array and the aperture itself. By breaking the symmetry of the aperture itself, we can generate strong second harmonic signal at normal incidence. There are strong third harmonic generation signals at normal incidence because there is no symmetry restriction. For the third harmonic generation, the effect of the asymmetric aperture itself is to raise the overall signal level by about eight times, as shown in Figure 6.7, due to changes in field enhancement. Then it would be reasonable to extrapolate that optimization of the aperture shape may allow for even greater third harmonic conversion to be obtained.

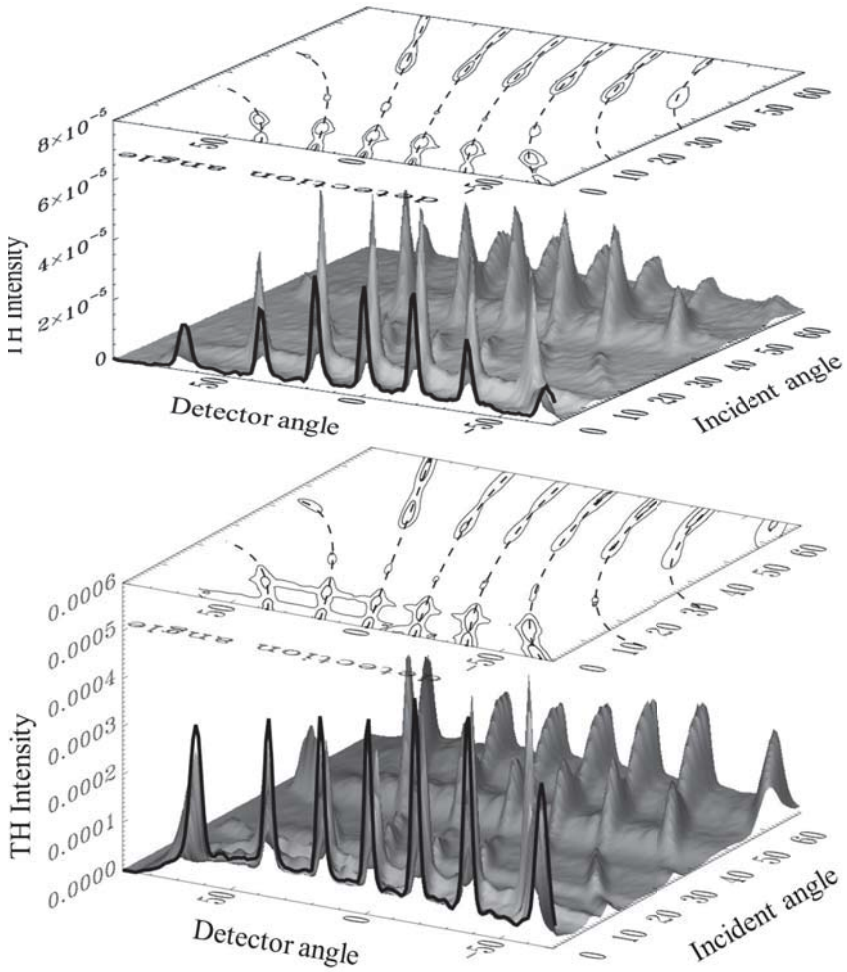

Figure 6.7: Double angle scan of third harmonic generation from square latticed metallic hole arrays, with $5nm$ Cr adhesion layer, and $100nm$ Au. The asymmetric hole array (top) produce about 8 times stronger third harmonic signal than that from a round hole array (bottom).

6.4 Effects of Aperture Size

Keeping the aperture spacing at about 885nm, we have investigated the effects of varying the aperture size on the fundamental transmission, second harmonic generation and third harmonic generation from round hole arrays composed of different aperture sizes. We have fabricated all the hole arrays on the same sample, and made the measurements within a relatively short time period to phase out all other factors which might complicate our experiments.

Figure 6.8 shows the fundamental transmission results from the samples of different hole sizes, but same spacings. From 250nm to 420nm diameter holes, the fundamental transmission increases with increasing aperture size. This is expected since larger holes will allow more light to pass. All the samples showed peaks almost at the exact same position, which are determined by equation 6.1.

There is something we thought might be interesting about the relative height of the third harmonic peaks, as the results show in Figure 6.9. For hole arrays with different sizes, at the first two peaks near zero and 10°, third harmonic generation decreases with aperture size, while at the third peak (near 30°) the third harmonic generation intensity increases with aperture size, and at the fourth peak near 50°, it decreases again. Individual apertures have cutoff frequencies,[84] [85] below which group velocity is minimized, resulting in an increase in intra aperture intensity. This

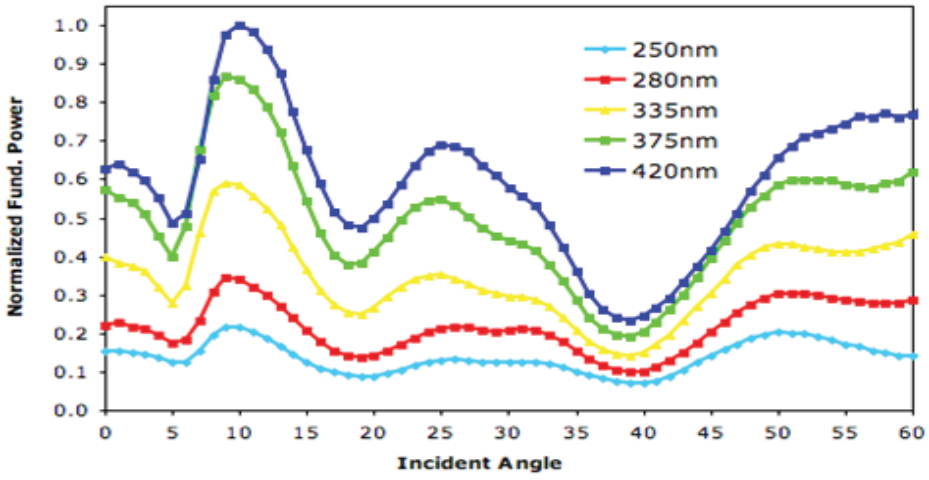

Figure 6.8: Fundamental transmission from samples of different hole sizes, but all have same spacing about 885nm arranged in square lattice.

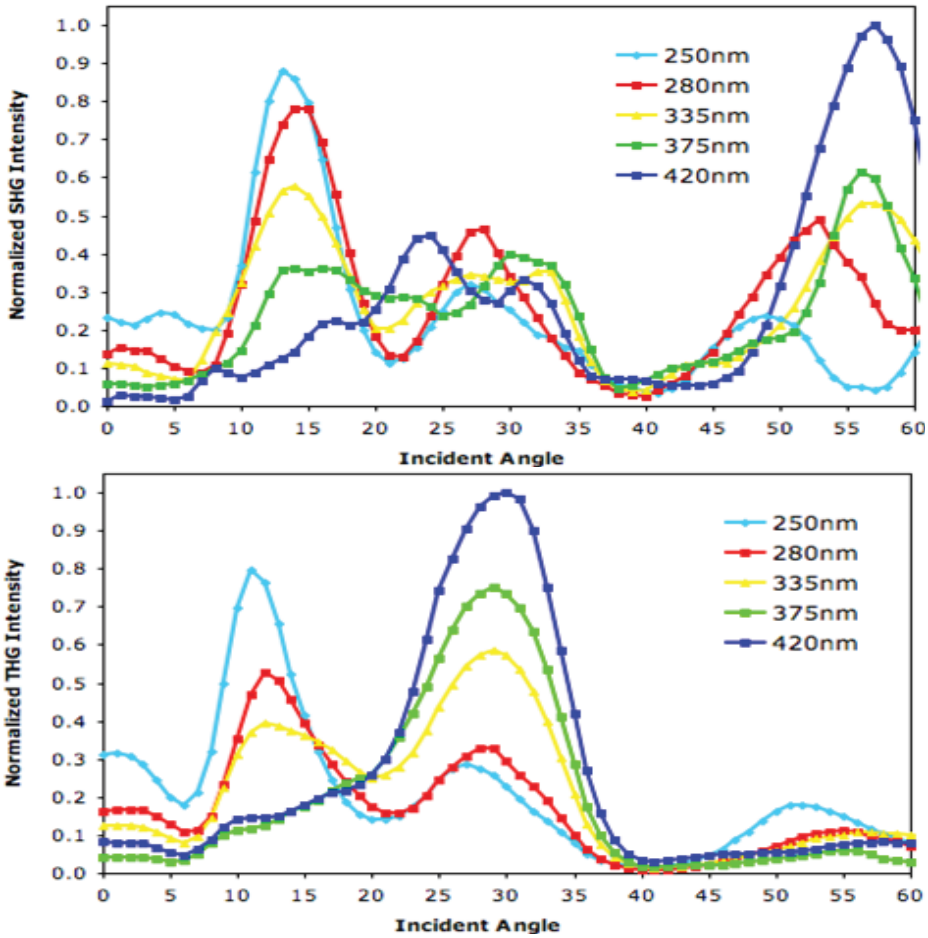

Figure 6.9: Second harmonic generation and third harmonic generation from a set of hole arrays having different hole size, but having the same spacing of about $885nm$ with square lattice arrangements.

explains why the third harmonic generation intensities decrease at 0°, 10° and 50°. For the increase at 30°, the fundamental difference between these two cases lies in the localization of the enhanced electromagnetic field. At 30°, the surface plasma polariton is localized at the substrate interface, where greater field overlap with the substrate occurs, so third harmonic generation is increased with aperture size.

6.5 Effects of Filling Materials

What would happen if the nanoholes are filled with materials, like SiO_2 or SiN_x in our case? In order to study the effects of the linear and nonlinear behavior to filling materials, we have used plasma enhanced chemical vapor deposition ($PECVD$) to grow a layer of SiO_2 or SiN_x on top of our samples, and also inside the holes. All

the films are thicker than the Au film thickness ($100nm$) to make sure the holes are fully filled. Then the same measurements are performed on these samples.

There are apparent peak shifts for the third harmonic peak positions, as shown in Figure 6.10, which correspond to the fundamental extraordinary transmission, even at normal incidence. This peak shift can be related to the ϵ_m in equation 6.1. $SiNx$ has a refractive index of about 2.05,[86] and this has shifted the position where the third harmonic generation appears, except at normal incidence.

On the other hand, the diffraction order of the second harmonic and third harmonic generations do not shift at all for hole arrays with and without the nonlinear filling material shown from Figure 6.11. Again, the explanation can be traced back to equation 6.3. Since there is no parameter of the material showing up in this equation, the diffraction peaks will appear at the same position as long as the incident angle is the same.

The samples filled with about $200nm$ $SiO2$ also showed similar behaviors for both sample scan and detector scan.

6.6 Conclusions and Discussions

More or less, all the factors we have studied here have affected the nonlinear processes, namely second harmonic generation and third harmonic generation.

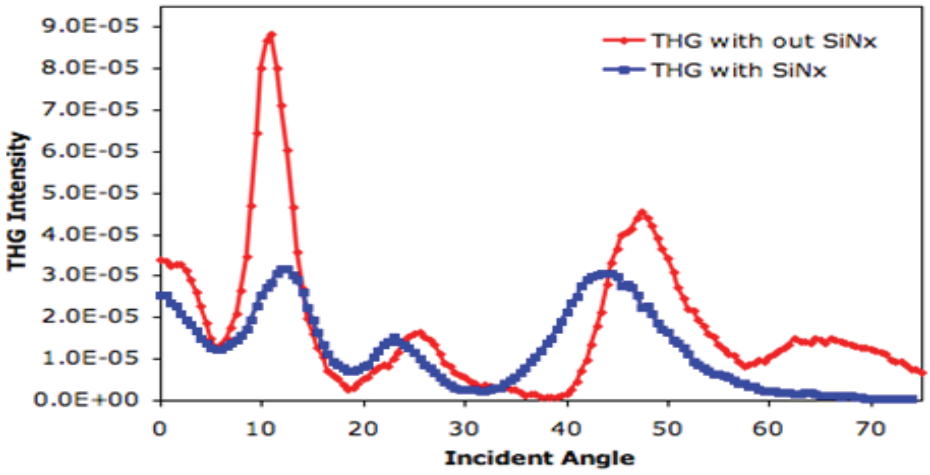

Figure 6.10: The angular distribution of third harmonic generation from a hole array filled with $245nm$ $SiNx$ and a hole array without any filling.

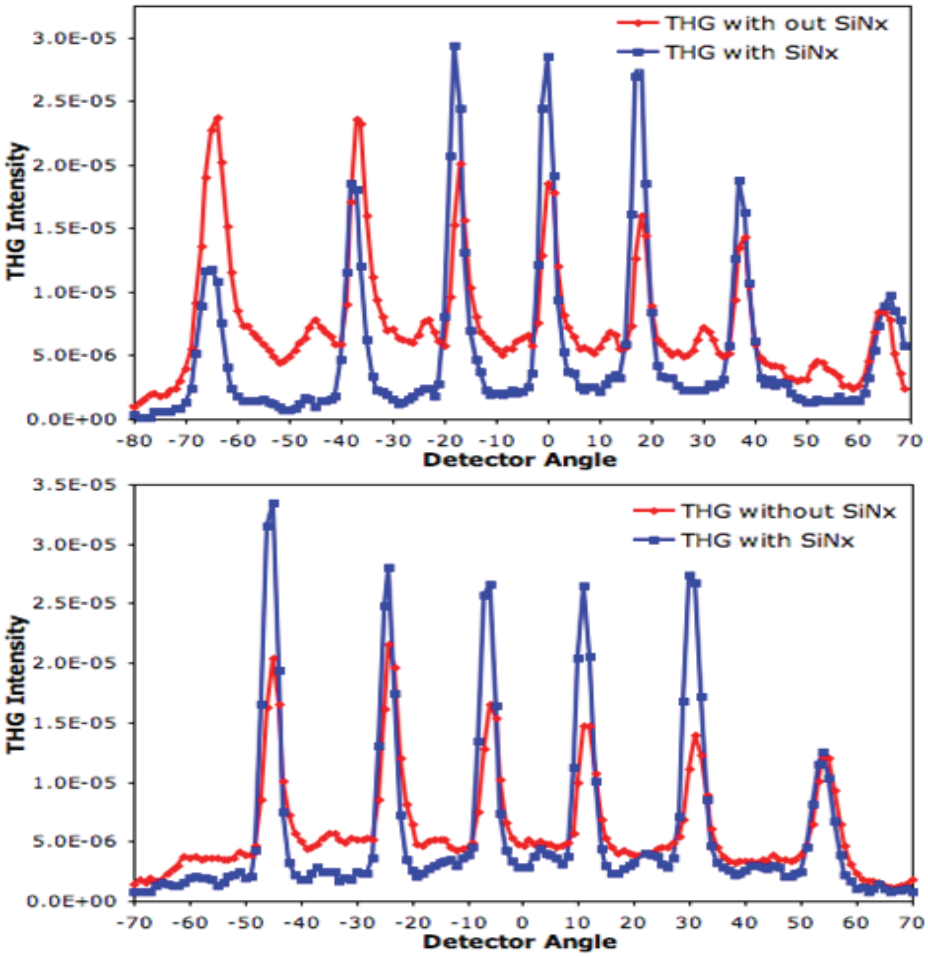

Figure 6.11: Third harmonic diffraction peaks at different incident angle: 0 degrees (left) and -45 degrees (right) for a hole array filled with $245nm$ $SiNx$ and a hole array without any filling. Both samples have $5nm$ Cr as the adhesion layer.

An adhesion layer like Cr is inherently very lossy. But we did not see too much difference between the Cr adhesion layer and the TiO_2 layer, which is suppose to be much less lossy while providing the same level of adhesion capability. One possible reason is that the nonlinear signal is generated on the incident side. The best way to test this would be fabricating samples with the same thickness Au film on the same thickness Cr and TiO_2 layers, and fabricate the hole arrays with the same method, preferably focused ion beam lithography, since it will avoid any difference from the holes.

The effect of lattice spacing is very obvious from our results. With the variation of lattice constants, the surface plasmon enhanced transmission shifted their peak

positions in the angular spectrum, and shifted the generated second harmonic and third harmonic peaks accordingly.

Filling the apertures with materials like SiO_2 and SiN_x should presumably enhance the nonlinear conversion efficiency since the SiO_2/Au and SiN_x/Au interfaces should have greater $\chi^{(2)}$ and $\chi^{(3)}$than the air/Au interface. This needs further exploration because we have not seen this effect yet from our results. Since SiO_2 and SiN_x have a higher refractive index than air, one role they have played in our study is to shift the extraordinary transmission peak positions in our angular spectrum. But the diffraction distribution did not change because the nonlinear filling should only change what happens on the incident side or inside the holes but not anything on the output side.

The most prominent attribute of the aperture shape is the nonlinear effect at normal incidence. By breaking the symmetry of the aperture itself but preserving the symmetry of the lattice, it can generate a second harmonic peak at normal incidence which is absent in case of hole arrays with inversion symmetry. One other contribution to the nonlinear process is to increase the overall signal level by about eight times, as shown in third harmonic generation.

CHAPTER 7

OTHER NONLINEAR OPTICAL PROCESSES: LUMINESCENCE AND SUPERCONTINUUM

For many of the second harmonic generation spectrum measurements, there exists a broadband background, [90] [91] [92] and Figure 7.1 shows a couple of examples. This strong background signal had been widely attributed to luminescence generation from noble metals.

Some of our results also showed this same characteristic background as the plot shown in Figure 7.2, even though we were not directly measuring the transmitted

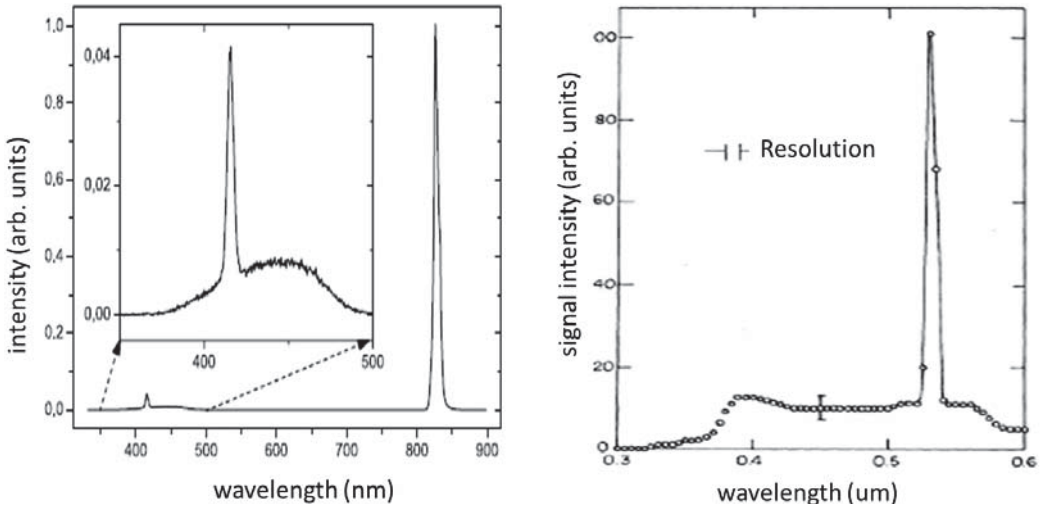

Figure 7.1: Second harmonic generation spectrum showing nonzero, broad-band luminescence background. The left[92] is a transmission spectrum through a square lattice subwavelength Au square hole array, the peak at $830nm$ is the fundamental transmission attenuated by color glasses, and the peak at $415nm$ is the generated second harmonic signal. The inset of the left image clearly shows that the second harmonic signal is sitting on top of a broad band multiphoton luminescence background. The right[90] is the reflected second harmonic generation from a roughened Ag surface, which possesses similar characteristics to the left one: the second harmonic generation peak is extremely sharp compared to the luminescence background.

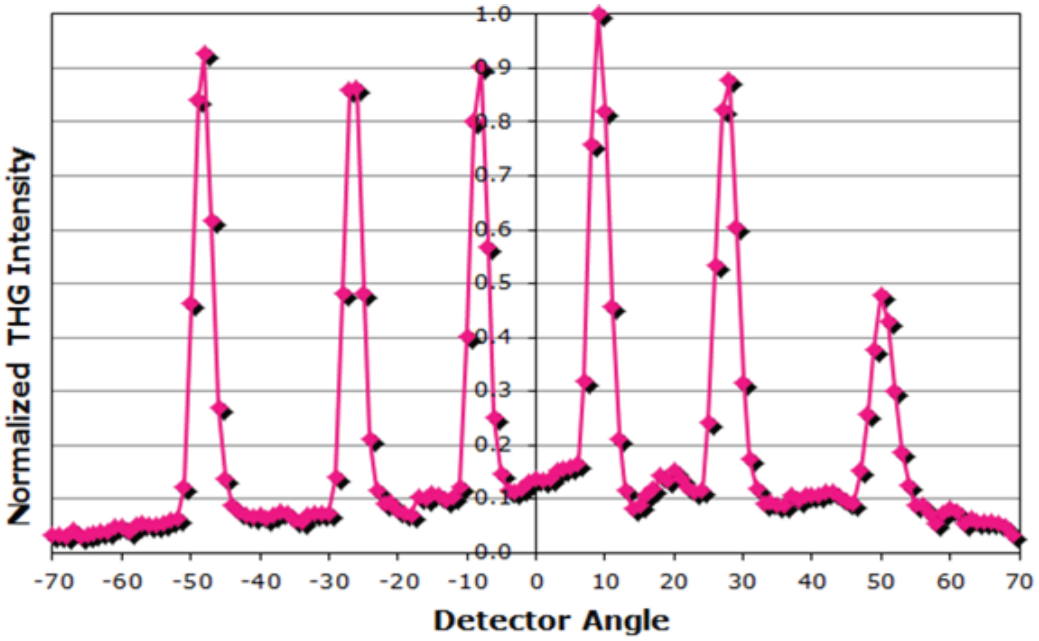

Figure 7.2: One of our experimental results showing third harmonic generation with broadband luminescence background. This plot shows a detector scan of third harmonic generation from a square lattice hole array with sample parked at -48 degrees. The sample used here has about 250nm diameter holes arranged in square lattice with 880nm spacing, and the film is a 5nm Cr adhesion layer and 100nm Au film. The broadband luminescence background on this spectrum is very clear.

second harmonic generation or third harmonic generation wavelength spectrum, but the angular spectrum.

Usually, the second harmonic generation signal shows as a very sharp peak on the spectrum, like the one on the right of Figure 7.1, but should have almost no background at all. So the question is what is the origin of the luminescence background. The understanding of the nature of this background may help us to study supercontinuum generation from hole arrays, which is a coherent process.

The angular scan technique used here provides a unique method to distinguish luminescence from harmonic generations and supercontinuum generation: luminescence shows up in the angular spectrum as a broad background due to the fact that it is an incoherent emission, while the coherent emission will have distinctive peaks through "angular filtering", as shown for second and third harmonic generation. In the same way, if supercontinuum from a hole array could be observed, we should be able to get distinguished peaks by scanning angular spectrum for all the wavelengths.

7.1 Luminescence from Noble Metals

Luminescence from noble metals was first discovered[96] from gold and copper by optically excited radiative recombination of electrons and holes in metals, and the schematic band structure is shown in Figure 7.3. Photoluminescence is one of the luminescence types which can be excited through many methods, such as nuclear radiation (scintillation), mechanical shock (triboluminescence), heat (thermoluminescence), chemical reactions (chemiluminescence), and electric fields (electroluminescence).

There are two prerequisites for luminescence: first, the luminescent material must have a semiconductor-like band gap structure with nonzero band gap E_g; second, energy must be provided to this material before luminescence can take place. The second requirement can be easily satisfied by the energy sourced mentioned above. For noble metal, like Au, the d bands and sp band are separated about $1.8eV$ at k_F.[97] For a roughened metal surface[98] or nanostructurized metal surfaces,[97 99] luminescence has been greatly enhanced due to localized surface plasmon resonances.

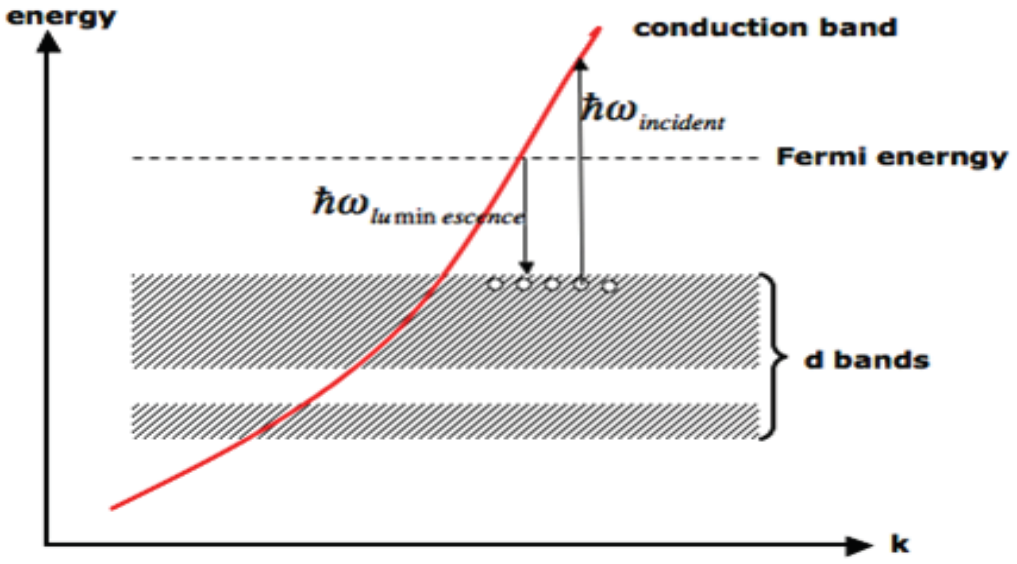

Figure 7.3: Schematic band structure[96] of a noble metal showing the excitation and luminescence process.

7.2 Multiphoton Luminescence

During double angle scan for second and third harmonic generation measurements, we have encountered a broad band background, as shown in Figure 7.4. We attribute the background to multiphoton luminescence.

Multiphoton luminescence is an nth order nonlinear process depending on how many photons are involved in the process. Multiphoton luminescence has gained attention from many researchers, especially those working on fluorescence imaging, because it is an up-conversion process and can be used to generate ultraviolet florescent images from visible or near infrared excitations.[93] [94] It allows spectral separation from the excitation light and from the induced fluorescence due to the utilization of a long wavelength, which only requires inexpensive ordinary visible or near infrared optical components rather than expensive ultraviolet adaptable optics such as nonfluorescent ultraviolet objective lenses.[95]

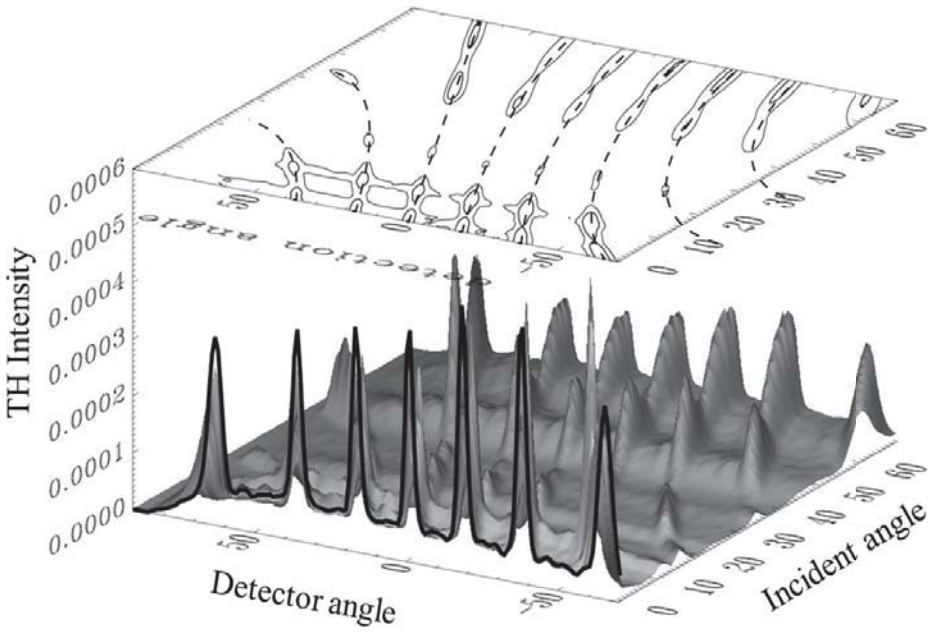

Figure 7.4: Double angle scan of third harmonic generation from square lattice asymmetric hole array with $5nm$ Cr adhesion layer and $100nm$ Au. Except the distinguished third harmonic signals, a broad band background can be clearly seen throughout all the incidence and detection angles.

7.2.1 Luminescence and Harmonic Generations

Multiphoton luminescence and corresponding harmonic generations are all nth order nonlinear optical processes, and they have the same power dependence, as shown in Figure 4.7, Figure 5.7 and Figure 7.4. For example, two-photon luminescence and second harmonic generation are both second order nonlinear processes, and three-photon luminescence and third harmonic generation are both third order nonlinear processes.

We believe that we have detected both harmonic generation and multiphoton luminescence when we were scanning the detector while parking the sample at a certain angle. To make this clear, we have split the results into pure harmonic generation peaks and the multiphoton luminescence background. To simplify this analysis, we have simply removed the peak data, taken the values on both sides right next to the bottom of the peaks, and averaged them to get the background values for the peak detector angles, as shown in Figure 7.5. For the plot of the harmonic generation peaks, we have subtracted the background values from the measurements.

It is clear that the harmonic generation and luminescence background have totally different behavior after diffraction from the metallic subwavelength hole array. In other words, the two-dimensional grating has served as a angular filter to distinguish the two types of signals: harmonic generation is a coherent process, so they will be diffracted by the two-dimensional hole array to specified angles, then the diffraction patterns are well-defined peaks. On the other hand, multiphoton luminescence is incoherent, so the generated luminescence will be at all directions. Then after the diffraction grating, they will appear to be broadband. When the detector is aligned with the normal direction of the hole array, the transmission will be the highest. As the detector moves away from this normal position, more light will be scattered away by the walls of the holes, so the signal drops as the detector moves. Finally, a dome-like background was formed on the angular spectrum.

7.2.2 Power Dependence of Multiphoton Luminescence

In order to find out what the backgrounds are on the angular spectra, we have measured the power dependence of the background with respect to the incident laser

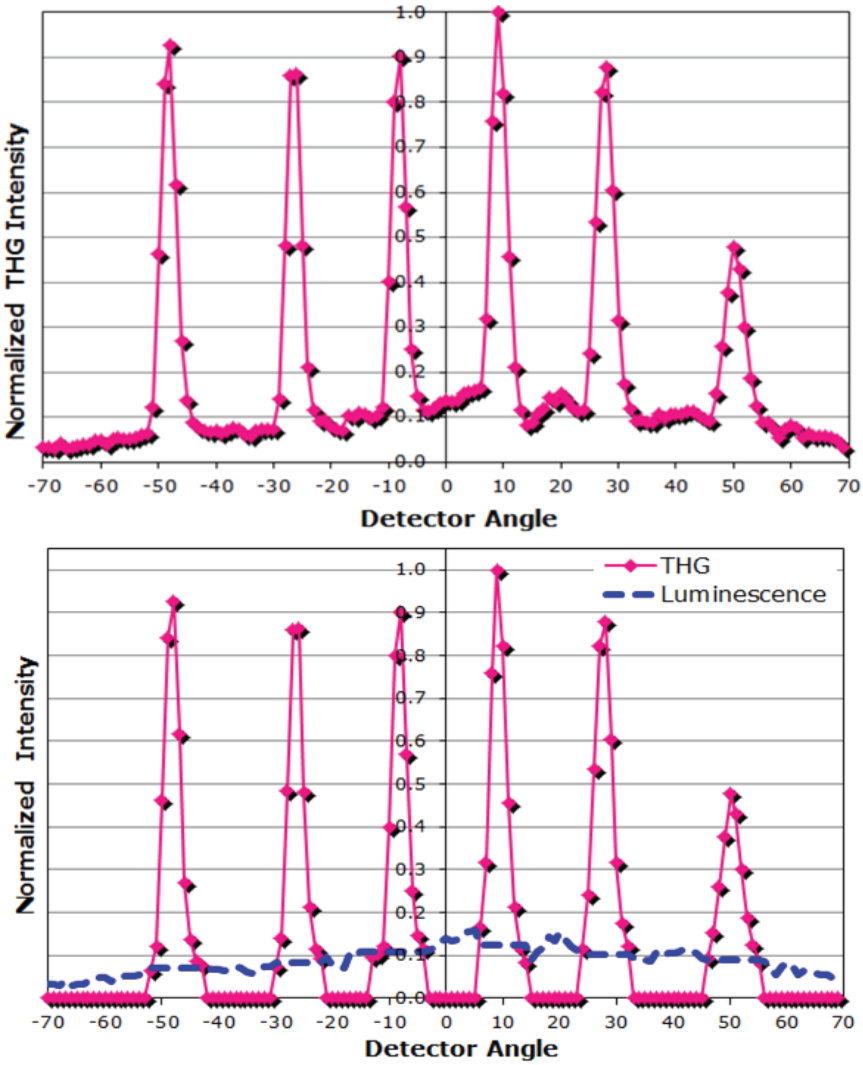

Figure 7.5: Detector scan of the third harmonic generation from a square lattice round hole array with sample setting at 48 degrees. The plot on the top is the original scan and the plot on the bottom is the separated third harmonic peaks (purple) and luminescence background (blue).

power. Since the detector scan gives a much clearer vision of the luminescence background, we have parked our sample at 45 degrees, which is one of the transmission peaks, and scanned the detector from one side of the sample back to the other side, with different incident laser power. This way, we can have the power dependence of the peaks, which are harmonic generation, and luminescence background at the same time. The data shown in Figure 7.6 are chosen with the detector at zero degrees. According to our calculation, there should not be anything except the background.

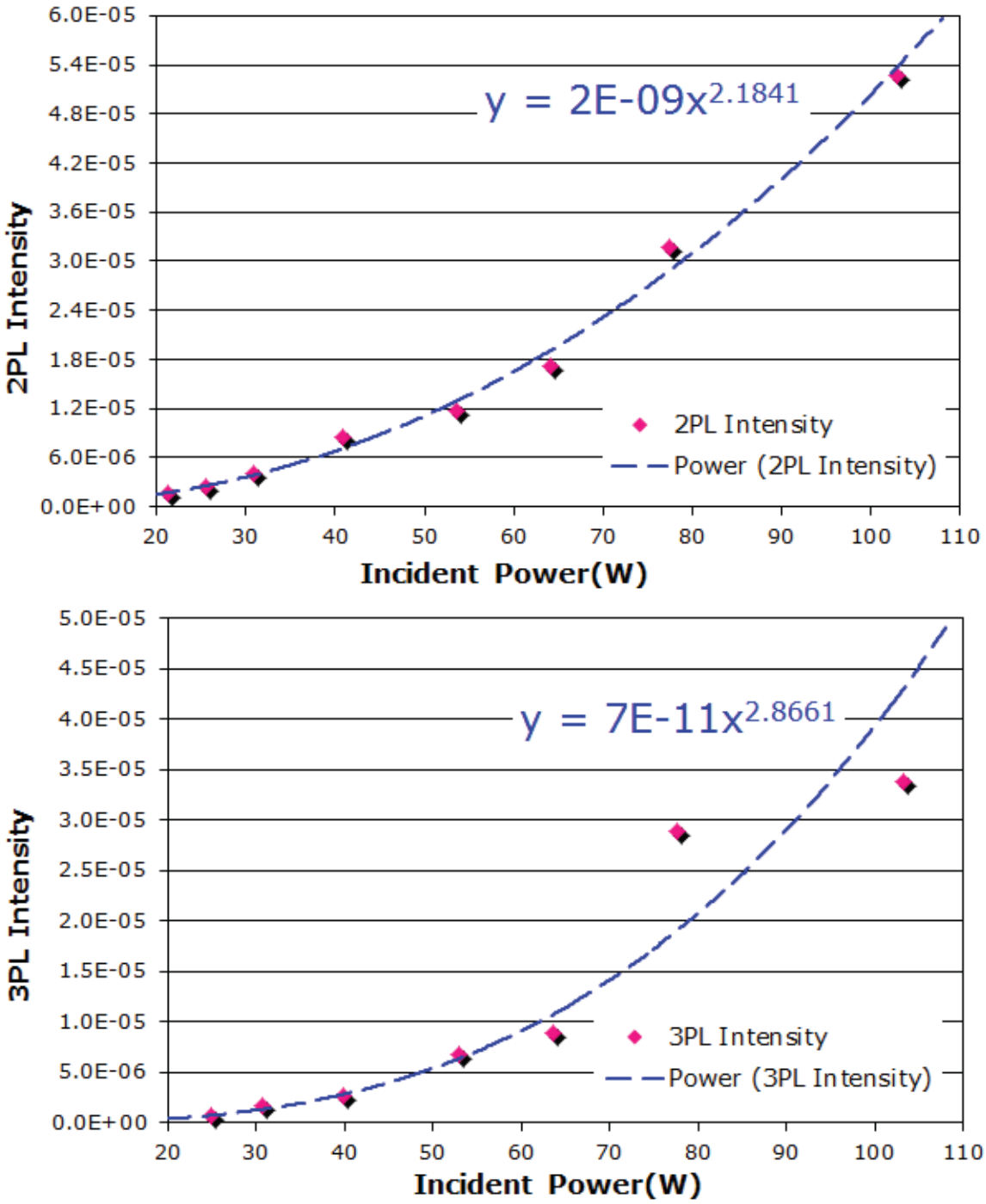

Figure 7.6: Power dependence of multiphoton luminescence. The two-photon luminescence (2PL) shows a power 2 dependence and the three-photon luminescence (3PL) shows a power 3 dependence. To make these measurements, the sample has been parked at a 45 degree incident angle, then a detector scan is performed at different incident power levels. The two-photon luminescence was taken along with second harmonic generation measurements and the three-photon luminescence with third harmonic generation measurements.

7.3 Supercontinuum and High Harmonic Generation

Supercontinuum generation is the phenomenon when narrow band incident laser pulses propagating through a nonlinear medium undergo extreme nonlinear spectral broadening to yield a broad band (usually a white light) spectrally continuous output. The first supercontinuum generation was reported by Alfano and Shapiro[101 102] in bulk glass. Since then, it has been the subject of numerous investigations in a wide variety of nonlinear media, including solids, organic and inorganic liquids, gases, and various types of waveguides, to explore the applications in diverse fields, such as spectroscopy, pulse compression and the design of tunable ultrafast femtosecond laser sources.

As an interesting and very challenging physical phenomenon, supercontinuum generation involves the whole range of classical nonlinear optical effects, like self-phase modulation, cross-phase modulation, four-wave mixing, stimulated Raman scattering, and so on. And they all add up together to produce emissions with extremely broad spectra.

In the year 2000, Ranka et.al[103] first demonstrated white light supercontinuum generation from a microstructured photonic crystal fiber (PCF) and the major results are quoted in Figure 7.7. The solid-cored PCF offers additional degrees of freedom than conventional optical fiber by modifying the hole size and periodicity to engineer the dispersion properties, like anomalous group-velocity dispersion (GVD) at wavelengths as short as $1\mu m$, thus making it possible for any femtosecond laboratory to carry out continuum-related nonlinear studies.

High-harmonic generation by focusing a femtosecond laser into a gas is a well-known method of producing coherent extreme ultraviolet light,[104 105 106] This nonlinear conversion process requires high pulse intensities, greater than $10^{13}\ W/cm^2$, which are not directly attainable using only the output power of a femtosecond oscillator. By utilizing the local field enhancement induced by resonant plasmons within a metallic nanostructure consisting of bow-tie-shaped gold elements on a sapphire substrate, S. Kim[107] has generated harmonics up to 17th order by just using the output laser from a standard $Ti:Sapphire$ oscillator, as sown in Figure 7.8. This has opened a way to generate higher order harmonics from the metallic hole arrays, since the similar local field happened inside the holes according to our results.

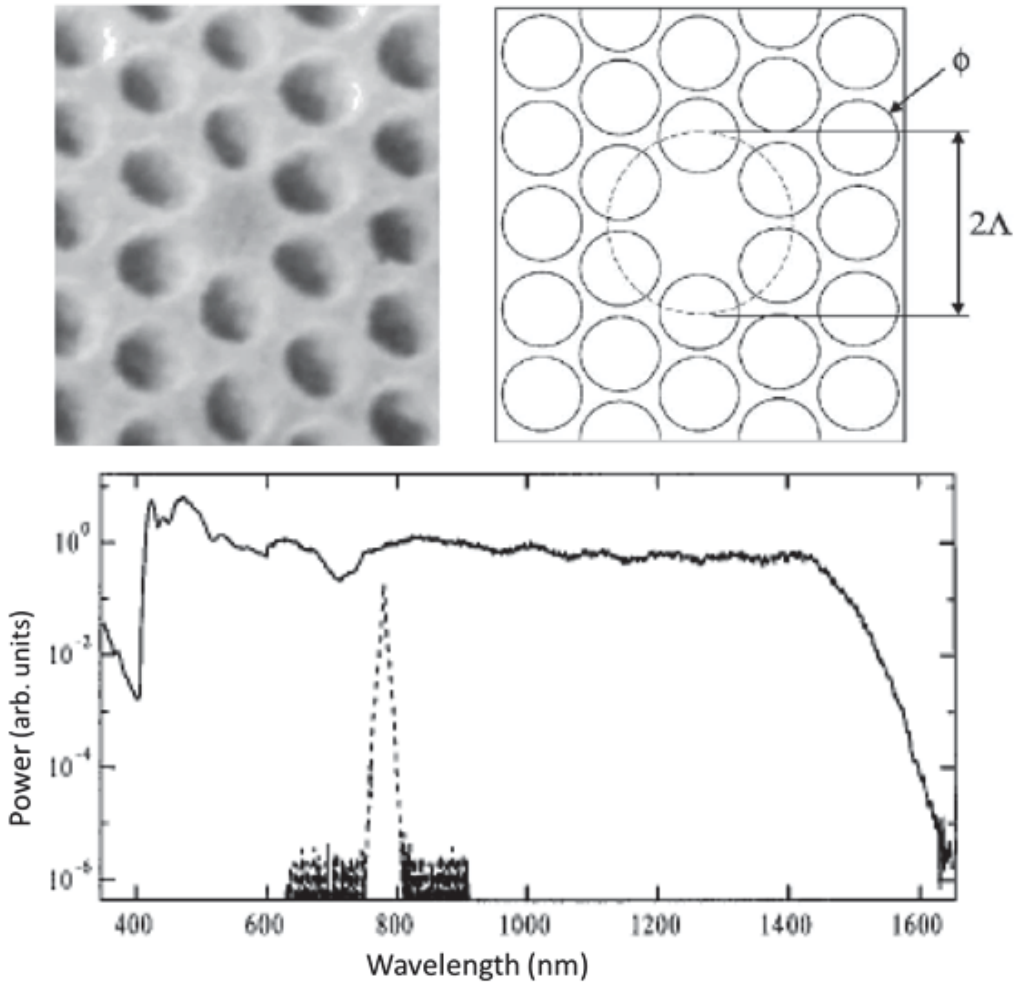

Figure 7.7: Photonic crystal fiber (PCF) used by Ranka[103] to generate white light supercontinuum (top). The parameter of the ideal hexagonal structure is Λ=1.7μm (pitch) and ϕ=1.3μm (hole diameter). The image on the right shows the optical spectrum of the generated continuum from the microstructured fiber. The inset of the dashed curve shows the spectrum of the initial 100fs pulse.

Another good example of local field enhancement responsible for possible supercontinuum generation has already been demonstrated by P. Muhlschlegel,[108] as shown in Figure 7.9. The resonant optical antenna are simply two nanometer sized gold bars separated about 20nm, and the incident laser used in this work was an 8ps pulsed laser with an average power of about 150μW. It is possible what they have seen is instead multiphoton luminescence because the spectrum they have shown cannot distinguish the multiphoton luminescence from the supercontinuum generation.

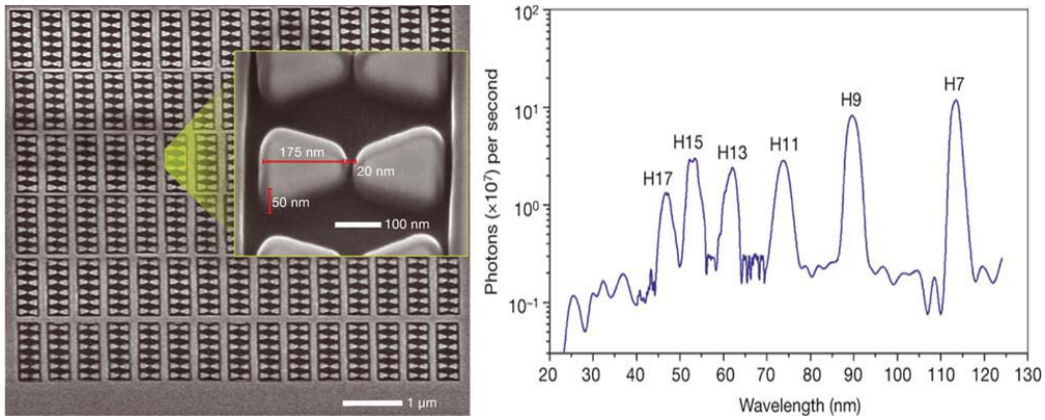

Figure 7.8: Bow-tie-shaped gold nanostructures[103] shown in the left SEM image, with a gap of about $20nm$ between the two triangle shaped elements, have the capability of enhancing the local field intensity by a factor of 20-40dB. The image on the right shows the up to 17th order harmonic generation from the injected argon gas. Only odd orders have been observed here because the antenna is centrosymmetric.

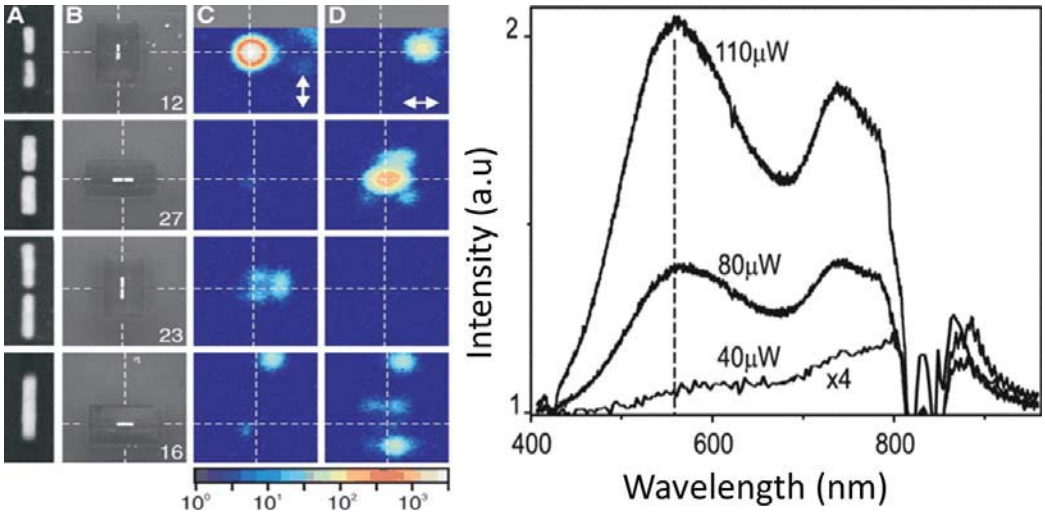

Figure 7.9: (Copyright permission for P. Muhlschlegel) The nanometer scaled optical antenna used by P. Muhlschlegel[?] to generate supercontinuum and the power dependence of the spectrum of the supercontinuum.

A rough caparison of the experimental parameters P. Muhlschlegel used and what we are using makes the study of supercontinuum generation from hole arrays quite promising. Their power density of incident light is about 3.75×10^7 W/m^2 (with $150\mu W$ power delivered on a 2×2 μm^2 area). In our case, the power density is on the order of 2.4×10^8 W/m^2 (with $75mW$ power focused on a spot with diameter of about $20\mu m$) which is one order higher than what they have been using. And more

importantly, we are using a femtosecond pulse rather than picosecond ones, with which it is easier to see the four-wave mixing process.

7.4 Preliminary Work on Supercontinuum Generation

We have tried to generate supercontinuum from the hole arrays, but with no success. According to the theory we have come up with from the results of second harmonic generation and third harmonic generation, if there is any supercontinuum generated, for example, with wavelength filtered at $500nm$, $600nm$, $700nm$, etc. we should be able to resolve them unambiguously by scanning the diffraction pattern through the hole arrays, just like with second order and third order generation, and the preliminary results are shown in Figure 7.10. Since the scattered light will have different wavelength corresponding to the selected filter sets, the transmitted supercontinuum should be diffracted at different angles.

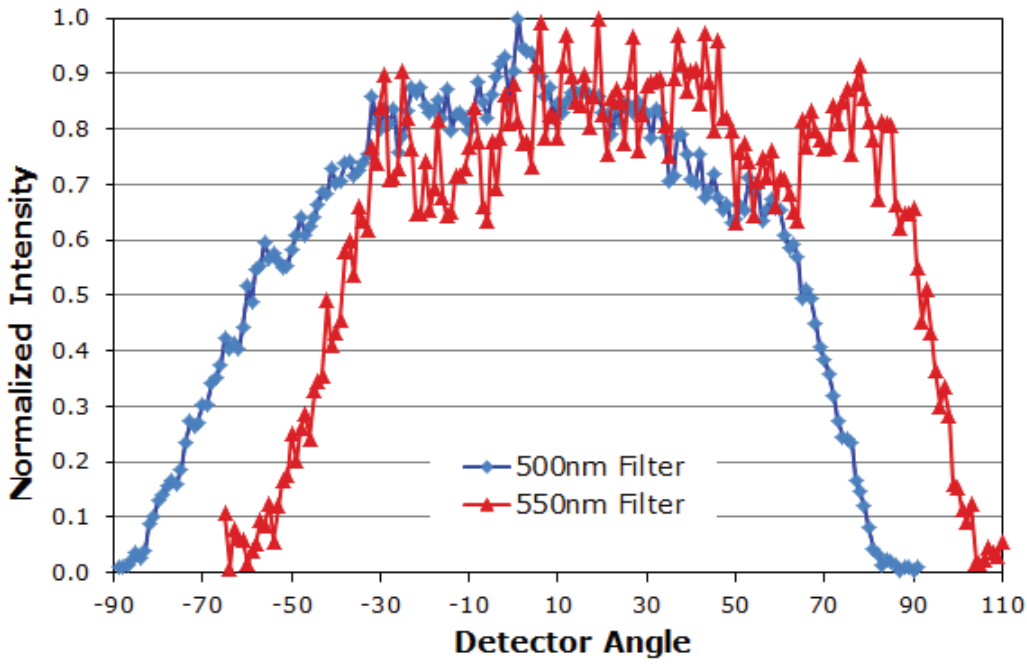

Figure 7.10: Our preliminary results for supercontinuum generation. For those measurements, we have parked the samples at one of the maximum positions of the fundamental transmission. The red curve was taken with the sample at 25 degrees, and the blue curve at 1 degree. For each wavelength, we have used two short pass filters $50nm$ longer than that and a corresponding bandpass filter with $20nm$ bandwidth on each side.

Again, we have used both the oscillator and regenerative amplifier as the light sources, for concern that the oscillator cannot provide pulses with high enough intensity. But unfortunately, we still have not seen any expected results so far. Only a luminescence background was observed with no distinctive peaks. The possible reason might be the local field enhancement is not high enough. Therefore, our best chance might be to switch to apertures with other shapes, for example, bow-ties,[109] [110] [111] which presumably have much better capability to enhance the local field in between their tips.

When we were trying to generate supercontinuum from the hole arrays, unavoidably, the background luminescence will always be there. The same method used to distinguish second harmonic generation and third harmonic generation with diffraction should be used for the same purpose.

7.5 Discussion and Conclusions

We have confirmed two- and three- photon luminescence from the hole arrays, but the question why we could not detect any supercontinuum signal is still wide open. The results we have found so far are most likely just multiphoton luminescence, and we need to modify our aperture designs, and to compare power dependence of luminescence at higher incidence power. If we see fourth power scaling without distinctive peaks for diffraction spectrum at all wavelengths, then that will provide evidence that supercontinuum can not be generated from the hole arrays.

CHAPTER 8

FUTURE WORK

As a conclusion, I am going to briefly discuss problems associated with future sample fabrication with electron beam lithography and dry etching, and possible solutions to overcome the obstacles. Based on our results and understanding of what was happening inside the apertures and with the array as a whole, some future work is also proposed in this chapter.

8.1 Nanofabrication Issues

So far, we have reported our work on nanofabrication to produce nanometer scale hole arrays on thin metallic films, especially on Au films. There are more challenges to fabricate the same kind of hole array samples on Al films since Ar plasma physical bombardment is not very effective to etch Al. Also, the grain size of sputtered aluminum is on the order of $100nm$, as shown in Figure 8.1, which basically eliminates any possibility of wet etching. In contrast, the grain size of gold is smaller than $50nm$. Aluminum has already been widely used in nanofabrication industry, but with the capability we have in the University of Utah, we have to approach it from other ways.

As we have discussed earlier in Chapter 2, by introducing a thin layer of chromium as a hard mask, we have successfully fabricated samples for this work. But the shortcomings of this method are also very obvious: we can not make very fine structures; we can not make complicated structures; damage on the substrate is possible; and this method is basically limited to work on soft materials like gold or cooper, any material harder than chromium is not going to work. For instance, we can not use this method to make any sample on Al film, because aluminum very easily forms an oxide layer and it is very dense and resistant to Ar plasma physical bombardment.

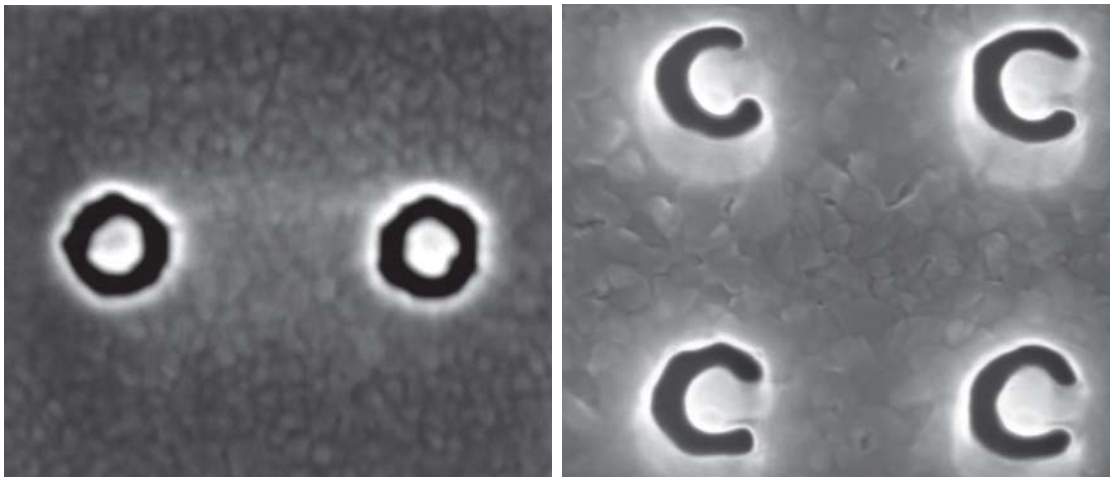

Figure 8.1: Nanoapertures fabricated on 100nm Au and Al films with FIB. These images clearly show the different grain size of those two material, which have been sputtered with the same tool at similar conditions. For Au, the grain size is normally in the range of 20 to 30nm, while the grain size of Al is about 50 to 100nm.

The nanofabrication method we have used so far is a top-down method, in which we have all the films sputtered prior to any fabrication process. Then all the nanofabrication steps are carried out on top of the films and work proceeds downwards.

One possible solution might be a bottom-up approach (or lift-off) as shown in Figure 8.2. In the lift-off case, the photoresist will be negative tone resist, like SU-8 from $MicroChem$.[100] After exposing to electron beam, the molecules of the resist will be interconnected and the exposed area will survive after development. In general, negative resists have excellent resistance to RIE and dry etching, but the disadvantage is that it is difficult to strip it off once it is stuck on the substrate. $OmniCoat$ will allow easier stripping of hard-to-remove photoresists and other materials. It is a polymer which is not sensitive to the electron beam so it will not be exposed during the EBL process. After development, it can be plasma etched with the protection of the negative photoresist, to expose the substrate for the next step. Then 5nm Cr or any other equivalent adhesion layer and the gold film with desired thickness (but not recommended for over 50nm) can be thermally evaporated to fill the resist-free area. Finally, the chip is then immersed into a resist stripping solution, like *Acetone* or $RemoverPG$. Since $OmniCoat$ can be easily dissolved, the negative photoresist can then be stripped away. Metal films will be left and the areas exposed will be the

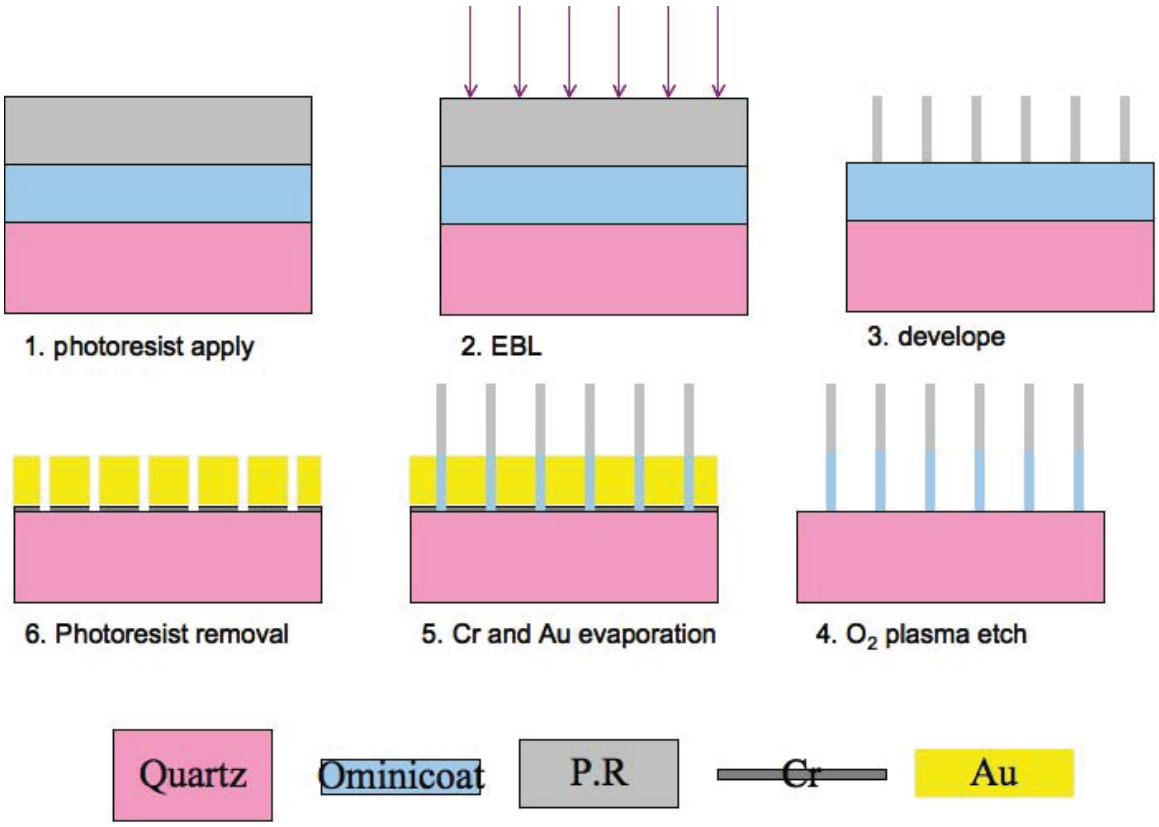

Figure 8.2: The lift-off process with negative tone photoresist and utilizing electron beam lithography. Etching process has been minimized to reduce the uncertainties and provide better control of fabrication.

holes. This method is potentially capable of making structures smaller and make the surface cleaner because the etching process has been minimized.

The other way out is to improve our current process by working out a better RIE recipe for gold. Ar ion milling did an adequate job on gold etching because gold is very soft, but it also etches other materials. Since it is an isotropic process, the structures have been unavoidably broadened. Ideally, we should have a recipe which only etches gold and leaves the mask layer untouched.

8.2 Quantum Dots in Nanohole Arrays

Similar to what we have done in our earlier works, we can fill the hole arrays with quantum dots rather than dielectric layers. Quantum dots are semiconductor nanostructures that confine the motion of conduction band electrons, valence band holes, or excitons (bound pairs of conduction band electrons and valence band holes)

in all three spatial directions. Small quantum dots, such as colloidal semiconductor nanocrystals, can be as small as 2 to 10 nanometers, as schematically shown in Figure 8.3. The spatial electronic confinement imposed by such a small volume produces energy levels with separations such that in the presence of an external perturbation, there will be induced transitions among these levels. If the quantum dots are arranged in a way that the self-consistent electromagnetic responses of all the quantum dots also induce resonances through the local field, this will greatly enhance the second harmonic generation by a factor of 2000 compared to that of the bulk samples.[112] The biggest challenge for quantum dots is that they are typically in the colloidal form and not easily arranged into a desired lattice arrangement.

However, the hole arrays have provided an ideal platform to provide the resonant feature of the local field needed for the enhancement of second harmonic generation from quantum dots. The quantum dots will be placed within about 5 nanometer proximity to the metal surface via a self-assembled monolayer formed with a quantum dot conjugated protein, such that direct energy transfer between the quantum dots excited state and surface plasmon modes occurs. With the presence of nanohole arrays, the coupling between the surface plasmon modes and excitation of the quantum

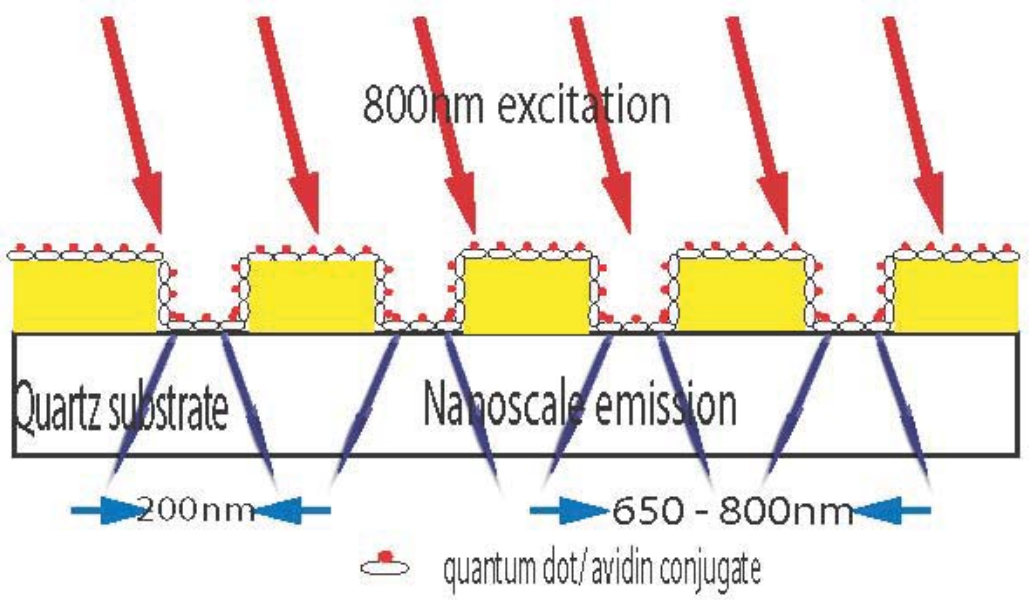

Figure 8.3: Conjugated quantum dots can be precisely placed inside the nanoholes even by a single layer with assistance of chemistry methods.

dots might happen, then, we would be able to see large enhancement of the second harmonic generation.

Since quantum dots have tunable absorption and emission bands, as illustrated in Figure 8.4, it would be interesting to study the behavior of the absorption and emission of the quantum dots with the presence of nanohole arrays.

Take the $QD800$ for example. It will absorb $400nm$ light and emit $800nm$ light. If it were illuminated with a $800nm$ laser, $400nm$ second harmonic generation will be produced, but the $QD800$ is supposed to absorb $400nm$ and emit $800nm$. Which effect dominates will probably depend on the competition of the two processes. If we use an OPA to generate a pump laser at $1600nm$, $800nm$ second harmonic will be generated and it should be resonantly enhanced.

Another idea of putting quantum dots into the nanoholes is to try to make a nanoscale laser, which is produced by the interaction between quantum dots excited by an external optical pump source and surface plasmon oscillations in a thin metal film. The surface plasmon mode will be amplified via stimulated emission [114] from the quantum dots. Laser emission would occur when the surface plasmon oscillations are scattered away from the nanohole arrays, thus achieving nanoscale laser output.

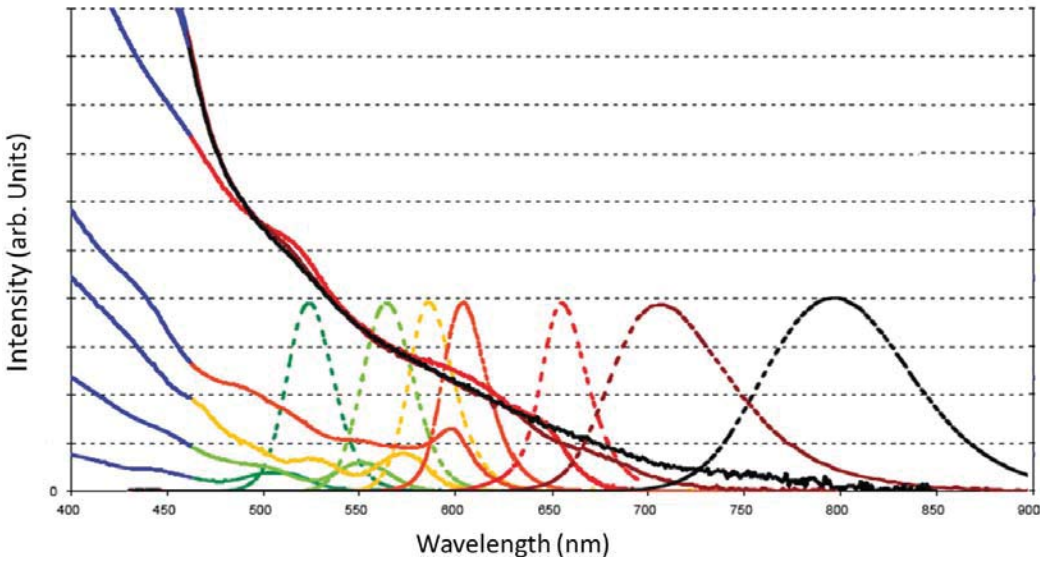

Figure 8.4: Absorption and emission spectra of different types of quantum dots.[113] The solid lines are the absorbency spectra, and the dotted lines are the emission spectra for the quantum dots.

8.3 Metamaterials

A metamaterial[115] is a material that gains its properties from its structure rather than directly from its composition. To distinguish metamaterials from other composite materials, the metamaterial label is usually used for a material that has unusual properties, such as a negative refractive index or infinite inertia (which are not found in naturally occurring materials).

In 1999, J. B. Pendry[116] proposed theoretically that microstructures built from nonmagnetic conducting sheets (the so-called double split-ring-resonator or SRR) could exhibit magnetic properties, and enhanced nonlinear optical properties could also arise.

In practice, people are using single split-ring-resonators rather than double SRRs, as shown in Figure 8.5.

A SRR is essentially a small LC circuit consisting of an inductance L and a capacitance C, where the ring forms one winding of a coil which gives the inductance and the ends of the ring form the plates of the capacitor. This combination of magnetic atoms[117] (split rings) and electric atoms (metallic wires) with negative permeability and permittivity can lead to materials with a negative refractive index. By tuning the lattice constant of densely packed SRRs smaller than the LC resonant wavelength, the SRR array can exhibit a resonance behavior of the magnetic permeability, with

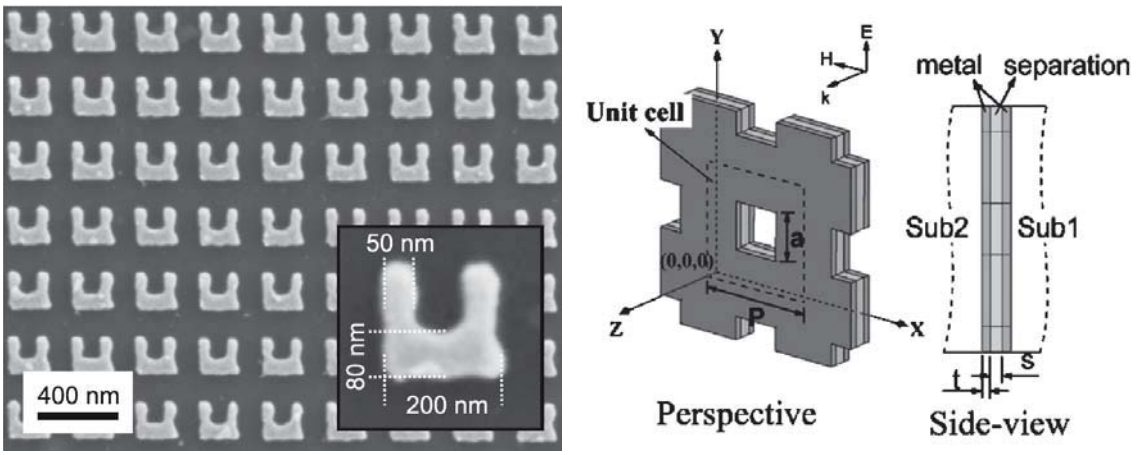

Figure 8.5: Two types of metamaterials. The split-ring-resonators (SRRs) have been widely studied in the microwave region and the trilayer metamaterial has only been theoretically studied but might be a good candidate for nonlinear optical studies.[122]

a magnetic resonance at the LC resonance frequency $\omega = \frac{1}{\sqrt{LC}}$[118] . In 2004, people[119] generated magnetic response of SRR metamaterials at 100 terahertz, which corresponds to $3\mu m$ wavelength. Magnetic response in telecommunication (200 terahertz, $1.5\mu m$) and visible frequencies (370 terahertz, $800nm$) was reported one year later by using the same SRR metamaterials. However, it is almost impossible to get down to the visible regime,[120] because at the low-frequency regime up to several terahertz, the magnetic resonance frequency scales reciprocally with the structure size, but at high frequencies, this linear scaling breaks down.

However, there is another type of metamaterial composed in a quite different way other than the SRRs but are more relevant to what we are doing. This kind of metamaterial is the combination of subwavelength metallic hole arrays and MIM metamaterials, as schematically shown in Figure 8.6.

Zhiming Huang etc.[121] proposed a pair of parallel thin metallic plates separated by a dielectric medium (MIM). Here is how it works: when an external electromagnetic field is exerted on it, the $\vec{E}$ and $\vec{H}$ fields will excite an electric current in the parallel plates. And a displacement current will also be excited by a time-varying electromagnetic field which flows between the plates. If the structure is misbalanced, there will be a nonzero net current between the plates. Therefore, a virtual current

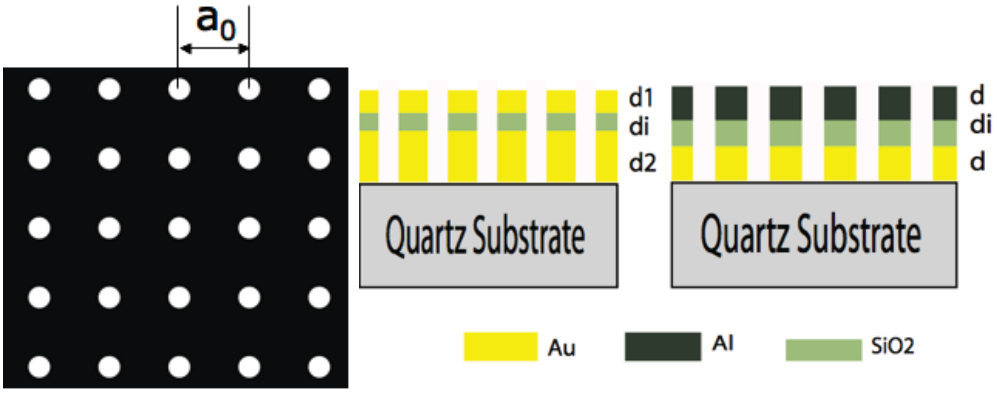

Figure 8.6: Schematics of top view and cross-section of proposed metamaterials. Viewed from top, this kind of metamaterial is the same as regular subwavelength metallic hole arrays. But from the cross-section, they are sandwiched layers: metal-insulator-metal. The unbalance can be realized in two ways: the two metal layers are the same metal but with different thickness, or the two layers have different materials with same thickness, or both the materials and thickness are different.

loop (VCL) will be formed along a contour through the plates and the dielectric medium. Theory[122] has shown by drilling a hole array on a trilayered metamaterial, one can achieve magnetic excitations arising from the localized SPPs at the optical regime down to visible range.

From the results we have found so far, the subwavelength metallic hole array alone cannot generate supercontinuum. By properly engineering the aperture spacing and thickness of different layers, we can localized the electric fields inside the apertures, excite and trap slow light modes inside the insulating layer. If resonance condition is reached, we might be able to achieve higher nonlinear optical conversion, and even generate supercontinuum out from this kind of structure.

REFERENCES

1. Y.R Shen, *The Principles of Nonlinear Optics,* (JOHN WILEY & SONS, 1984).

2. R. W. Boyd, *Nonlinear Optics,* Second Edition (Academic Press, 2003)

3. R.L. Sutherland, *Handbook of Nonlinear Optics,* Second Edition (Marcel Dekker, INC., 2003).

4. Wendell T. Hill and Chi H. Lee, *Light-Matter Interaction: Atoms and Molecules in External Fields and Nonlinear Optics,* (WILEY-VCH Verlag GmbH & Co. KGaA, Weinheim, 2007).

5. J. Wenger, D. Gerard, J. Dintinger, O. Mahboub, N. Bonod, E. Popov, T. W. Ebbesen and H. Rigneault, "Emission and Excitation Contributions to Enhanced Single Molecule Fluorescence by Gold Nanometric Apertures," Optics Express **16**, 3008–3020 (2008).

6. M. J. Levene, J. Korlach, S. W. Turner, M. Foquet, H. G. Craighead and W. W. Webb, "Zero-Mode Waveguides for Single-Molecule Analysis at High Concentrations," Science **299**, 682–686 (2003).

7. J. Wenger, P. F. Lenne, E. Popov and H. Rigneault, "Single Molecule Fluorescene in Rectangular Nano-Apertures," Optics Express **13**, 7035–7044 (2005).

8. H. Rigneault, J. Capoulade, J. Dintinger, J. Wenger, N. Bonod, E. Popov, T. W. Ebbesen, and P. F. Lenne, "Enhancement of Single-molecule Fluorescence Detection in Subwavelength Apertures," Physics Review Letters **95**, 117401 (2005).

9. A. G. Brolo, R. Gordon, B. Leathem and K. L. Kavanagh, "Surface Plasmon Sensor Based on the Enhanced Light Transmission through Arrays of Nanoholes in Gold Films," Langmuir **20**, 4813–4815 (2004).

10. E. C. Nice and B. Catimel, "Instrumental biosensors: new perspectives for the analysis of biomolecular interactions," BioEssays **21**, 339–352 (1999).

11. A. Partovi, D. Peale, M. Wuttig, C. A . Murray, G. Zydzik, L. Hopkins, K. Baldwin, W. S. Hobson, J. Wynn, J. Lopata, L. Dhar, R. Chichester and J. H-J. Yeh, "High-power laser light source for near-field optics and its application to high-density optical data storage," Applied Physics Letters **75**, 1515–1517 (1999).

12. F. Chen, A. Itagi, J. A. Bain, D. D. Stancil and T. E. Schlesinger, "Imaging of optical field confinement in ridge waveguides fabricated on very-small-aperture laser," Applied Physics Letters **83**, 3245–3247 (2003).

13. A. Sundaramurthy, P. J. Schuck, N. R. Conley, D. P. Fromm, G. S. Kino and W. E. Moerner, "Toward Nanometer-Scale Optical Photolithography: Utilizing the Near-Field of Bowtie Optical Nanoantennas," Nano Letters **6**, 355–360 (2006).

14. H. Raether, *Surface Plasmons on Smooth and Rough Surfaces and Gratings,* (Springer-Verlag, 1988).

15. C.F. Bohren, D.R. Huffman, *Absorption and Scattering of Light by Small Particles,* (New York: Wiley, 1983).

16. C. Pollock, M. Lipson, *Integrated Photonics,* (Kluwer Academic Publishers, 2003).

17. H. Bethe, "Theory of Diffraction by Small Holes," Physical Review **66**, 163–182 (1944).

18. C.J. Bouwkamp, "Diffraction Theory," Rep. Prog. Phys. **17**, 35–100 (1954).

19. D.E. Grupp, H.J. Lezec, T. Thio, T.W. Ebbesen, "Beyond the Bethe Limit: Tunable Enhanced Light Transmission through a Single Sub-Wavelength Aperture," Adv. Mater. **11**, 860–862 (1999).

20. T. Thio, K.M. Pellerin, R.A. Linke, H.J. Lezec, T.W. Ebbesen, "Enhanced light transmission through a single subwavelength aperture," Optical Letters **26**, 1972–1974 (2001).

21. H.J. Lezec, A. Degiron, E. Devaux, R.A. Linke, F. Martin-Moreno, L.J. Garcia-Vidal, and T.W. Ebbesen, "Beaming light from a subwavelength aperture," Science **297**, 220–222 (2002).

22. T. Thio, H.J. Lezec, T.W. Ebbesen, K.M. Pellerin, G.D. Lewen, A. Nahata, R.A. Linke, "Giant optical transmission of sub-wavelength apertures: physics and applications," Nanotechnology **13**, 429–432 (2002).

23. A. Nahata, R.A. Linke, T. Ishi, and K. Ohashi, "Enhanced nonlinear optical conversion using periodically nanostructured metal films," Optical Letters **13**, 429–432 (2002).

24. A. Degiron and T. W. Ebbesen, "Analysis of the transmission process through single apertures surrounded by periodic corrugations," Optics Express **12**, 3694–3700 (2004).

25. H. Cao, A. Agrawal, and A. Nahata, "Controlling the transmission resonance lineshape of a single subwavelength aperture," Optics Express **13**, 763–769 (2005).

26. F. J. Garca-Vidal, L. Martin-Moreno, H. J. Lezec and T. W. Ebbesen, "Focusing light with a single subwavelength aperture flanked by surface corrugations," Applied Physics Letters **83**, 4500–4502 (2003).

27. L. Martin-Moreno, F.J. Garca-Vidal, H. J. Lezec, A. Degiron, and T.W. Ebbesen, "Theory of highly directional emission from a single subwavelength aperture surrounded by surface corrugations," Physics Review Letters **90**, 167401 (2003).

28. T.W. Ebbesen, H.J. Lezec, H.F. Ghaemi, T. Thio, P.A. Wolff, "Extraordinary optical transmission through sub-wavelength hole arrays," Nature **391**, 667–669 (1998).

29. Ebbesen, Thomas W. , Ghaemi, Hadi. F., Thio, Tineke, Wolff, Peter A., "Subwavelength aperture arrays with enhanced light transmission," United States Patent 5973316, (1999).

30. http://www.freepatentsonline.com/REF5973316.html

31. T. Thio, H.F. Ghaemi, H.J. Jezec, P.A. Wolff, and T.W. Ebbesen, "Surface-Plasmon-Enhanced Transmission through Hole Arrays in Cr Films," J. Opt. Soc. Am. B **16** (10), 1743–1748 (1999).

32. T. Matsui, A. Agrawal, A. Nahata, and Z.V. Vardeny, "Transmission Resonances through Aperiodic Arrays of Subwavelength Apertures," Nature **446**, 517–521 (2007).

33. J.B. Abad, A. I. Fernandez-Dominguez, F.J. Garcia-Vidal, and L. Martin-Moreno, "Theory of Extraordinary Transmission of Light through Quasiperiodic Arrays of Subwavelength Holes," Physical Review Letters **99**, 203905 (2007).

34. K. J. Klein Koerkamp, S. Enoch, F.B. Segerin, N.F. van Hulst, and L. Kuipers, "Strong Influence of Hole Shape on Extraordinary Transmission through Periodic Arrays of Subwavelength Holes," Physical Review Letters **92**, 183901 (2004).

35. K. L. van der Molen, K. J. Klein Koerkamp, S. Enoch, F. B. Segerink, N. F. van Hulst, and L. Kuipers, "Role of Shape and Localized Resonances in Extraordinary Transmission through Periodic Arrays of Subwavelength Holes: Experiment and Theory," Physical Review B **72**, 045421 (2005).

36. Xiaolei Shi, Lambertus Hesselink and Robert L. Thornton, "Ultrahigh Light Transmission through a C Shaped Nanoapertures," Optical Letters **28**, 1320–1322 (2003).

37. Je Hong Kim and Patrick J. Moyera, "Transmission characteristics of metallic equilateral triangular nanohole arrays," Applied Physics Letters **89**, 121106 (2006).

38. Sun Mei, Liu Rong-Juan, Li Zhi-Yuan, Cheng Bing-Ying, Zhang Dao-Zhong, Yang Hai-Fang, and JinAi-Zi, "The Influence of Hole Shape on Enhancing Transmission through Subwavelength Hole Arrays," Chinese Physics **15**, 1591–1594 (2006).

39. Shaun M. Williams, Amanda D. Stafford, Trisha M. Rogers, Sarah R. Bishop, and James V. Coe, "Extraordinary Iinfrared Transmission Resonances of Metal Microarrays for Sensing Nanocoating Thickness," Applied Physics Letters **85**, 1472–1474 (2004).

40. A. Degiron, H. J. Lezec, W. L. Barnes and T. W. Ebbesen, "Effects of Hole Depth on Enhanced Light Transmission through Subwavelength Hole Arrays," Applied Physics Letters **81**, 4327–4329 (2002).

41. Je Hong Kim and Patrick J. Moyer, "Thickness Effects on the Optical Transmission Characteristics of Small Hole Arrays on Thin Gold Films," Optics Express **14**, 6595–6603 (2006).

42. M. J. Levene, J. Korlach, S. W. Turner, M. Foquet, H. G. Craighead, W. W. Webb, "Zero-Mode Waveguides for Signle-Molecule Analysis at High Concentration," Science **299**, 682–686 (2003)

43. W. L. Barnes, W. A. Murray, J. Dintinge, E. Devaux and T. W. Ebbesen, "Surface Plasmon Polaritons and Their Role in the Enhanced Transmission of Light through Periodic Arrays of Subwavelength Holes in a Metal Film," Physical Review Letters **92**, 107401 (2004)

44. N. Bloembergen, R.K. Chang, S.S Jha, and C.H. Lee, "Optical Second-Harmonic Generation in Reflection from Media with Inversion Symmetry," Physical Review **174**, 813–8222 (1968).

45. C.C Wang, "Second-Harmonic Generation of Light at the Boundary of an Isotropic Medium," Physical Review **178**, 1457–1461 (1969).

46. H.J. Simon, D.E. Mitchell, and J.G. Watson, "Optical Second-Harmonic Generation with Surface Plasmons in Silver Films," Physical Review Letters **33**, 1531–1534 (1974).

47. C.K Chen, A.R.B. De Castro, and Y.R. Shen, "Surface Enhanced Second-Harmonic Generation," Physical Review Letters, **46**, 145–148 (1981).

48. S.P. Mulvaney, M.D. Musick, C.D. Keating, and M.J. Natan, "Glass-Coated, Analyte-Tagged Nanoparticles: A New Tagging System Based on Detection with Surface-Enhanced Raman Scattering," Langmuir, **19**, 4784–4790 (2003).

49. Chanda Ranjit Yonzon, Christy L. Haynes, Xiaoyu Zhang, Joseph T. Walsh, Jr., and Richard P. Van Duyne, "A Glucose Biosensor Based on Surface-Enhanced Raman Scattering: Improved Partition Layer, Temporal Stability, Reversibility, and Resistance to Serum Protein Interference," Analytical Chemistry, **76**, 78–85 (2004).

50. YunWei Charles Cao, Rongchao Jin, and Chad A. Mirkin, "Nanoparticles with Raman Spectroscopic Fingerprints for DNA and RNA Detection," Science, **46**, 1536–1540 (2002).

51. T. Kawazoe, T. Shimizu, and M. Ohtsu, "Second harmonic generation in a near field optical fiber probe," Optics Letters, **26**, 1687–1689 (2001).

52. M. Airola, Y. Liu, S. Blair, "Second-harmonic generation from an array of subwavelength metal apertures," Journal of Optics A: Pure and Applied Optics, **7**, s118–s123 (2005).

53. J. A. H. van Nieuwstadt, M. Sandtke, R. H. Harmsen, F. B. Segerink, J. C. Prangsma, S. Enoch and L. Kuipers, "Strong modification of the nonlinear optical response of metal lic subwavelength hole arrays," Physical Review Letters, **97**, 146102 (2006).

54. A. Lesuffleur, L.K.S. Kumar, and R. Gordon, "Enhanced second harmonic generation from nanoscale double hole arrays in a gold film," Physical Review Letters, **88**, 221104 (2006).

55. A. Lesuffleur, L.K.S. Kumar, and R. Gordon, "Apex-enhanced second harmonic generation by using double hole arrays in a gold film," Physical Review B, **75**, 045423 (2007).

56. N. Feth, S. Linden, M. W. Klein, M. Decker, F. B. P. Niesler, Y. Zeng, W. Hoyer, J. Liu, S. W. Koch, J. V. Moloney and M. Wegener, "Second-harmonic generation from complementary split-ring resonators," Optics Letters, **33**(17), 1975–1977 (2008).

57. M. W. Klein, C. Enkrich, M. Wegener and S. Linden, "Second-Harmonic Generation from Magnetic Metamaterials," Science, **313**, 502–505 (2006).

58. Y. Zeng, W. Hoyer, J. Liu, S. W. Koch, J.V. Moloney, "Classical theory of second-harmonic generation from magnetic metamaterials," arXiv:0807.3531v1, http://arxiv.org/abs/0807.3531v1 (2008).

59. E. Reichmanis and A. E. Novembre, "Lithographic Resist Materials Chemistry," Annu. Rev. Mater. Sci., **23**, 11–43 (1993).

60. http://en.wikipedia.org/wiki/Photolithography

61. http://www.research.ibm.com/journal/rd/411/chiu.html

62. http://www.semiconductor.net/article/CA6319061.html

63. http://www.cnf.cornell.edu/cnf-spietoc.html

64. Zheng Cui, *Micro-Nanofabrication Technologies and Applications,* (Higher Education Press, Springer, 2005).

65. http://www.siliconfareast.com/lith-electron.htm

66. http://www.ee.byu.edu/photonics/holography.phtml?holography-see-all=true

67. http://pvd-coatings.co.uk/theory-of-pvd-coatings-magnetron.htm

68. T. Ishii, H. Tanaka, E. Kuramochi and T. Tamamura, "Fabrication of Nanometer-Order Dot Patterns by Lift-off Using a Fullerene-Incorporated Bilayer Resist System," Jpn J. Appl. Phys., **37**, 7202 – 7204 (1998)

69. T. Nishida, M. Notomi, R. Iga and T. Tamamura, "Quantum Wire Fabrication by E-Beam Elithography Using High-Resolution and High-Sensitivity E-Beam Resist ZEP-520" Jpn J. Appl. Phys., **31**, 4508 – 4514 (1992)

70. M. H. F. Overwijk, F. C. van den Heuvel and C. W. T. Bulle Lieuwma, "Novel scheme for the preparation of transmission electron microscopy specimens with a focused ion beam" J. Vac. Sci. Technol B., **11**, 2021 – 2024 (1993)

71. Yannick Poujet, Jerome Salvi and Fadi Issam Baida, "90% Extraordinary optical transmission in the visible range through annular aperture metallic arrays" Optics Letters, **32**, 2942 – 2944 (2007)

72. Rick Trebino, "Frequency-resolved Optical Gating: The Measurement of Ultrashort Laser Pulses," (Kluwer Academic Publishers, Springer, 2002).

73. J.D. Kafka and T. Baer, "Prism-pair dispersive delay lines in optical pulse compression," Optics Letters, **12**(6), 401–403 (1987).

74. R. L. Fork, O. E. Martinez, and J. P. Gordon, "Negative dispersion using pairs of prisms," Optics Letters, **9**(5), 150–152 (1984).

75. P.A. Franken, A.E. Hill, C.W. Peters and G. Weinreich, "Generation of Optical Harmonics," Physical Review Letters **7**, 118–120 (1961).

76. M. Schwartz, "Electrical Dipole Approximation and the Canonical Formalism in Electrodynamics," Physical Review Letters **123**, 1903–1908 (1961).

77. M. Airola, Y. Liu, and S. Blair, "Second-Harmonic Generation from an Array of Sub-wavelength Metal Apertures," J. Opt. A: Pure and Appl. Opt. **7**, S118–S123 (2005).

78. K. Liu, L. Zhan, Z. Y. Fan, M. Y. Quan, S. Y. Luo, and Y. X. Xia, "Enhancement of Second-Harmonic Generation with Phase-matching on Periodic Sub-wavelength Structured Metal Film," Opt. Commun. **276**, 8–13 (2007).

79. M. D. McMahon,R. Lopez, R. F. haglund, Jr., E. A. Ray, and P. H. Bunton, "Second-Harmonic GenerationFrom Arrays of Symmetric Gold Nanoparticles," Physical Review B. **73**, 041401 (2006).

80. B. K. Canfield, H. Husu, J. Laukkanen, B. Bai, M. Kuittinen, J. Turunen, and M. Kauranen, "Local Field Asymmetry Drives Second-Harmonic Generation in Noncentrosymmetric Nanodimers," Nano Letters **7**, 1251–1255 (2007).

81. B. Lamprecht, A. Leitner, and F. R. Aussenegg, "SHG Studies of Plasmon Dephasing in Nanoparticles," Applied Physics B **68**, 419–423 (1999).

82. A. M. Moran, J. Sung, E. M. Hicks, R. P. van Duyne, and K. G. Spears , "Second Harmonic Excitation Spectroscopy of Silver Nanoparticle Arrays," J. Phys. Chem. B **109**, 4501–4506 (2005).

83. K. Liu, L. Zhan, Z. Y. Fan, M. Y. Quan, S. Y. Luo, and Y. X. Xia, "Enhancement of second-harmonic generation with phase-matching on periodic sub-wavelength structured metal film," Opt. Commun. **276**, 8–13 (2007).

84. J. A. H. van Nieuwstadt, M. Sandtke, R. H. Harmsen, F. B. Segerink, J. C. Prangsma, S. Enoch, and L. Kuipers, "Strong Modification of the Nonlinear Optical Response of Metallic Subwavelength Hole Arrays," Physical Review Letters, **97**, 146102 (2006).

85. E. Popov, M. Neievre, J. Wenger, P.-F. Lenne, H. Rigneault, and P. Chaumet, "Field Enhancement in Single Subwavelength Apertures," Journal of the Optical Society of America A, **23**, 2342-2348 (2006).

86. http://www.siliconfareast.com/sio2si3n4.htm

87. Davy Gerard, Jerome Wenger, Nicolas Bonod, Evgeni Popov, Herve Rigneault, Farhad Mahdavi, Steve Blair, Jose Dintinger and Thomas W. Ebbesen, "Nanoaperture - enhanced fluorescence: Towards higher detection rates with plasmonic metals," Physical Review B, **77**, 045413 (2008).

88. Jerome Wenger, Davy Gerard, Jose Dintinger, Oussama Mahboub, Nicolas Bonod, Evgeny Popov, Thomas W. Ebbesen and Herve Rigneault "Emission and excitation contributions to enhanced single molecule fluorescence by gold nanometric apertures," Optics Express, **16**, 3008 – 3020 (2008).

89. Heykel Aouani, Jerome Wenger, Davy Gerard, Herve Rigneault, Eloise Devaux, Thomas W. Ebbesen, Farhad Mahdavi, Tingjun Xu and Steve Blair, "Crucial Role of the Adhesion Layer on the Plasmonic Fluorescence Enhancement," ACS Nano, **3**, 2043 – 2048 (2009).

90. C. K. Chen, A. R. B. de Castro and Y. R. Shen, "Surface-Enhanced Second-Harmonic Generation," Physical Review Letters, **46**, 145–148 (1981).

91. W. J. Fan, S. Zhang, K. J. Malloy and S. R. J. Brueck, "Second Harmonic Generation from Patterned GaAs inside a Subwavelength Metallic Hole Array," Optics Express, **46**, 9570–9575 (1981).

92. J. A. H. van Nieuwstadt, M. Sandtke, R. H. Harmsen, F. B. Segerink, J. C. Prangsma, S. Enoch and L. Kuipers, "Strong Modification of the Nonlinear Optical Response of Metallic Subwavelength Hole Arrays," Physical Review Letters, **97**, 146102 (2006).

93. W. Denk, J. H. Strickler, and W. W. Webb, "Two-Photon Laser Scanning Fluorescence Microscopy," Science, **248**, 73–76 (1990).

94. S. W. Hell, K. Bahlmann, M. Schrader, A. Soini, H. Malak, I. Gryczynski, J. R. Lakowicz and J. Biomed, "Three-Photon Excitation in Fluorescence Microscopy," Journal of Biomedical Optics, **1**, 71–74 (1996).

95. H. Kano and S. Kawata, "Two-Photon-Excited Fluorescence Enhanced by a Surface Plasmon," Optical Letters, **15**, 1848–1850 (1996).

96. A. Mooradian, "Photoluminescence of Metals," Physical Review Letters, **3**, 185–187 (1969).

97. M. R. Beversluis, A. Bouhelier and L. Novotny, "Continuum generation from single gold nanostructures through near-field mediated intraband transitions," Physical Review B, **68**, 115433 (2003).

98. G. T. Boyd, Z. H. Yu and Y. R. Shen, "Photoinduced luminescence from the noble metals and its enhancement on roughened surfaces," Physical Review B, **33**, 7923–7936 (1986).

99. J. P. Wilconxon, J. E. Martin, F. Parsapour, B. Wiedenman and D. F. Kelley, "Photoluminescence from nanosize gold clusters," Journal of Chemical Physics, **108**, 9137–9148 (1998).

100. http://www.microchem.com/products/sueight.htm

101. R. R. Alfano and S. L. Shapiro, "Emission in the Region 4000 to 7000 via Four-Photon Coupling in Glass," Physical Review Letters **24**, 584–587 (1970).

102. R. R. Alfano and S. L. Shapiro, "Observation of Self-Phase Modulation and Small-Scale Filaments in Crystals and Glasses," Physical Review Letters **24**, 592–594 (1970).

103. Jinendra K. Ranka, Robert S. Windeler, and Andrew J. Stentz, "Visible Continuum Generation in AirSilica Microstructure Optical Fibers with Anomalous Dispersion at 800nm," Optics Letters **25**, 25–27 (2000).

104. P. B. Corkum, "Plasma Prospective on Strong-Field Multiphoton Ionization," Physical Review Letters **71** , 1994–1997 (1993)

105. M. Lewenstein, P. Balcou, M. Y. Ivanov, A. L. Huillier and P. B. Corkum "Theory of High-Harmonic Generation by Low-Frequency Laser Fields," Physical Review A **79**, 2697–2699 (1994)

106. Z. Chang, A. Rundquist, H. Wang, M. M. Murnane and H. C. Kapteyn, "Generation of Coherent Soft X Rays at 2.7 nm Using High Harmonics," Physical Review Letters **79**, 2697–2699 (1997)

107. S. Kim, J. Jin, Y.J. Kim, I.Y. Park, Y.Kim and S.W. Kim, "High-harmonic Generation by Resonant Plasmon Field Enhancement," Nature **453**, 757–660 (2008).

108. P. Muhlschlegel, H. -J. Eisler, O. J. F. Martin, B. Hecht and D. W. Pohl, "Resonant Optical Antennas," Sceience **308**, 1607–1609 (2005).

109. Tiberiu-Dan Onuta, Matthias Waegele, Christopher C. DuFort, William L. Schaich, and Bogdan Dragnea, "Optical Field Enhancement at Cusps between Adjacent Nanoapertures," Nano Letters **7**, 557–564 (2007).

110. Eric X. Jin and Xianfan Xu, "Enhanced Optical Near Field from a Bowtie Aperture," Applied Physics Letters **88**, 153110 (2006).

111. L. Wang and X. Xu, "Spectral resonance of nanoscale bowtie apertures in visible wavelength," Applied Physics A **89**, 293–297 (2007)

112. A. Guerrero and Bernardo S. Mendoza, "Model for great enhancement of second harmonic generation in quantum dots," J. Opt. Soc. Am. B, **12**, 559–569 (1995)

113. "Qdot Streptavidin Conjugates User Manual," Quantum Dot Corporation, PN 90-0003, Rev 9.2

114. P. Muhlschlegel, H. J. Eisler, O. J. F. Martin, B. Hecht , D. W. Pohl, "Surface plasmon amplification by stimulated emission of radiation: Quantum generation of coherent surface plasmons in nanosystems," Physical Review Letters,**90**, 027402 (2003)

115. http://en.wikipedia.org/wiki/Metamaterial

116. J. B. Pendry, A. J. Holden, D. J. Robbins, and W. J. Stewart, "Magnetism from Conductors and Enhanced Nonlinear Phenomena," IEEE Transactions on Microwave Theory and Techniques, **47**, 2075 (1999)

117. C. Enkrich, M.Wegener, S. Linden, S. Burger, L. Zschiedrich, F. Schmidt, J. F. Zhou, Th. Koschny, and C. M. Soukouli, "Magnetic metamaterials at telecommunication and visible frequencies," Physical Review Letters, **95**, 203901 (2005)

118. M. W. Klein, C. Enkrich, M. Wegener, C.M.Soukoulis, and S. Linden, "Single-slit split ring resonators at optical frequencies: limits of size scaling," Optical Society of America, (2005)

119. Stefan Lindon, Christian Enkrich, Martin Wegener, Jiangfeng Zhou, Thomas Koschny and Costas M. Soukoulis, "Magnetic response of metamaterials at 100 terahertz," Science, **306**, 1351-1353 (2004)

120. J. Zhou, Th. Koschny, M. kafesaki, E. N. Economou, J. B. Pendry and C. M. Soukoulis, "Saturation of the magnetic response of split ring resonators at optical frequencies," Physics Review Letters, **95**, 223902 (2005)

121. Zhiming Huang, Jianqiang Xue, Yun Hou, Junhao Chu and D. H. Zhang, "Surface plasmon induced optical magnetic response in perforated trilayer metamaterial," Physics Review E, **76**, 016606 (2007)

122. Matthias W. Klein, Christian Enkrich, Martin Wegener and Stefan Linden, "Second Harmonic Generation from Magnetic Metamaterials," Science, **313**, 502–504 (2006)